UNIVERSITY OF CALIFORNIA,
IRVINE

**The Role of Microglia in the Immune Response to Breast Cancer Brain Metastasis**

DISSERTATION

submitted in partial satisfaction of the requirements
for the degree of

DOCTOR OF PHILOSOPHY

in Physiology and Biophysics

by

Katrina Taylor Evans

Dissertation Committee:
Associate Professor Devon A. Lawson, Chair
Distinguished Professor Michael D. Cahalan
Assistant Professor Armando Villalta
Associate Professor Mathew Blurton-Jones

2021

# DEDICATION

To

My committee chair, committee members, colleagues, family and friends who supported and encouraged me to complete this work.

"but it be the strangeness you see that pulls you to the next horizon."
**— Robert Jordan, The Eye of the World**

*"Do what you can, with what you have, where you are"*

Theodore Roosevelt

*"'Far and away the best prize that life has to offer is a chance to work hard at work worth doing.' And I would add that what makes work worth doing is getting to do it with people that you love… Now go find your team and get to work"*

Leslie Knope, "One Last Ride," Parks and Recreation, Season 7, Episode 13

# TABLE OF CONTENTS

# LIST OF FIGURES

# LIST OF TABLES

Page

# ACKNOWLEDGEMENTS

I would like to express the deepest appreciation to my committee chair, Devon A. Lawson. Thank you for encouraging me to pursue this work, facilitating these experiments with your guidance and expertise on breast cancer metastasis and breast cancer models, holding high standards or scientific rigor, all while being patient and supportive of the process of learning.

I would like to thank my committee members, Professor Mike Cahalan, Matthew Blurton- Jones, and Armando Villalta. Thank you for your advice in experimental design and providing critical mouse models, reagents and collaborations with your students and Post Docs.

This work would not have been possible without my collaborator Kerrigan Blake, who performed the computational analysis of the single cell RNAseq data sets in our co-first author manuscript and has given me permission to publish this as chapter 2 of my thesis.

Additionally, I want to express my deepest gratitude to Aaron Longworth, Dennis Ma, Morgan Coburn, Quy Nguyen, Grace Hernandez, Hamad Alshetaiwi, Davit Orujyan and Armani Oganyan who helped me perform these experiments. Maren Pein and Jacob Insua-Rodriguez who provided important critique and feedback on the manuscript and experimental design and interpretation, and Nicholas Pervolarakis, Justice Williams, Kevin Knee, and Ryan T. Davis and Paige Halas for their friendship and comradery in the lab. I also could not have completed this work without the support of our lab managers, Nathan James, Grace Hernandez, and Sharmila Mallya, thank you for procuring all my reagents on time. I would also like to thank my funding sources: the National Institutes of Health T32AI 0602573, the Stanley Behrens Fellows in Medicine award and the UCI Graduate Dean's Dissertation Fellowship.

Finally, I thank my family. My husband, my dad, and my mom, who especially made a difference in 2020/2021, during COVID-19 pandemic and the birth of my son. Words cannot express how much I appreciate your support at home in helping me learn to be a mom and scientist and giving the peace of mind to go to work and leave my baby cared for in a loving and fun home with you.

## VITA

Katrina Taylor Evans

| | |
|---|---|
| 2010 | B.S. in Biological Sciences, California State University, Fullerton |
| 2011 | High School Science Teaching Credential, University of California, Irvine |
| 2012-2015 | High School Science Teacher, Orange County School of the Arts, Santa Ana, CA |
| 2015-2021 | Ph.D. in Physiology and Biophysics, University of California, Irvine |

### FIELD OF STUDY

Immunology of Breast Cancer Brain Metastasis

### PUBLICATIONS

1. Katrina T. Evans*, Kerrigan Blake*, Aaron Longworth, Morgan A. Coburn, Quy H. Nguyen, Dennis Ma, Grace A. Hernandez, Armani K. Oganyan, Davit Orujyan, Robert A. Edwards, Clare Pridans, Mathew Blurton-Jones, and Devon A. Lawson. Microglia mount a pro-inflammatory response to suppress breast cancer brain metastasis. *Co-first authors, in revision, Nature Cell Biology

2. Dennis Ma*, Grace A. Hernandez*, Austin E. Y. T Lefebvre, Hamad Alshetaiwi, Kerrigan Blake, Kushal R. Dave, Maha Rauf, Justice W. Williams, Ryan T. Davis, Katrina T. Evans, Aaron Longworth, Madona Y.G. Masoud, Regis Lee, Robert A. Edwards, Michelle A. Digman, Kai Kessenbrock†, Devon A.Lawson†. Patient-derived xenograft culture-transplant system for investigation of human breast cancer metastasis. Communications Biology. Accepted, in Press, Manuscript # COMMSBIO-20-2413-T *Authors Contributed Equally. Preprint available on bioRxiv. https://doi.org/10.1101/2020.06.25.172056

3. Hamad Alshetaiwi, Nicholas Pervolarakis, Laura Lynn McIntyre, Dennis Ma, Quy Nguyen, Jan Akara Rath, Kevin Nee, Grace Hernandez, Katrina Evans, Leona Torosian, Anushka Silva, Craig Walsh and Kai Kessenbrock. Defining the emergence of myeloid-derived suppressor cells in breast cancer using single-cell transcriptomics. Sci Immunol., 2020. Feb 21;5(44):eaay6017. PMID: **32086381**

4. Ian Parker, Katrina T. Evans, Kyle Ellefson, Devon A. Lawson, and Ian F. Smith. Lattice light sheet imaging of membrane nanotubules between human breast cancer cells in culture and in brain metastases. Sci Rep., 2017. Sep 8;7(1):11029. PMID: 28887508

5. Math P. Cuajungco, William Podevin, Vinod K. Valluri, Quang Bui, Van H. Nguyen, Katrina Taylor. Abnormal accumulation of human transmembrane (TMEM)-176A and 176B proteins is associated with cancer pathology. Acta Histochem., 2012. PMID: 22244448

## POSITIONS

| | |
|---|---|
| 2016 – June 2021 | Graduate Student Researcher, UC Irvine, Dr. Devon Lawson's Lab |
| 2012 - 2015 | High School Science Teacher, Orange County School of the Arts |
| 2011-2012 | Student teacher Northwood High School, Irvine CA |
| | Long-Term Substitute Teacher, Whittier Christian High School |
| Summer 2012 | UCI COSMOS Teacher Fellow, Biomedical Cluster |
| 2008 - 2010 | Undergraduate researcher, California State University Fullerton |

## FELLOWSHIPS AND HONORS

| | |
|---|---|
| 2020 | Graduate Dean's Dissertation Fellowship |
| 2017-2018 | Stanley Behrens Fellow in Medicine |
| December 2017 | UCI Annual Immunology Fair 2nd place award for talk competition |
| Aug 2017- Sep 2018 | National Institutes of Health Training Grant T32 AI 0602573 |
| 2015 | NSF Graduate Research Fellowship- honorable mention |
| June 2010 | Graduated Magna Cum Laude, CSU Fullerton |
| 2008 - 2010 | HHMI Undergraduate Research Fellowship |
| 2008-2010 | Dean's List for 5 semesters, CSUF, College of Natural Science and Mathematics |

## POSTERS AND PRESENTATIONS

| | |
|---|---|
| December 2019 | "Single-cell analysis reveals microglia coordinate immune response to breast cancer brain metastasis" UCI Annual Immunology Fair, Irvine, CA |
| January 2019 | "Single-cell analysis of the brain microenvironment in breast cancer metastasis" Mid-Winter Conference of Immunologists, Asilomar, CA |

| | |
|---|---|
| June 2018 | "Single-cell analysis of the brain microenvironment in breast cancer metastasis" New Frontiers in Neuroinflammation, Keystone Symposia, CO |
| December 2017 | "Investigating the Brain Metastatic Niche in Breast Cancer," UCI Annual Immunology Fair, Irvine, CA. |
| December 2016 | "Mouse Model of Breast Cancer Brain Metastasis," Chao Family Comprehensive Cancer Annual Scientific Meeting |
| November 2016 | "Mouse Model of Breast Cancer Brain Metastasis," Chao Family Comprehensive Cancer Annual Scientific Meeting |

# ABSTRACT OF THE DISSERTATION

**The Role of Microglia in the Immune Response to Breast Cancer Brain Metastasis**

by

Katrina Taylor Evans

Doctor of Philosophy in Biomedical Sciences

University of California, Irvine, 2021

Assistant Professor Devon A. Lawson, Chair

Breast cancer brain metastasis (BCBM) is a lethal disease with no effective treatment options and limited experimental models. BCBMs are densely infiltrated by activated macrophages, but their origin, function and potential for therapeutic targeting are controversial. We used single-cell RNA-sequencing to investigate the role of brain-resident microglia in mouse and humanized models of BCBM. We find that mouse and human microglia directly interface with metastatic cells and mount a robust pro-inflammatory response. This is associated with upregulation of type I and II interferon responses, antigen presentation machinery cytokine and exome secretion and expansion of T and natural killer (NK) lymphocytes that control tumor outgrowth. Functional studies show that microglia depleted animals display decreased survival, increased metastasis, and impaired T and NK cell response to BCBM. This demonstrates the important tumor suppressive function of microglia during BCBM initiation.

# CHAPTER 1: INTRODUCTION

## BCBM Prognosis and Therapy

Breast cancer metastasis is the process of cancer cell escape from the primary tumor in the breast, dissemination throughout the body via the lymphatics and circulatory system, and finally seeding and outgrowth in a distal site. In recent years, the frequency of breast cancer brain metastasis (BCBM) has increased (Lombardi et al. 2014; Tosoni, Ermani, and Brandes 2004). This is paradoxically attributed to improvements in the treatment of peripheral tumors and metastasis; as patients survive longer, they have increasing opportunity to develop brain metastasis (Lombardi *et al.*, 2014). Currently, the recommended treatments for BCBM include radiotherapy, surgical resection, systemic chemotherapy or anti-Her2 therapy if indicated by the tumor subtype (Lin, 2014). Unfortunately, even with treatment, the prognosis for brain metastasis is poor, and ultimately leads to mortality in <2 years in nearly all patients (Niikura, et al., 2014). Given this poor prognosis, there is an urgent need to identify new therapeutic targets to treat BCBM. Immunotherapies including immune checkpoint blockade inhibitors and CAR-T cell therapies have shown success in treating cancer in the periphery and may have potential for treating cancers in the brain (Wei et al. 2018), however, more research is needed to understand how the immune response develops in metastatic brain tumors and why it ultimately fails and results in tumor outgrowth.

## Potential role or the immune system in BCBM

The innate and adaptive arms of the immune system play a role in all phases cancer progression from tumor initiation and growth to metastatic dissemination, seeding and outgrowth at a distal site (Gonzalez, Hagerling, and Werb 2018). Immune cells such as macrophages, NK cells, CD8+, CD4+ TH1 cells can be tumoricidal during cancer initiation, but over time, become suppressed by chronic inflammatory conditions and regulatory T cells in the tumor microenvironment and favor tumor growth and metastasis (Wei et al. 2018; Mantovani et al. 2017). This process has been studied

in more detail in the periphery, but is less well characterized in the brain, especially in the context of metastasis. This in part because the central nervous system (CNS) and brain were previously thought to be 'immune privileged' and relatively devoid of immune cells. It is now understood that the CNS and brain are 'immune specialized,' with unique cellular and anatomical features that protect the brain (Russo and McGavern 2015). These include the blood brain barrier, lymphatics, meninges, the bony scull that encases the brain and specialized resident macrophage populations that occupy the brain and meninges (Herz et al. 2017; Jordão, Sankowski, Brendecke, Sagar, et al. 2019; Prinz, Erny, and Hagemeyer 2017). These macrophages, collectively called central nervous system (CNS) associated macrophages, or CAMs have embryonic origins and specialized physiology (Ginhoux and Prinz 2015). Due to their location in the CNS, CAMs may represent an important target for developing BCBM specific immune therapies.

CAMs play important functions during CNS homeostasis and disease, based on their location and physiology. For example, the brain parenchyma is tiled by microglia, while other boarder associated macrophages (BAMs) patrol the perivascular space, choroid plexus and meninges, (Goldmann et al. 2016; Herz et al. 2017). Microglia are the most numerous of these cell types, maintaining region-specific density by self-renewal and carry out vital functions such as phagocytosing apoptotic neurons and pruning synapses during development and homeostasis (Elmore et al. 2014; Li and Barres 2018). Homeostatic microglia appear ramified, with small cell bodies and thin branched protrusions that actively survey the brain for signs of damage (Boche, Perry, and Nicoll 2013). Like macrophages in the periphery, microglia possess pattern recognition receptors including Toll-like receptors and Siglecs to detect pathogens (Hickman et al. 2015). Additionally, microglia express Cx3CR1, the Fractaline (CX3CL1) receptor, and P2ry12 and other nucleotide receptors to attract microglia to sites of neuroinflammation and cellular damage respectively (Hughes et al. 2002; Lou et al. 2016). Thus, microglia are capable of rapidly detecting and responding to infection, inflammation and tissue damage. Under these conditions, microglia shift

from ramified to amoeboid morphology (Davalos et al. 2005; Haynes et al. 2006). Amoeboid microglia move towards injured tissue where it is thought that they may have different activation states depending on the environmental cues of the injury or disease (Wolf, Boddeke, and Kettenmann 2017a). This skewing is analogous to M1 and M2 polarization of macrophages in the periphery and depends on the type of damage, and secondary signals from infiltrating immune cells that enter the CNS during inflammation (Kettenmann et al. 2011). In other contexts such as ischemic stroke, experimental autoimmune encephalopathy, Parkinson's Alzheimer's and disease, activated microglia downregulate homeostatic genes such as Tmem119 and P2RY12 , and upregulate proteins such as IBA1 for membrane ruffling and motility, MHC-I and MHC-II for antigen presentation, and processes such as phagocytosis, and iNOs production (Bennett et al. 2016; Ito et al. 1998; Mildner et al. 2017). Given their ability to detect and respond to brain injury, microglia may also be able to detect and respond to primary and metastatic tumors in the brain.

**Evidence for Immune Response to BCBM in Patients**

Some clues to the potential role of microglia in BCBM can be found in pathology studies of primary and metastatic brain tumors after surgical resection. Immunohistochemistry analysis of surgically resected primary and metastatic brain tumors indicate immune cells may mount an anti-tumor response. First, primary brain tumors and brain metastasis are marked by macrophage/microglia infiltration and activation, including upregulation of markers for phagocytosis, reactive oxygen species and MHC-DR (MHC-II) (Berghoff, et al., 2013). Second, increased peritumoral brain edema correlates positively with higher density of tumor infiltrating lymphocytes and overall survival (Berghoff, et al., 2016; Spanberger, et al., 2013). Third, survival after tumor excision correlates positively with tumor infiltrating lymphocytes and CD68+ macrophage infiltration within the tumor (Duchnowska, et al., 2016). Finally, expression of the MHC-II invariant chain CD74, which participates in MHC-II and MHC-I peptide loading for antigen presentation, was found to be expressed by macrophages in glioma, and correlated positively with prolonged patient

survival (Zeiner, et al., 2015; Zeiner, et al., 2018; Basha, et al., 2012). These data suggest that tumor infiltrating macrophages/microglia and lymphocytes may be able to coordinate an immune response in the brain to slow tumor outgrowth. However, it remains unclear whether these macrophages are of CNS or peripheral origin, and why anti-tumor immunity ultimately fails in the CNS. Experimental approaches including *in vitro* and *vivo* models are needed to investigate these questions including the role of microglia in the anti-tumor immune response to BCBM.

## Experimental Models used to Study Breast Cancer Brain Metastasis

Investigating the biology of BCBM poses many challenges. Freshly resected or postmortem human BCBM samples are rare and difficult to obtain. More typically human BCBM samples come in the form of formalin fixed paraffin embedded or frozen blocks. These types of samples can be used to study histology, RNA, and protein expression, but preclude investigating system and cellular responses in a controlled experimental setting. BCBM is also a difficult disease to model *in vitro*. The microenvironment of BCBM includes endothelial cells, pericytes, and astrocytes that form the blood brain barrier, and microglia, neurons and oligodendrocytes in the parenchyma (Quail and Joyce 2017a; Steeg 2016). Infiltrating immune cells such as monocytes, neutrophils, dendritic cells, T cells and B cells also increase the complexity of the BCBM tumor microenvironment at advanced stages. Some research groups use *in vitro* approaches to investigate this system, including astrocyte-cancer cell co-cultures, and brain slice cultures, however this has not been widely adopted due to the challenges of the culture technique and caution generalizing findings to the intact brain (Q. Chen et al. 2016; Pukrop et al. 2010; Valiente et al. 2014) (Klemm et al. 2021 Biorxiv). Lastly, Microglia function is difficult to model *in vitro* due to the lack of brain-specific signals; they lose many important aspects of their cellular identity (Gosselin, et al., 2017). Thus, investigations using *in vitro* microglia must be carefully designed and interpreted with caution.

While human patient samples and *in vitro* models have their place in investigating BCBM, due to limitations and challenges, researchers have relied on mouse models to study BCBM. Mouse models have the advantage that they can more authentically model the process of BCBM, and have the cellular components of the brain and peripheral immune system. There are two mouse models predominantly used to investigate BCBM. These models rely on cell lines that are capable of metastasizing to the brain after injection into arterial circulation through the left ventricle. The human triple negative breast cancer cell line, MDA-MD-231, is studied in immunocompromised mice, including FOXn1$^{NU/NU}$ and NOD/SCID strains which lack T cells, B cells and an adaptive immune response(Fitzgerald et al. 2008). This permissive background allows for MDA-MB-231 cells to cross the blood brain barrier early after injection, and form micrometastasis as early as 7 days, and macrometastasis by 28 days in FOXn1$^{NU/NU}$ mice (Kienast et al. 2010; Lorger et al. 2019). In the immune competent setting, the basal-like mouse mammary carcinoma cell line, 4T1, is injected into syngeneic BALB/c mice. 4T1 metastasis progresses rapidly into lethal macrometastasis by ~14 days after intracardiac injection. Several groups have established brain tropic sub-lines cell lines (MDA-MB-231-BrM2, 4T1-Br, and LN-99-BrM2) by serially isolating brain metastasis from cardiac injected mice, making them convenient tools to study BCBM (Bos et al. 2009; Sevenich et al. 2014) (Klemm, 2021 Biorxiv). More recently, the EO771 triple negative cell line has been used in both cardiac injection and direct injection models of BCBM in C57BL/6 mice (Guldner et al. 2020a). Importantly, these mouse models contain the complex components of the brain microenvironment and the intact immune system. This will allow more research into the mechanisms of BCBM and the role of the immune response in blocking or facilitating metastatic outgrowth in the brain.

**Table 1. Summary of selected literature on metastasis, breast cancer brain metastasis, and primary brain tumors.**

| Ref. (author, year, title) | Cell line and model | Key findings |
|---|---|---|
| Fitzgerald, et al., 2008. Reactive glia are recruited by highly proliferative brain metastasis of breast | MDA-MB-231 cardiac injection experimental metastasis model. Cancer cell glia co-culture | Analysis of GFAP+ astrocytes, CD45+, CD11b+ cells, KI67 and Cleaved Caspace 3 (CC3) in human metastasis samples and experimental MDA-231 metastasis.<br>Demonstration that experimental metastasis can model immune and glia interactions |

| | | |
|---|---|---|
| cancer and promote tumor cell colonization | | |
| Bos et al., 2009. Genes that mediate breast cancer brain metastasis | Generation of brain tropic MDA-MB-231 BR2 cell line | RNA-seq analysis of parental and brain tropic BR2 sub line of MDA-231 and CN34 breast cancer cell lines reveal St6Galnac5 as a gene that mediates brain metastasis. |
| Lorger & Felding-Habermann, 2010. Capturing changes in the brain microenvironemtn during initial steps of breast cancer brain metastasis | 4T1, MDA-MB-231/brain, MDA-MB-435, MCF-7, ad MDA-MB-231(parental) BC17/SCID mice | IVIS imaging shows progression of different cell line metastasis models. IF analysis of tissues for F4/80, CD31, nestin and GFAP, and MMP9. Cancer cell invasion into the brain is marked by glial activation. |
| Kienast et al. 2010 Real-time imaging reveals the single steps of brain metastasis formation | Chronic cranial window and live imaging of PC14-PE6 and HTB177 Lung carcinoma, and MDA-MB-435 and A2058 melanoma | The essential steps of brain metastasis visualized including arrest at vascular branch points, early extravasation, persistent close contact to microvessels and perivascular growth and early angiogenesis. |
| Pukrop, et al., 2010. Microglia promote colonization of brain tissue by breast cancer cells in a Wnt- dependent way | Brain slice cultures MCF-7 human breast cancer cell line M410.0 murine mammary carcinoma | Microglia promote tumor invasion via wnt signaling to cancer cells. Microglia promote tumor invasion |
| Coniglio, et al., 2012. Microglial Stimulation of Glioblastoma Invasion Involves Epidermal Growth Factor Receptor (EGFR) and Colony Stimulating Factor 1 Receptor (CSF-1R) Signaling | Glioblastoma GL261 C57BL/6 CSF1R inhibitor (PLX3397) EGFR inhibitor | CSF1R inhibition in vivo and in vitro reduced microglia invasion into tumors. Reduction in glioblastoma invasions. EGFR inhibitor blocked glioblastoma invasion. Pro-tumor function of TAMs |
| Pyonteck, et al., 2013. CSF-1R inhibition alters macrophage polarization and blocks glioma progression | Glioblastoma multiforme proneural muse model (PDG). CSF1R inhibitor (BLZ945) | Depletion of TAMs via (CSF1R) inhibition results in reduced tumor burden and increased survival surviving TAMs show decreased expression of M2 macrophage-associated, pro-tumorigenic markers. Pro-tumor role of TAMs |
| Sevenich, et al., 2014. Analysis of tumor- and stroma- supplied proteolytic networks reveals a brain metastasis-promoting rolw for cathepsin S | MDA-231 cells, in NOD/SCID mice and MMTV-PyMT cells in FVB/N mice Cathepsin S inhibitor VBY-999 prevention trial | Cathepsin, a tight junction proteolytic enzyme, expressed by tumor cells or microglia increased brain metastasis *in vivo.* Microglia are tumor promoting |
| Valiente et al., 2014. Serpins promote cancer cell survival and vascular co-option in brain metastasis | MDA-MB-231 BrM2 in FOXn1 nude mice | Plasminogen activator inhibitory serpins in cancer cells shield metastatic cells as they colonize the brain. |
| Steeg 2016. Targeting Metastasis | NA, review | Therapies designed to treat primary tumors translate poorly to treating metastasis, the driving cause of cancer related deaths. Pre-clinical models of metastasis are needed to investigate potential targets in each specific metastatic tissue, including the brain. |
| Bowman et al., 2016. Macrophage Ontogeny Underlies Differences in Tumor-Specific Education in Brain Malignancies | Glioma mouse model, lineage tracing, RNA-seq and ATAC-seq | Identification of microglia and bone marrow derived macrophage gene expression and chromatin profiles. Identification of CD49D and CD11a to distinguish Microglia from infiltration macrophages in brain malignancy. |
| Quail et al., 2016. The tumor microenvironment underlies acquired resistance to CSF-1R inhibition in gliomas | PDG mouse model of glioma BLZ945 CSF-1R inhibitor | Depletion of TAMs via BLZ945 results in reduced tumor burden and increased survival. Tumors developed resistance to CSF1R inhibition. Macrophage derived IGF-1 and tumor derived IGF-1receptor derive this resistance through PI3K pathway active in recurrent GBM. Inhibition of IGF-1R and PI3K with CSF-1R inhibition prolongs overall survival. Pro-tumor role of TAMs |
| Chen et al. 2016. Carcinoma- astrocyte gap junctions promote brain | Brain tropic MDA-231 (breast) and H2030 (NSCLC) cells | Demonstration of Cancer-cell- astrocyte interactions. Brain tropic cell lines MDA-231 and H2030 overexpress PCCDH7, which promotes gap |

| | | |
|---|---|---|
| metastasis by cGAMP transfer | | junction assembly. cGAMP transfer through astrocyte- cancer gap junctions promote metastatic outgrowth. |
| Quail & Joyce, 2017. The microenvironmental landscape of brain tumors | NA, review | The brain tumor microenvironment is a regulator of primary and metastatic tumors. Discussion of components of the brain tumor microenvironment and how they can be leveraged for and potential therapies. |
| Yan D. et al., 2017. Inhibition of colony stimulating factor-1 receptor abrogates microenvironment-mediated therapeutic resistance in gliomas | PDGF-B driven proneuronal mouse model of glioma PLX3397 CSF-1R inhibitor | PLX339s blocks glioma progression and suppresses tumor proliferation and tumor grade. PLX339 inhibition of TAMS restores glioma sensitivity to tyrosine kinase inhibitors. Pro-tumor role of TAMs |
| Priego et al., 2018. STAT3 labels a subpopulation of reactive astrocytes required for brain metastasis | Variety of brain metastatic cell lines, B16/F10 BrM | Stat3+ reactive astrocytes associate with brain metastasis and supports metastasis by modulating innate and adaptive immune response. Blocking stat3 in patients with brain metastasis had significant anti-tumor affects |
| Taggart et al. 2018. Anti-PD-1 and anti-CTLA4 efficacy in melanoma brain metastasis depends on extracranial disease and augmentation of Cd8 T cell trafficking. | B16 melanoma C57BL/6 | Anti- PD-1 and CTLA-4 therapy enhances peripheral expansion and homing of CD8 T cells to the brain. Anti-tumor role for CD8 and NK cells in CNS metastasis. |
| Lorger et al 2019. Immune checkpoint blockade- How does it work in Brain metastasis? | NA, review | Anti-PD1 and anti-CTLA4 therapy is showing some success in clinical trials for brain metastasis. |
| Yan J et al. 2019. FGL2 promotes tumor progression in the CNS by suppressing CD103+ dendritic cell differentiation | Glioblastoma | FGL2 knockout in tumor cells impairs GBM progression in immune competent mice.<br>NF-Kb, Stat1/5 and p38 activation in CD103+ DCs.<br>Anti-tumor role of CD103+ DCs |
| Qiao et al., 2019. Long term characterization of activated microglia/ macrophages facilitating the development of experimental brain metastasis through intravital microscope imaging | Melanoma mouse model CX3CR1-GFP transgenic mouse<br>MMP3 inhibitor | PLX3397 CSF1R inhibitor reduced melanoma BM occurrence.<br>MMP3 expressed by microglia/macrophages, MMP3 inhibitor moderately decreased melanoma BM.<br>Pro-tumor role of TAMs |
| Klemm et al., 2020. Interrogation of the Microenvironmental landscape in brain tumors reveals disease specific alterations of immune cells | Survey of brain tumor microenvironment by flow cytometry, RNA-seq, protein arrays, culture assays and special tissue characterization. | Reveals disease specific changes in the immune cells in the CNS during glioma and brain metastasis.<br>Brain metastasis shows upregulation of IL6 in microglia. |
| Guldner et al., 2020. CNS-native myeloid cells drive immune suppression in the brain metastatic niche through Cxcl10 | ScRNA-seq of CNS myeloid cells from EO771 model of BCBM<br>Cx3CR1 DTR depletion of CNS myeloid cells<br>Cxcl10 inhibition<br>PD1, VISTA therapy | Cx3CR1-ko mice have increased metastasis and increased expression of IFNA pathway.<br>CNS-myeloid are immune suppressive. |
| Ochocka, et al., 2021. Single-cell RNA sequencing reveals functional heterogeneity of glioma associated brain macrophages | scRNA-seq of Cd11b+ myeloid cells in naïve and GL261 glioma bearing mice. | Microglia upregulate APC, and IFN pathways. Male mice have higher expression of MHCII.<br>Sex differences in microglia response. |
| Klemm et al. June 7. 2021, Biorxiv | MDA-BrM and 99LN-BrM2 breast -BrM mouse | DEG analysis show higher expression of antigen presentation, tissue remodeling and immune regulation in TAM-MDM. TAM-MG show higher |

| | | |
|---|---|---|
| Compensatory CSF2-driven macrophage activation promotes adaptive resistance to CSF1R inhibition in breast to brain metastasis | models. CSF1R inhibitor BLZ945<br>Ex vivo brain slice culture microscopy.<br>Bulk RNA seq of FACS sorted lineage restricted TAM-MG and TAM-MDM. | expression of wound responses and regulation of neurological function.<br>Signatures for leukocyte recruitment were similar between TAM-MG and TAM-MDM. Microglia support tumor extravasation and colonization of the brain.<br>TAM-MG depletion leads to initial response at 4-7 days, then no difference in tumor size.<br>Remaining 35% of TAMs shift from CSF1R to CSF2RB-Stat5 signaling, drives wound processes such as IL4. |

## Central Question, Hypothesis, and Summary

The goal of my work is to investigate the immune response to BCBM, with an emphasis on the response of brain resident microglia. In preliminary studies using immunofluorescence staining of IBA1 to identify microglia and macrophages in MDA-MB-231 metastasis in Foxn1$^{nu/nu}$ mice, I found that microglia and macrophages home to metastasis. To investigate the microglia response to BCBM, we performed an un-biased single cell RNA sequencing screen of microglia, cancer cells, and astrocytes in two different mouse models and humanized mouse model of BCBM compared to control microglia. Single-cell RNA sequencing technology has allowed researchers to differentiate heterogeneous cell types and activation states under homeostatic and disease conditions in cancer and in the brain (Lawson, et al., 2018; Jordão, et al., 2019; Keren-Shaul, et al., 2017; Mathys, et al., 2017; Singer, et al., 2016; Steinman, et al., 2018). Applying this technology to the MDA-MB-231-Foxn1$^{nu/nu}$ model of we identified the responses of microglia to brain metastasis (BCBM-R) and verified this in freshly isolated microglia using flow cytometry, humanized microglia, and in situ using immunofluorescence microscopy. BCBM-R includes upregulation of a type I and II interferon, antigen presentation, proliferation and cytokine and exome secretion programs. Finally, I utilized a new mouse model with genetic knock out of the c-fms intronic regulatory element (FIRE-KO) which controls the expression of *Colony stimulating factor 1 receptor* to completely ablate microglia from the brain. The absence of microglia resulted in increased morbidity, metastatic outgrowth, and reduced numbers of T and NK cells during metastasis initiation. These data highlight the importance of the microglia response during BCBM and their role in supporting T and NK cells to suppress tumor outgrowth.

# CHAPTER 2: Microglia mount a pro-inflammatory response to suppress breast cancer brain metastasis

## Introduction

Breast cancer brain metastasis (BCBM) is increasing in incidence and rapidly emerging as a critical clinical problem in breast cancer. 15-30% of metastatic breast cancer patients develop brain metastasis, and autopsy and imaging studies indicate an additional 30% of patients are likely to develop brain metastasis as treatments for peripheral disease improve and patients live longer(Ostrom, Wright, and Barnholtz-Sloan 2018; Witzel et al. 2016). This is alarming since there are no effective treatments for brain metastasis and median survival is only a few months(Brufsky et al. 2011; Martin et al. 2018; Niikura et al. 2014; Rostami et al. 2016). There is growing interest in immunotherapeutic strategies to treat central nervous system (CNS) cancers, given that immune cells enter the brain during disease while most conventional therapies are precluded by the blood brain barrier (BBB)(Deeken and Löscher 2007; Tosoni, Ermani, and Brandes 2004). However, greater understanding of the immune response to BCBM will be needed to develop immunotherapy strategies effective in the unique immune microenvironment of the CNS.

The brain immune microenvironment is principally composed of specialized tissue resident macrophages called microglia that tile the brain and play diverse functions in CNS homeostasis and disease(Hammond, Robinton, and Stevens 2018; Hanisch and Kettenmann 2007; Wolf, Boddeke, and Kettenmann 2017b). Microglia represent an attractive immunotherapeutic target because they are the first line of defense to disease in the CNS and have the power to direct the initial immune response. BCBMs are heavily infiltrated with tumor associated macrophages (TAMs), which may be comprised of microglia, border-associated macrophages (BAMs), as well as bone marrow derived

myeloid cells (BMDMs) such as monocytes and macrophages(Duchnowska et al. 2016; Goldmann et al. 2016; Jordão, Sankowski, Brendecke, Locatelli, et al. 2019; Mrdjen et al. 2018; Quail and Joyce 2017b). Functional studies using genetic and pharmacologic approaches to deplete TAMs support a tumor promoting role for these cells. Depletion of TAMs with CSF1R inhibitors results in tumor reduction and decreased metastasis in glioblastoma and melanoma models(Coniglio et al. 2012; Pyonteck et al. 2013; Qiao et al. 2019; Quail et al. 2016; Yan et al. 2017). TAM depletion using a CX3CR1-targeted genetic ablation model similarly results in decreased BCBM(Guldner et al. 2020). However, it is unclear whether microglia or other types of TAMs produce the tumor promoting effects observed in these studies. CSF1R inhibitors have been shown to preferentially deplete microglia, but also attenuate other myeloid cells, and microglia ultimately repopulate the brain when treatment ceases. Likewise, CX3CR1 is expressed by diverse myeloid cell populations and upregulated by BMDMs upon entry into the brain(Bowman et al. 2016; Guldner et al. 2020). Therefore, the impact of brain resident microglia on tumor initiation and their potential as an immunotherapy target remain unclear.

We combined single cell RNA-sequencing (scRNA-seq) with newly developed genetic and humanized mouse models to show for the first time that microglia exert a potent tumor suppressive effect on BCBM initiation. ScRNA-seq of >75,000 cells from three different models revealed that microglia mount a robust pro-inflammatory response to BCBM. Subclustering of pro-inflammatory microglia showed further specialization of their response, where distinct populations of microglia upregulate programs for antigen presentation, interferon (IFN) response, phagocytosis, cytokine production, and glycolysis. ScRNA-seq showed that these discrete microglia substates were conserved in a humanized mouse model of BCBM, suggesting that human microglia have the capacity to respond similarly to disease initiation in BCBM patients. Finally, we investigated the function of

microglia in BCBM initiation using an innovative new genetic model that completely lacks microglia while retaining other CNS macrophages and myeloid cells(Rojo et al. 2019). We find that the absence of microglia results in decreased survival and increased BCBM progression, showing that microglia play an important role in tumor suppression. This contrasts with the pro-tumorigenic function reported for other types of TAMs in CNS cancer, and highlights the potential of harnessing the natural tumor suppressive function of microglia to treat brain metastasis.

## Results

### BCBM are extensively infiltrated with activated TAMs

During homeostasis, the brain is home to microglia that tile the parenchyma as well as BAMs that reside in the meninges, choroid plexus, and perivascular surface of blood vessels **(Fig 1A)**. During inflammation, there can be substantial infiltration of BMDMs that express similar markers, making it difficult to determine the origin and function of TAMs in BCBM **(Fig 1A)**. We first investigated TAM activation and localization in human patient BCBM by immunofluorescence (IF) staining for the canonical activation marker ionized calcium-binding adaptor molecule 1 (IBA1), which is expressed lowly by homeostatic microglia and highly by activated microglia and macrophages **(Fig 1A)**(Kettenmann et al. 2011). As expected, we find that IBA1$^+$ cells are evenly spaced throughout normal brain and display small cell bodies and ramified morphology typical of homeostatic microglia **(Fig 1B)**. In contrast, we find that BCBM are heavily infiltrated with IBA1$^+$ cells that display ameboid morphology typical of activated microglia and macrophages. We subsequently turned to a well-established mouse model of BCBM for further investigation of TAM origin and function(Bos et al. 2009; Lorger and Felding-Habermann 2010). In this model, MDA-MB-231-BR2 (231BR) human breast cancer cells are delivered into the arterial circulation of immune deficient animals via intracardiac injection, which facilitates metastasis to the brain. We injected 231BR cells

stably expressing firefly luciferase and AcGFP reporters into Foxn1$^{nu/nu}$ mice and analyzed the brain at progressive timepoints (**Fig 1C**). Consistent with prior reports, 231BR cells arrest in blood vessels and cross into the brain two to seven days after injection, then grow along blood vessels and form micrometastases by day 14 and parenchymal metastasis by day 28 (**Fig 1D**)(Kienast et al. 2010; Valiente et al. 2014). Interestingly, IF analysis shows that IBA1$^{+}$ cells surround and directly interface with cancer cells by day seven, showing they interact with cancer cells at the initial stages of micrometastasis initiation **(Fig 1D)**. We further find that day 28 parenchymal metastases are densely infiltrated with IBA1$^{+}$ cells, in contrast to regions of normal tissue distal to metastases **(Fig 1D)**. Quantification of IBA1 fluorescence intensity shows 4-fold higher signal in parenchymal metastases compared to control brains ($p<0.0001$) **(Fig 1E)**. These data show that TAMs immediately interact with metastatic cells and become progressively activated in mouse and human BCBM.

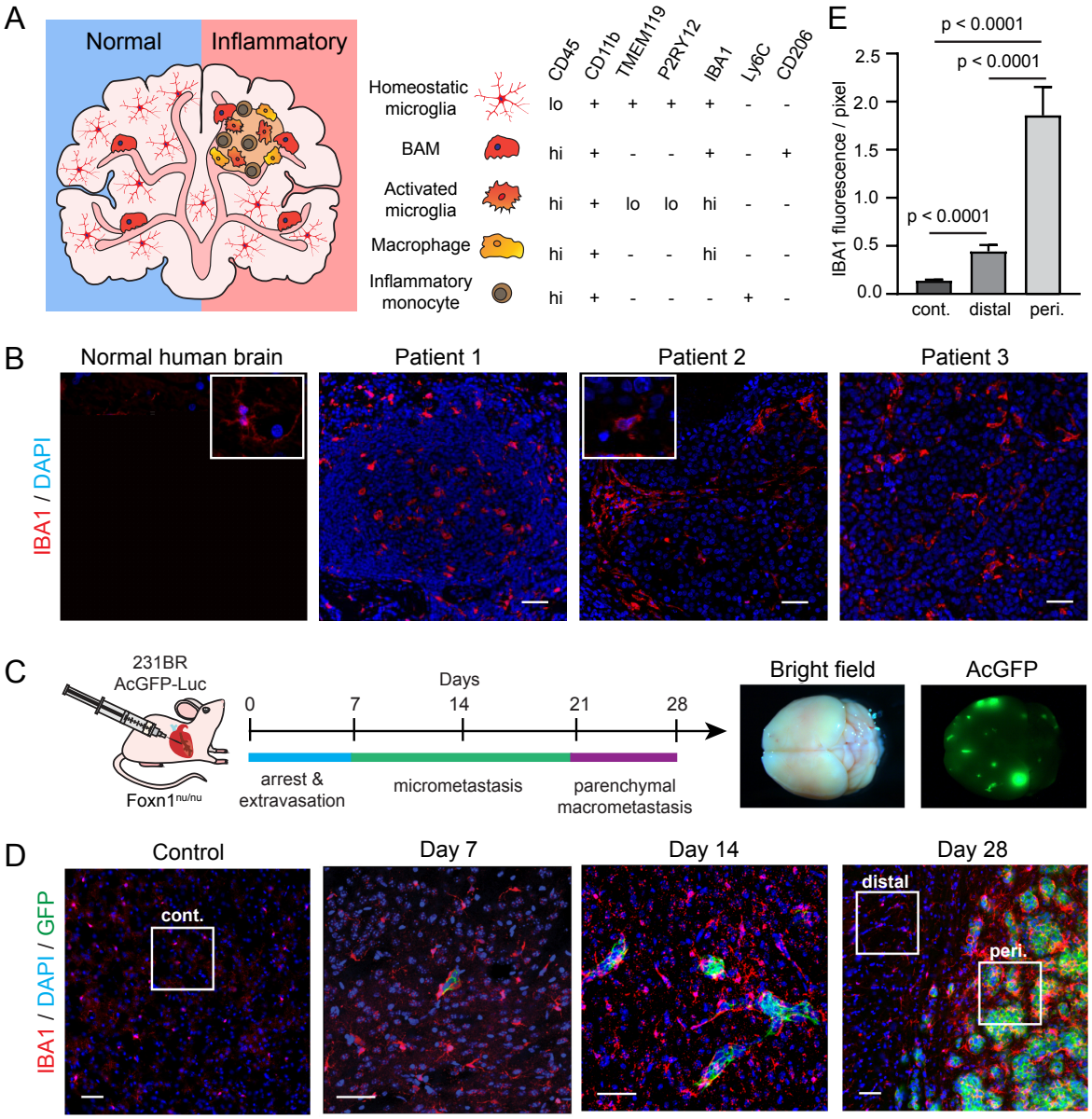


**Figure 1: BCBM are extensively infiltrated with activated TAMs.** (A) Schematic (left) of brain resident and bone marrow-derived macrophage cell types present in the normal and inflammatory brain microenvironment and their relative expression of canonical markers (right). BAM = border-associated macrophage. (B) IF staining shows IBA1⁺ cells (red) in normal human brain and three resected patient BCBM tumors. Insets show cell morphology. Scale bar = 50μm. (C) Schematic showing disease progression in mouse 231BR-Foxn1$^{nu/nu}$ BCBM experimental metastasis model. 500,000 AcGFP-Luc labeled 231BR cells were injected into the left cardiac ventricle of Foxn1$^{nu/nu}$ mice and harvested 28 days later. Whole mount brightfield and fluorescence microscopy images show a representative brain with AcGFP⁺ metastatic foci (green). (D) IF staining shows IBA1⁺ cells (red) in control and metastatic brains at 7, 14, and 28 days post 231BR cell injection. Metastatic cells are AcGFP⁺ (green). Boxes indicate representative peritumoral (peri.), distal and control (cont.) regions for IBA1 quantified in (E). Scale bar = 50μm. (E) Quantification of IBA1 expression in control (n=4) and metastatic (n=4) brains 28 days post 231BR cell injection. IBA1 fluorescence intensity per pixel was quantified in control (cont., n=115 fields), peritumoral (peri., n=127 fields) and distal (n=96 fields) regions as shown in (D). *P* values were generated using a two sided, unpaired Welch's *t*-test and error bars show standard deviation.

**Microglia display a robust pro-inflammatory response to BCBM initiation**

We used scRNA-seq to investigate the specific function of microglia in BCBM and discriminate them from other TAM populations in the 231BR-Foxn1$^{nu/nu}$ model. Cells were dissociated from control (n=3) and metastatic brains (n=3) by automated heated mechanical and enzymatic digestion followed by density centrifugation to remove myelin (**Fig 2A, Fig S1A**). Live 231BR metastatic (CD45$^-$ GFP$^+$) and myeloid cells (CD45$^+$CD11b$^+$) were subsequently isolated by flow cytometry (**Fig S1B**). Astrocytes (CD45$^-$ASCA2$^+$) were also sorted since they have been previously implicated in BCBM(Q. Chen et al. 2016; Priego et al. 2018; Valiente et al. 2014) (**Fig S1B**). Isolated cells were captured and prepared for sequencing using droplet-based technology (Chromium) (**Fig 2A**).

Mouse myeloid cells and astrocytes were discriminated from human 231BR cells by aligning to a merged human (GRCh38) and mouse (mm10) genome, where cells were identified as mouse if >87.5% of reads aligned to mm10 (**Fig S1C**). We removed poor quality cells and doublets by excluding cells with <500 genes, >2000 genes, or a mitochondrial gene percentage >10% (**Fig S1D**). The remaining cells were integrated across sequencing batch using the mutual k-nearest neighbors (kNN) algorithm adaptation in the Seurat pipeline(Butler et al. 2018; Stuart et al. 2019). Analysis of the 42,891 cells that passed further filtering revealed seven distinct cell types identified by lineage-specific markers and visualized by t-distributed stochastic neighbor embedding (tSNE) **(Fig 2B, Fig S1E-F)**. This included the targeted cell types, astrocytes (*Aldoc, Atp1a2*), microglia (*Tmem119, P2ry12*) and non-microglia myeloid cells including dendritic cells, monocytes and macrophages (*Lyz2, Plac8*) (**Fig 2B**, **Fig S1E-F**). We also recovered small numbers of ependymal cells (*Ccdc153, Rarres2*), oligodendrocytes (*Mbp, Ptgds*), vascular cells (*Cldn5, Vtn*), and lymphocytes (*Cd3g, Gzma*) (**Fig 2B**, **Fig S1E-F**). Peripheral immune cells, namely non-microglia myeloid populations and lymphocytes, were found preferentially in the metastatic condition (**Fig S1E-F**).

Further analysis of the 231BR cells showed limited heterogeneity beyond cell cycle differences. We found substantial heterogeneity amongst astrocytes, but it was principally associated

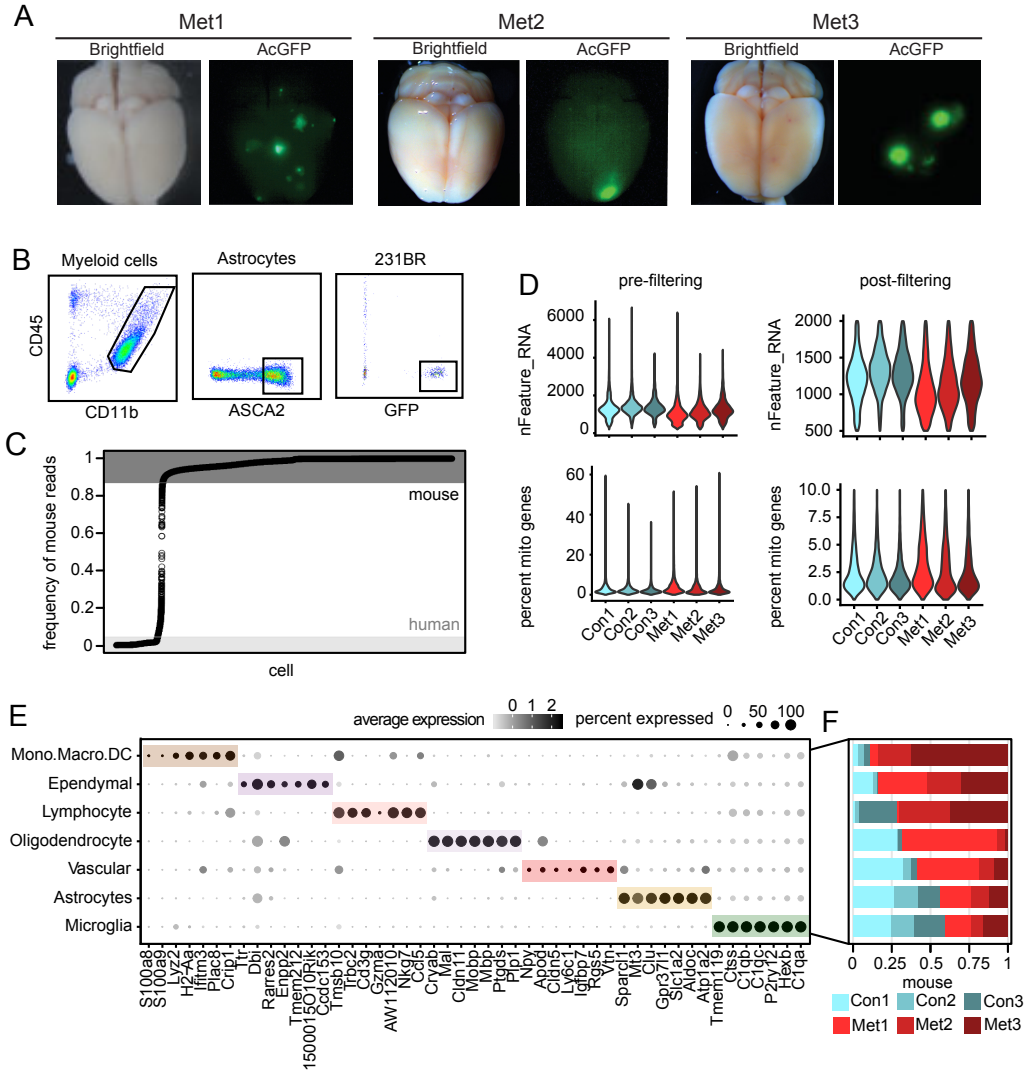


**Figure S1: Quality control and exclusion criteria for Foxn1$^{nu/nu}$ scRNA-seq cell libraries.** (A) Whole mount brightfield and fluorescent microscopy images of metastatic brains (Met1-3) used to generate the scRNA-seq dataset described in **Fig 2**. Metastatic lesions are AcGFP$^{+}$ (green). (B) Representative FACS plots show gating for single, live (Sytox negative) myeloid cells (CD45$^{+}$CD11b$^{+}$), astrocytes (CD45$^{-}$ASCA2$^{+}$) and 231BR cells (CD45$^{-}$GFP$^{+}$) isolated for scRNA-seq. (C) Identification of mouse and human cells by the frequency of reads that align to the mm10 mouse genome. Cutoffs used to identify mouse cells (>0.875 aligned, n=51,418 cells), human cells (<0.05 aligned, n=7336 cells) and doublets (0.05-0.875 aligned, n=913 cells) are shown. (D) Violin plots show cell distributions for key quality control metrics pre- and post-filtering and removal of poor quality cells. Cells were removed that displayed <500 or >2000 genes (nFeature_RNA), or >10% of genes mapped to the mitochondrial genome (percent mito genes). (E) Dot plot shows top marker genes for each cell type ranked by the average natural logFC and determined by the Wilcoxon rank sum test. Dot size represents the percentage of cells that express the gene, and dot greyscale represents the average expression level. (F) Bar chart showing the frequency of cells contributed by each mouse that localize to each cell type in (E).

with regional localization (**Fig S2A,B**). Consistent with prior work, astrocytes formed discrete subpopulations associated with the telencephalon (*Mfge8)*, diencephalon (*Agt)*, and cerebellum (*Gdf10)* (**Fig S2A-D**)(Zeisel et al. 2018). However, we did not identify strong transcriptomic shifts associated with BCBM using unbiased clustering or supervised differential expression analysis (**Fig S2E-F**).

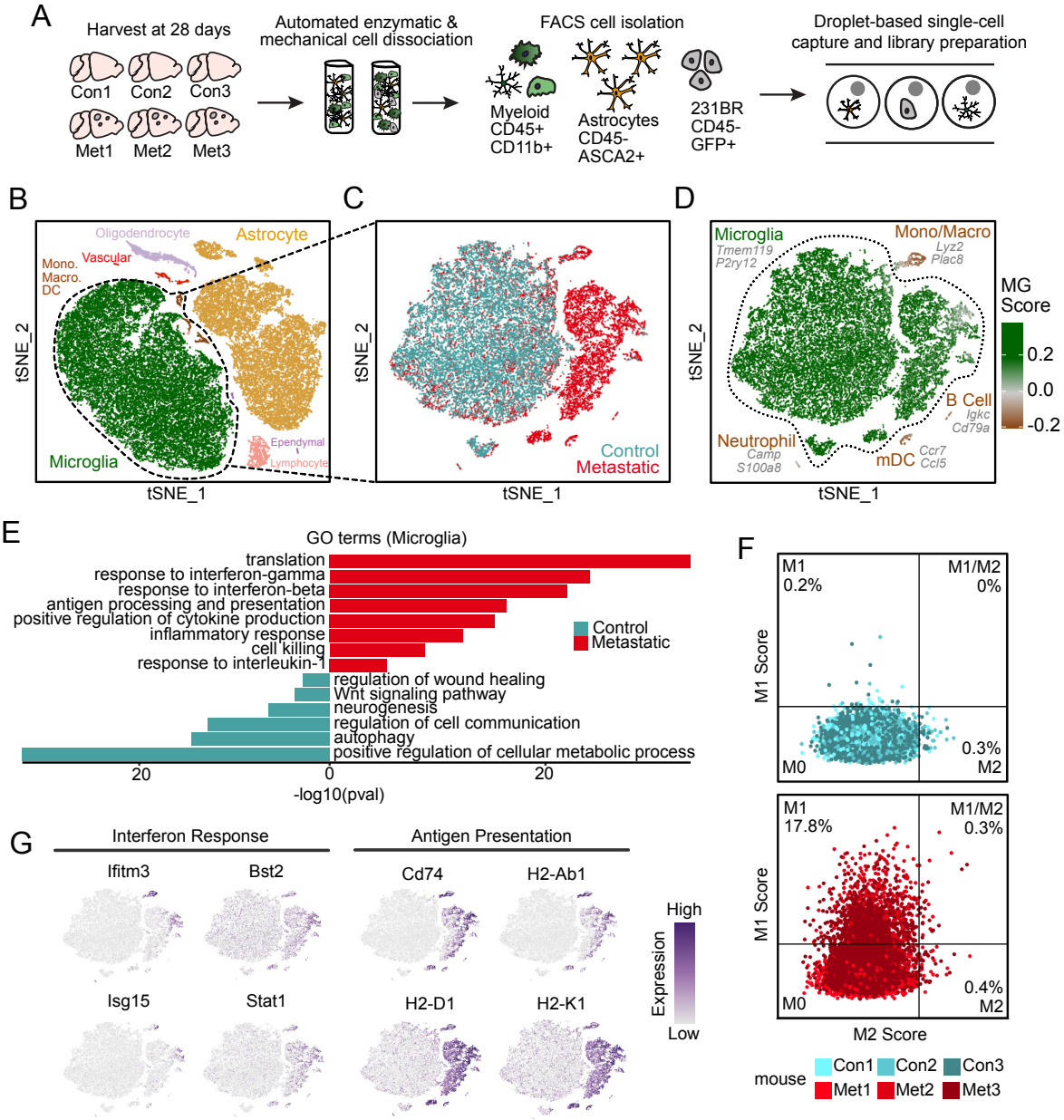

**Figure 2: Microglia display a robust pro-inflammatory response to BCBM** (A) Schematic showing experimental design for generation of scRNA-seq dataset. Foxn1$^{nu/nu}$ mice were injected with 500,000 AcGFP-Luc labeled 231BR cells and brains were harvested 28 days later. Three metastatic (Met1-3) and three control (Con1-3) and brains were digested, and myeloid cells, astrocytes and 231BR cells were isolated by flow cytometry for droplet-based scRNA-seq. (B) tSNE plot shows mouse cells that passed filtering (n=42,891), colored and labeled by cell type. (C) tSNE plot shows clustering of myeloid cells (n=24,348), colored by condition. (D) tSNE plot shows each myeloid cell colored by its MG-score, the core microglia gene signature from Bowman et al (2016). Scores were calculated using the AddModuleScore function in Seurat. Top marker genes (gray) for each myeloid cell type were identified using the Wilcoxon rank sum test in Seurat v3. mDC = mature dendritic cell; Mono/Macro = monocytes and macrophages. (E) Bar plot shows selected top GO terms identified for microglia from control (n=3,083 genes, adj. $p<0.05$) and metastatic (n=609 genes, adj. $p<0.05$) brains. Differentially expressed genes were determined using the Wilcoxon rank sum test. GO terms were determined using MouseMine and select terms with Holm-Bonferroni adjusted *P* values <0.05 were retained. (F) Scatter plots showing gene scores for M1 or M2 macrophage gene signatures in microglia from control and metastatic brains based on the lists from Azizi et al (2018). Control mice were used to draw boundaries for positive or negative M1 and M2 scores. (G) Feature plots show relative expression in each cell for key marker genes associated with top GO terms.

In contrast to astrocytes, tSNE visualization of myeloid cells showed strong separation of control and metastatic conditions **(Fig 2C, Fig S3E)**. Microglia were distinguished from other myeloid populations by scoring cells for the core microglia signature (MG-score) developed by Bowman et al (2016), which compared microglia to BMDMs using bulk RNA-seq from lineage labeled mice (**Fig 2D**)(Bowman et al. 2016). Marker gene analysis confirmed the presence of two major microglia populations *(Tmem119, P2ry12)* **(Fig 1A, Fig 2D, Fig S3A-B),** where one contained microglia from both control and BCBM and the other was almost fully from BCBM **(Fig 2C)**. We also identified two small populations of microglia that display an increased stress response (**Fig S3D)**, which is common post tissue manipulation(O'Flanagan et al. 2019), as well as populations of neutrophils (*Camp*, *S100a9*), monocytes/macrophages (*Ly6c2, Lyz2*), mature dendritic cells (*Ccr7, Flt3*), and B cells (*Igkc, Cd79a*) (**Fig 2D, Fig S3A-D**). The latter were predominantly recovered from metastatic animals **(Fig 2C, Fig S3C),** suggesting they are recruited to the CNS in response to metastatic outgrowth.

To identify gene expression changes in microglia associated with BCBM, from here on called BCBM-response (BCBM-R) microglia, we performed differential gene expression and pathway analyses. Supervised analysis revealed 3,715 genes differentially expressed between microglia from control mice and mice with BCBM (adjusted $p<0.05$). Gene Ontology (GO) analysis of this BCBM-R signature identified 'cytokine production,' 'antigen processing and presentation,' 'cellular response to IL-1,' 'response to IFN-gamma,' and 'response to IFN-beta' as top GO terms, suggesting that microglia undergo a primarily pro-inflammatory response to brain metastasis (**Fig 2E**)(Motenko et al. 2015). This is further supported by scoring each cell for a list of genes associated with pro-inflammatory (also known as M1) versus alternatively activated, anti-inflammatory (M2) macrophage responses (Azizi et al. 2018). Microglia from two of the three mice with BCBM (Met2 and Met3) showed a strong M1 upregulation with minimal M2 upregulation in all mice (**Fig 2F**). Most M2 markers that were expressed in the brain during BCBM (e.g. *Cd163*, *Ccl17*, *Mrc1*) were enriched in non-microglia TAM populations (**Fig S3F**,).

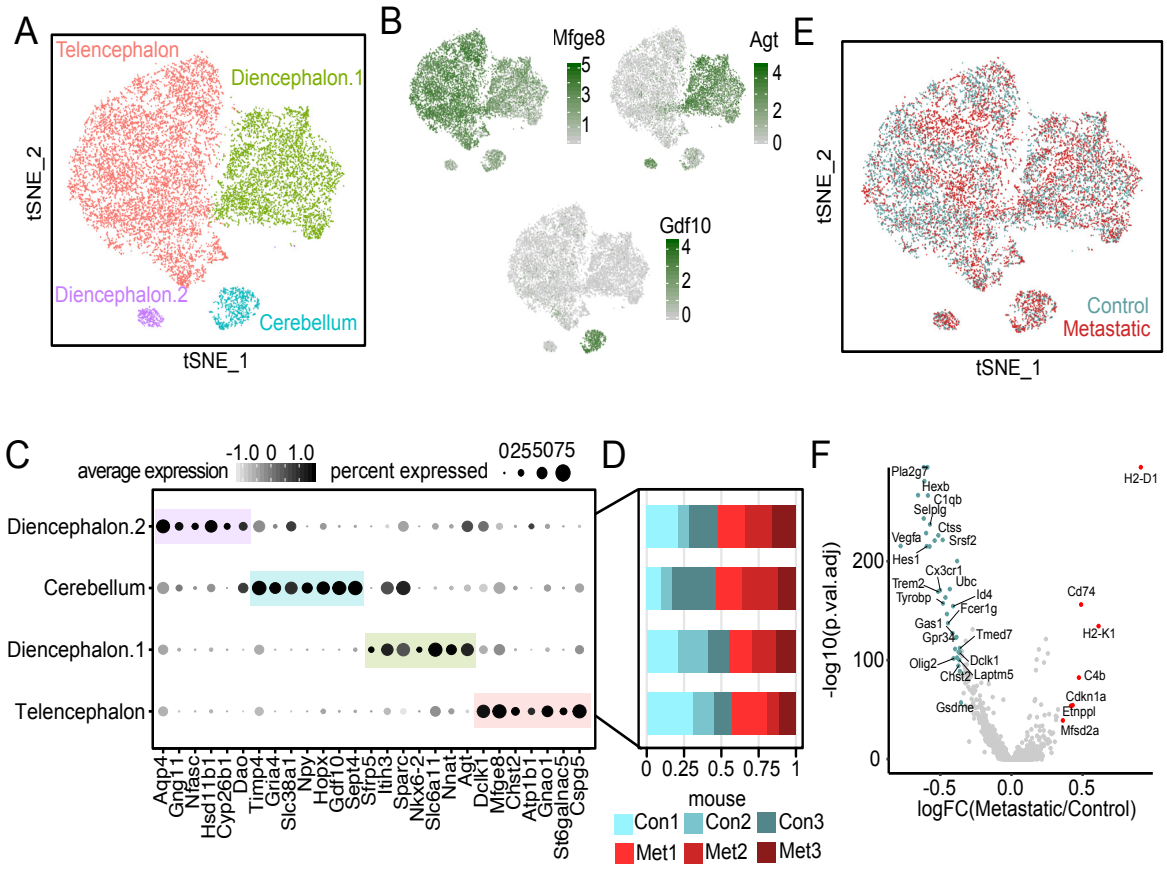


**Figure S2: Astrocytes display regional heterogeneity but limited response to BCBM.** (A) tSNE plot shows clustering of astrocytes (n=15,288) colored and labeled by brain region. (B) Feature plots show relative expression in each cell for key marker genes of astrocytes from the telencephalon (Mfge8), diencephalon (Agt) and cerebellum (Gdf10). (C) Dot plot shows top marker genes for each cluster ranked by average natural logFC and determined by the Wilcoxon rank sum test. Dot size represents the percentage of cells that express the gene, and dot greyscale represents the average expression level. (D) Bar chart shows the frequency of cells contributed by each mouse that localize to each cluster in (C). (E) tSNE plot of astrocytes colored by condition. (F) Volcano plot shows genes differentially expressed (n=6,542) between astrocytes from control and metastatic brains determined by Wilcoxon rank sum test, ($p < 0.01$). Select genes with an absolute value average natural logFC >0.35 are colored and labeled. The y-axis represents the -log10 of Bonferroni corrected *P* values, and the x-axis represents average natural logFC between conditions.

Examination of the genes associated with each GO term showed that BCBM-R microglia upregulate a series of IFN-beta (Type I) response genes typical of an inflammatory response, including *Bst2*, *Ifitm3, Isg15,* and *Stat1* (**Fig 2G**). BCBM-R microglia also upregulate extensive genes

associated with antigen presentation, including the MHC-I genes *H2-D1* and *H2-K1,* the MHC-II genes *H2-Ab1* and *Cd74*, as well as the proteasome activator subunits *Psme1* and *Psme2* (**Fig 2G**). Additionally, they upregulate key pro-inflammatory cytokines *Il1b, Tnf*, *Mif*, and *Spp1*, as well as many chemokines that promote immune cell recruitment(Zlotnik and Yoshie 2000), including *Ccl2* and *Ccl12* for inflammatory monocyte trafficking, *Ccl3*, *Ccl4* and *Ccl5* for macrophage and NK cell migration, and *Cxcl9* and *Cxcl10* for CD8 T cell recruitment for a Th1 response(Griffith, Sokol, and Luster 2014). These data show that microglia mount a robust pro-inflammatory response to BCBM, characterized by increased IFN response genes, cytokine production, and antigen presentation machinery.

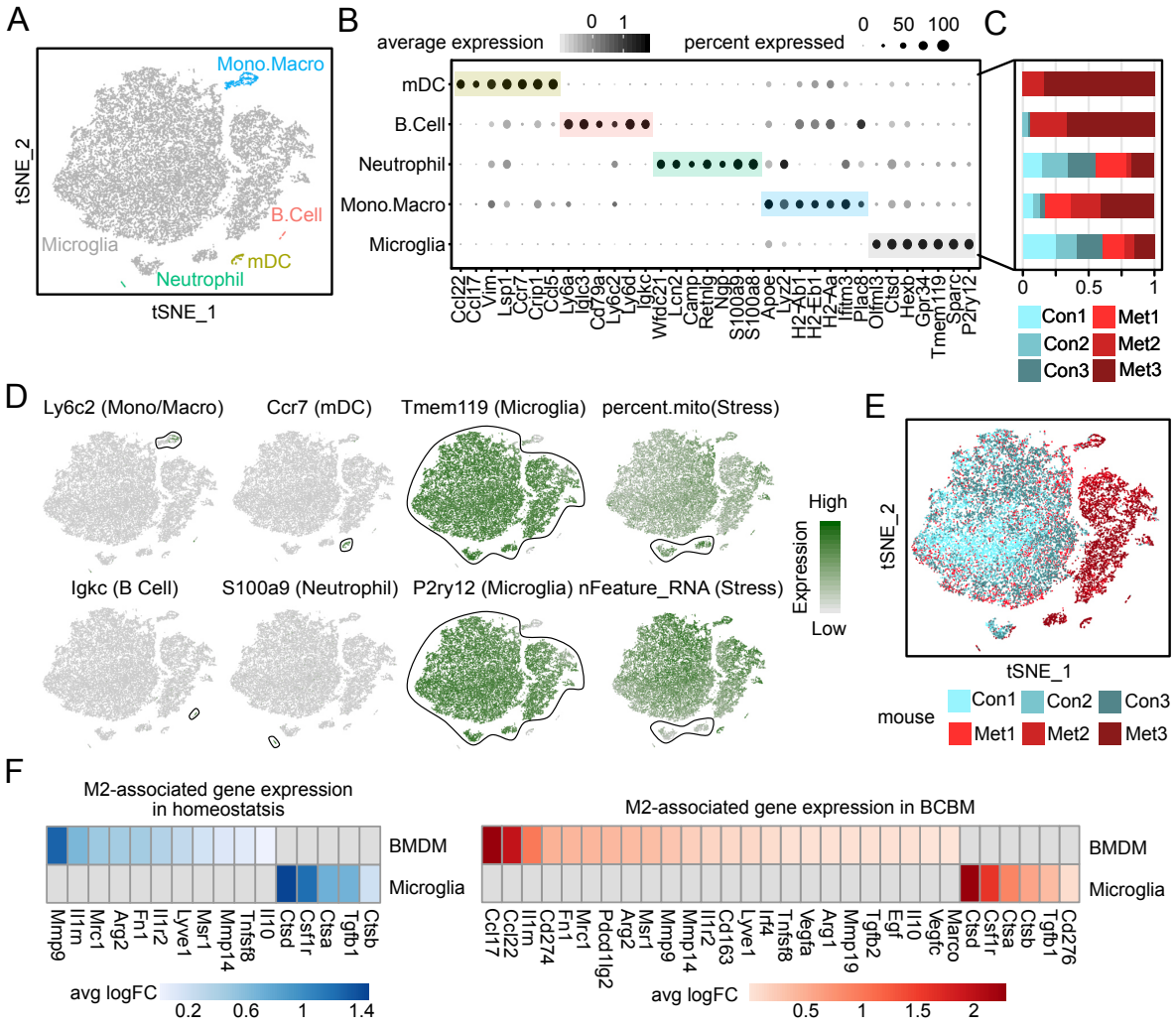


**Figure S3: Identification of myeloid cell types in BCBM.** (A) tSNE plot shows myeloid cells (n=15,288) colored and labeled by cell type. mDC = mature dendritic cell. (B) Dot plot showing top marker genes for each cell type ranked by average natural logFC. Dot size represents the percentage of cells that express the gene, and dot greyscale represents the average expression level. (C) Bar chart showing the frequency of cells contributed by each mouse that localize to each cell type in (B). (D) Feature plots show myeloid cells colored by top lineage-specific marker genes or features. Stressed cells were identified by increased expression of mitochondrial genome (percent.mito) genes, and decreased number of genes detected (nFeature_RNA). (E) tSNE plot of myeloid cells, colored by mouse. (F) Heatmaps show M2-associated genes differentially expressed between microglia and BMDM in homeostasis and BCBM. Differentially expressed genes (unadjusted $P < 0.01$) were determined using the Wilcoxon rank sum test and are displayed as average natural logFC. BMDMs include neutrophils, mono/macro, and mDC.

**The microglia pro-inflammatory response is conserved in diverse BCBM models**

We investigated the microglia pro-inflammatory response in three BCBM models, the human 231BR (Foxn1$^{nu/nu}$) and two mouse immune competent models, 4T1 (BALB/c) and EO771 (C57BL/6) (Contreras-Zárate et al., 2019; Guldner et al., 2020; Lorger and Felding-Habermann, 2010; Taggart et al., 2018). We evaluated protein expression of three representative markers by flow cytometry; the IFN-beta response gene bone marrow stromal antigen 2 (BST2), and major histocompatibility complex II (MHC-II) and CD74 which are critical for antigen presentation(Blasius et al. 2006; Neil, Zang, and Bieniasz 2008; Schröder 2016; Ting and Trowsdale 2002). In the 231BR-Foxn1$^{nu/nu}$ model, tissues were harvested 28 days post injection and microglia were identified by gating on CD45$^{lo}$CD11b$^{+}$Ly6C$^{-}$ cells **(Fig 3A**)(Butovsky et al. 2014; Gosselin et al. 2017). Remarkably, we found a 10-fold increase in the frequency of CD74 (p=0.001) and BST2 (p=0.0001), as well as a 20-fold increase in MHC-II (p=0.04) positive microglia in metastatic (n=14) versus control (n=7) brains **(Fig 3A),** validating our findings from scRNA-seq. In situ IF analysis further showed that the response is specific to microglia proximal to metastatic lesions. Co-staining of CD74 with the microglia-specific marker, transmembrane protein 119 (TMEM119) **(Fig 1A)**, showed that CD74 is specifically upregulated by microglia that directly interface with micrometastatic lesions, while distal microglia remain CD74 negative (**Fig S4A**)(Bennett et al. 2016; Jordão, Sankowski, Brendecke, Locatelli, et al. 2019).

The immune competent models also displayed marked expansion of pro-inflammatory microglia. In the 4T1-BALB/c model, GFP-labeled 4T1 cells were injected intracardiac and tissues were analyzed two weeks later **(Fig S4B,C)**. IF analysis showed infiltration of metastatic lesions with IBA1$^{+}$ cells similar to the 231BR-Foxn1$^{nu/nu}$ model (**Fig S4D**). Analysis of CD45$^{lo}$CD11b$^{+}$Ly6C$^{-}$ microglia by flow cytometry showed a 3.8-fold increase in the frequency of BST2 (p=0.004) and a

3.5-fold increase in MHC-II (p=0.01) in metastatic (n=9) versus control (n=7) brains. In contrast to the human 231BR-Foxn1$^{nu/nu}$ model, there was no increase in the frequency of CD74$^{+}$ cells **(Fig 3B)**. In the EO771-C57BL/6 model, GFP-labeled EO771 cells were injected intracranially according to previously established protocols for this model and analyzed two weeks later **(Fig S4E,F)**(Pyonteck et al. 2013; Yan et al. 2017). IF analysis showed similar infiltration of tumor lesions with IBA1$^{+}$ cells (**Fig S4G**). However, flow cytometry analysis showed a remarkably robust response in this model, with >20 fold increase in CD74 (p=0.003), BST2 (p=0.0004), and MHC-II (p=0.0004) positive microglia from metastatic (n=14) versus PBS-injected control (n=8) brains **(Fig 3C)**. These data show that the microglia pro-inflammatory response is generally conserved in three distinct BCBM models. Of note, the different magnitudes of response observed in each model may reflect known strain-specific differences in immune proclivity. The robust induction of CD74 in the EO771-C57BL/6 model is likely due to the strongly M1-polarizing microenvironment of the C57BL/6 background strain (Zeiner et al., 2018, Zeiner et al. 2015). Furthermore, the less robust response and lack of CD74 induction observed in the 4T1-BALB/c model is consistent with prior reports of proclivity towards Th2 over Th1 immunity in the BALB/c strain(Watanabe et al. 2004).

Finally, we investigated whether the microglia response to metastasis is homogeneous or heterogeneous by determining whether the protein markers are expressed by the same or different cells. We plotted microglia using tSNE to visualize the expression of BST2, MHC-II, and CD74 in each individual cell. Interestingly, this shows extensive overlap of the markers but also reveals subpopulations of microglia that express only one or two of the individual markers **(Fig 3D)**. For example, in the EO771-C57BL/6 model, the IFN-response protein BST2 is only expressed by a subpopulation of CD74$^{+}$MHC-II$^{+}$ microglia. This shows that the microglia response to metastasis is heterogeneous, and raises the question of whether there are discrete substates of microglia that carry out distinct functions in BCBM.

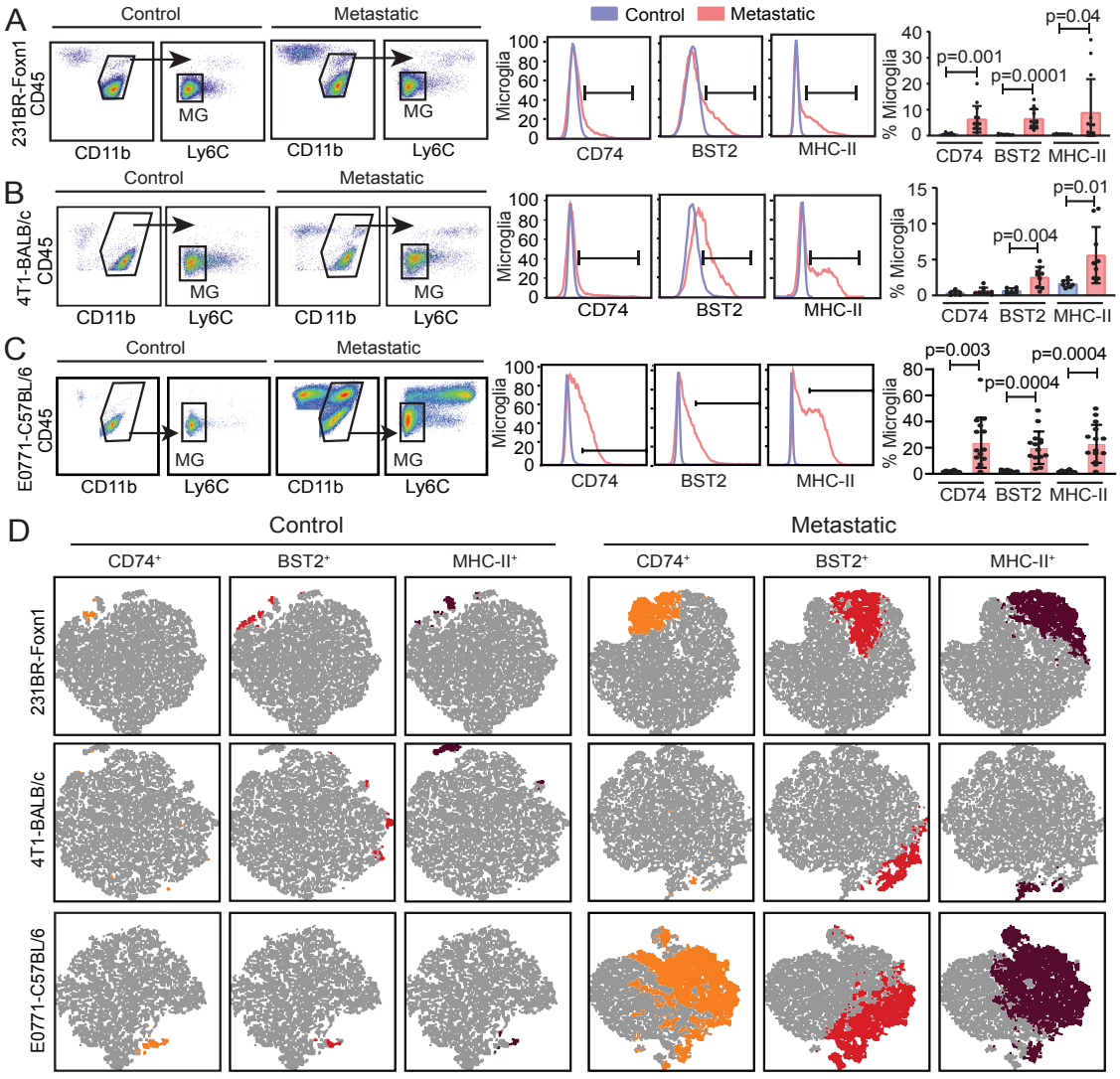


**Figure 3: The microglia pro-inflammatory response is conserved in diverse BCBM models.** (A) Flow cytometry analysis of CD74, BST2 and MHC-II in microglia harvested 28 days post intracardiac injection of 231BR (500,000) cells into Foxn1$^{nu/nu}$ animals. Representative plots show gating for single, live (Zombie$^{neg}$) CD45$^{lo}$CD11b$^{+}$Ly6C$^{-}$ microglia (left panel) followed by analysis for CD74, BST2, and MHC-II (middle panel). Bar graph (right panel) shows the percent of microglia that express each marker in control (n=7) and metastatic (n=14) brains. *P* values were generated by an unpaired two-sided Student's *t*-test, and error bars indicate standard deviation. (B) Flow cytometry analysis of CD74, BST2 and MHC-II in microglia harvested 14 days post intracardiac injection of 4T1-GFP (100,000) cells into BALB/c animals. Representative plots are gated as in 3A. Bar graph (right panel) shows the percent of microglia that express each marker in control (n=7) and metastatic (n=7) brains. *P* values were generated by an unpaired two-sided Student's *t*-test, and error bars indicate standard deviation. (C) Flow cytometry analysis of CD74, BST2 and MHC-II in microglia harvested 14 days post intracranial injection of EO771-GFP (100,000) cells into C57BL/6 animals. Representative plots are gated as in 3A. Bar graph (right panel) shows the percent of microglia that express each marker in control (n=8) and metastatic (n=14) brains. *P* values were generated by an unpaired two-sided Student's *t*-test, and error bars indicate standard deviation. (D) Representative tSNE plots of microglia gated from (A-C). Colored cells indicate those gated as positive for CD74 (orange), BST2 (red) and MHC-II (brown) in the 231BR-Foxn1$^{nu/nu}$, 4T1-BALB/c and EO771-C57BL/6 models.

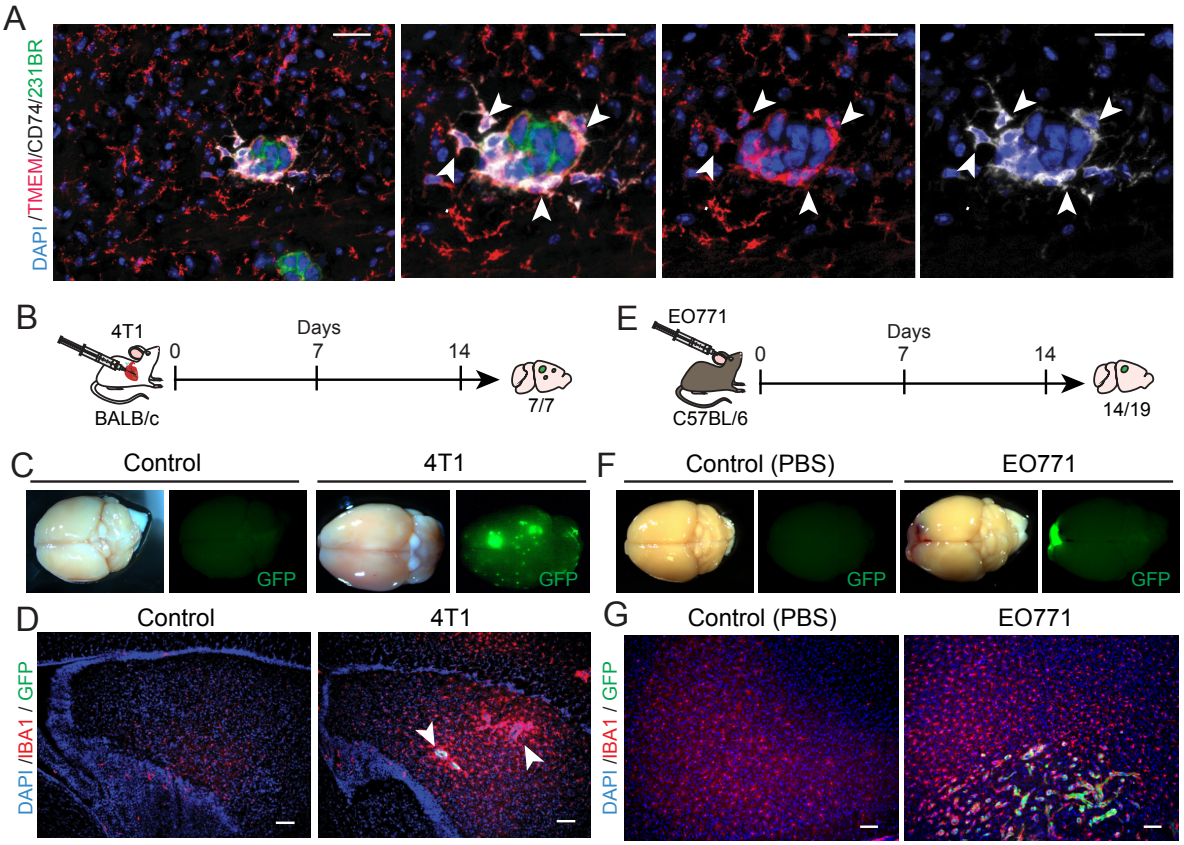


**Figure S4: Disease progression and microglia activation in the 4T1-BALB/c and EO771-C57BL/6 models.** (A) Representative images show IF analysis of CD74 in microglia from the 231BR-Foxn1$^{nu/nu}$ model (n=3). Arrowheads indicate CD74$^{+}$ (white) and TMEM119$^{+}$ (TMEM, red) microglia surrounding metastatic lesions (green). Scale bar= 50µm. (B) Schematic shows 4T1-BABL/c i.c. experimental metastasis model. 100% of animals (7/7) develop brain metastasis two weeks after injection of 100,000 GFP labeled 4T1 cells. (C) Whole mount brightfield and fluorescence microscopy images show metastatic lesions (green) in brains from representative control and metastatic animals. (D) Representative images show IF analysis for IBA1 in control and 4T1-BALB/c metastatic brains. White arrowheads indicate metastatic lesions (green) surrounded by IBA1$^{+}$ (red) microglia. Scale bar = 100µm. (E) Schematic shows EO771-C57BL/6 intracranial injection model. 73% of animals (14/19) develop tumors 2 weeks after injection of 100,000 GFP labeled EO771 cells. (F) Whole mount brightfield and fluorescence microscopy images show tumors (green) in brains from representative control (PBS injected) and tumor-bearing (EO771) animals. (G) Representative images show IF analysis for IBA1 (red) in control and EO771-C57/BL/6 (green) injected brains. Scale bar =

**BCBM-R microglia are heterogeneous and display specialized responses to metastasis**

We further investigated heterogeneity within BCBM-R microglia at the whole transcriptome level using an iterative analysis of our single cell dataset **(Fig 4A)**. To find conserved substates, we first performed sequencing batch correction using Seurat's integration protocol on myeloid cells from all three animals with BCBM and then unbiasedly clustered the integrated cells **(Fig 4A)**(Butler et al. 2018; Stuart et al. 2019). We next used the MG-score to discriminate microglia from other myeloid cells, and subsequently identified BCBM-R microglia by scoring for genes significantly upregulated in our metastatic condition compared to control **(Fig 4A**). This identified two clusters of BCBM-R microglia, which we extracted and further subclustered to investigate heterogeneity **(Fig 4A)**.

Our iterative analysis revealed six distinct subpopulations of BCBM-R microglia, which we named Cycling, IFN responsive, APC, Secretory, Glycolytic, and Homeostatic **(Fig 4B, Appendix A)**. The Homeostatic cluster was named as such because it displayed high levels of canonical microglia markers **(Fig 1A)** (*Tmem119, P2ry12*) and appeared similar to control microglia other than upregulation of MHC-II genes **(Fig 4C,D)**. The Cycling cluster was marked by proliferation genes, such as *Top2a*, *Mki67, and Pcna* **(Fig 4C,D)**. The IFN responsive (*Bst2*, *Ifitm3*, *Isg15*) and APC (*H2-Ab1*, *Cd74*, *Psme2*) clusters showed upregulation of the classic M1 pro-inflammatory genes identified in our BCBM-R signature (**Fig 4C,D)**. The Secretory and Glycolytic clusters displayed unique expression programs not strongly captured by the BCBM-R signature. The Secretory cluster was marked uniquely by cytokines (*Spp1*, *Tnf*, *Il1b, Csf1*) and exosome factors (*Cd9*, *Cd63*) and shared markers of lipid metabolism (*Lpl*, *Apoe*) and phagocytosis (*Trem2*, *Tlr2*) with the APC subpopulation (**Fig 4C,D, Table S3)**. This suggests that the Secretory cluster may represent more classic microglia functions, which include supporting the local inflammatory environment with cytokines and phagocytosing

dead or dying cells, leading to eventual antigen presentation. The Glycolytic cluster showed a shift towards increased glycolysis (*Pkm*, *Ldha, Gapdh*), which is a key feature of inflammatory macrophages and has been shown to increase metabolic output for microglia proliferation and cytokine production during neuroinflammation **(Fig 4C,D)**(Lauro and Limatola 2020; Mills et al. 2016). Interestingly, clustering of control microglia showed very limited heterogeneity, and label transfer in Seurat to the control condition showed that the BCBM-R subclusters were specifically enriched in mice with BCBM with very few cells observed in control mice **(Fig 4E,F)**. This suggests that the microglia substates are unlikely to derive from distinct pre-exisiting microglia cell types. Overall, these data show that the microglia response to BCBM is heterogeneous and represented by diverse specialized responses to metastasis.

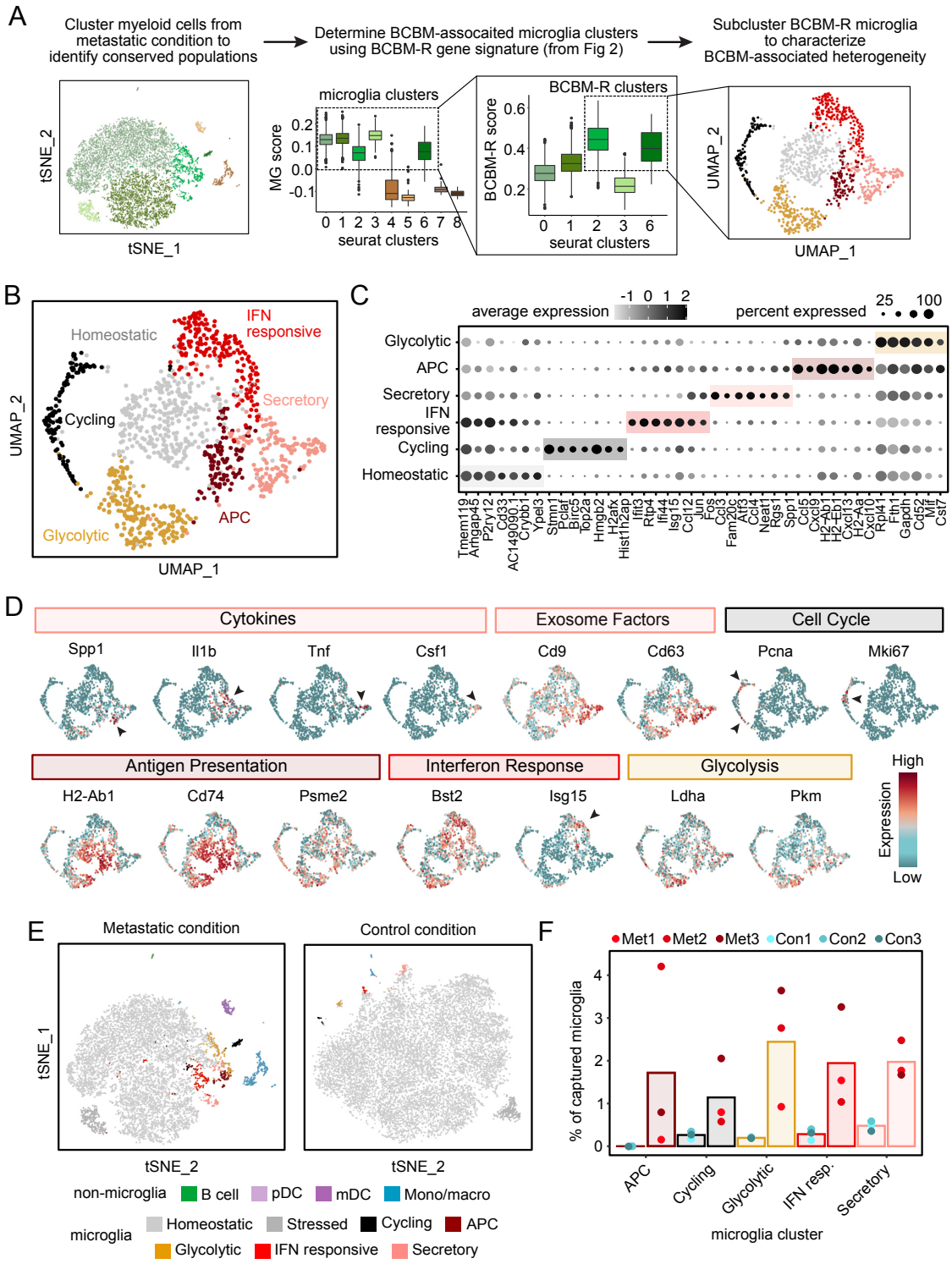
A
Cluster myeloid cells from metastatic condition to identify conserved populations
Determine BCBM-associated microglia clusters using BCBM-R gene signature (from Fig 2)
Subcluster BCBM-R microglia to characterize BCBM-associated heterogeneity
tSNE_2
tSNE_1
microglia clusters
MG score
seurat clusters
BCBM-R clusters
BCBM-R score
UMAP_2
UMAP_1
B
Homeostatic
IFN responsive
Secretory
Cycling
APC
Glycolytic
UMAP_2
UMAP_1
C
average expression
percent expressed
Glycolytic
APC
Secretory
IFN responsive
Cycling
Homeostatic
D
Cytokines
Exosome Factors
Cell Cycle
Spp1
Il1b
Tnf
Csf1
Cd9
Cd63
Pcna
Mki67
Antigen Presentation
Interferon Response
Glycolysis
H2-Ab1
Cd74
Psme2
Bst2
Isg15
Ldha
Pkm
High
Expression
Low
E
Metastatic condition
Control condition
tSNE_1
tSNE_2
non-microglia
B cell
pDC
mDC
Mono/macro
microglia
Homeostatic
Stressed
Cycling
APC
Glycolytic
IFN responsive
Secretory
F
Met1
Met2
Met3
Con1
Con2
Con3
% of captured microglia
APC
Cycling
Glycolytic
IFN resp.
Secretory
microglia cluster

**Figure 4: BCBM-R microglia are heterogeneous and display specialized responses to metastasis.** (A) Schematic overview of iterative approach for BCBM-R microglia selection for subclustering analysis. Briefly, myeloid cells from mice with BCBM were reclustered and microglia were identified using the MG-score. Next, microglia were scored for the BCBM-R microglia signature to identify most robust responders. Finally, these microglia were separated and subclustered to investigate heterogeneity within the BCBM-R microglia. Note that Fig 2 refers to Fig 3.2.1 in this manuscript. (B) UMAP of BCBM-R microglia subpopulations, colored by cluster label. (C) Dot plot shows top marker genes for each cluster ranked by average natural logFC and determined by the Wilcoxon rank sum test. Dot size represents the percentage of cells that express the gene, and dot greyscale represents the average expression level. (D) Feature plots show relative expression in each cell for key marker genes associated with each BCBM-R microglia cluster. Arrows indicate regions of high expression for indicated genes. (E) tSNE plots show myeloid cells from metastatic (left) and control (right) animals, integrated by sequencing batch and colored by cell types and states. Control cell labels were determined using label transfer from the metastatic condition in Seurat v3. (F) Barplots show the average percentage of microglia in each subcluster that came from control and metastatic animals. Points represent

## The pro-inflammatory response to BCBM is conserved in human microglia

To investigate the response of human microglia to BCBM, we developed a humanized mouse model of BCBM which allowed us to control the timing of tumorigenesis and investigate the full range of human microglia responses using scRNA-seq. We utilized the MITRG mouse model in which human *CSF1*, *IL3* and *TPO* are knocked into a *Rag2*$^{-/-}$*Il2rγ*$^{-/-}$ background to support the engraftment of human monocytes and macrophages(Rongvaux et al. 2014). In prior work, transplantation of human induced pluripotency-derived hematopoietic progenitor cells (iHPSCs) into the postnatal brain of MITRG mice was shown to result in differentiation into microglia and CNS macrophages(Hasselmann et al. 2019; McQuade et al. 2018). We injected MITRG mouse pups with GFP-labeled iHPSCs, allowed engraftment for 10 weeks, and injected mCherry-labeled 231BR cells intracardiac **(Fig 5A)**. Control (n=3) and metastatic (n=3) mice were harvested three weeks later and analyzed by whole mount fluorescence microscopy, which confirmed the engraftment of GFP$^{+}$ human microglia and mCherry$^{+}$ 231BR metastases **(Fig S5A)**. Dissociated cells from each sample were indexed using the MULTI-seq method and mouse cells were subsequently removed using anti-mouse MHC-I magnetic beads **(Fig 5A)**(McGinnis et al. 2019). The remaining human cells, consisting of both myeloid and cancer cells, were then captured for sequencing using droplet-based technology **(Fig 5A)**.

Human cells were further distinguished bioinformatically by aligning to a merged human (GRCh38) and mouse (mm10) genome, which identified 25,287 human cells (**Fig S5B**). Cells that were identified as doublets, contained no MULTI-seq index, or displayed a mitochondrial gene percentage >20% were removed from downstream analysis (**Fig S5C**). Clustering and marker gene analysis of the 21,353 human cells that passed filtering showed limited batch effects (**Fig S5D**), and revealed a distinct population of 231BR cells *(VIM)* and several populations of myeloid cells (**Fig 5B, Fig S5E-G, Table S5**). These included clusters of human perivascular macrophages (*CD163*), microglia (*TMEM119*), and a population of proliferating myeloid cells (*MKI67*) (**Fig S5E-G, Table S5**).

Supervised analysis of genes differentially expressed between human microglia from the control and metastatic conditions revealed GO terms similar to the mouse BCBM-R signature, including cytokine response, interferon response, and antigen presentation (**Fig 5C**). Strikingly, subclustering of the BCBM-R human microglia also revealed similar substates as observed in mouse microglia (**Fig 5D**). Using the same iterative analysis as described in **Fig 4A**, we identified four distinct subclusters marked by the same top genes that delineated APC (*HLA-DRB1, PSME2*), IFN responsive (*ISG15, IFITM3*), Secretory (*SPP1, IL1B, CD9, CD63*), and Glycolytic (*LDHA, PKM*) microglia in the mouse (**Fig 5D,E**). Gene scoring for subpopulation markers of each mouse microglia substate further supported this finding and showed that signatures derived from mouse BCBM-R microglia can be directly applied to human microglia to determine their phenotypic state (**Fig 5F**). However, the BCBM-R substates showed less relative expansion in the human than the mouse models (**Fig 5G, Table S5**). IF staining for the APC gene HLA-DR confirmed upregulation at the protein level, and showed the response is strongest in microglia proximal to BCBM lesions (**Fig 5H**). Overall, these data show that human and mouse microglia demonstrate similar pro-inflammatory responses to BCBM.

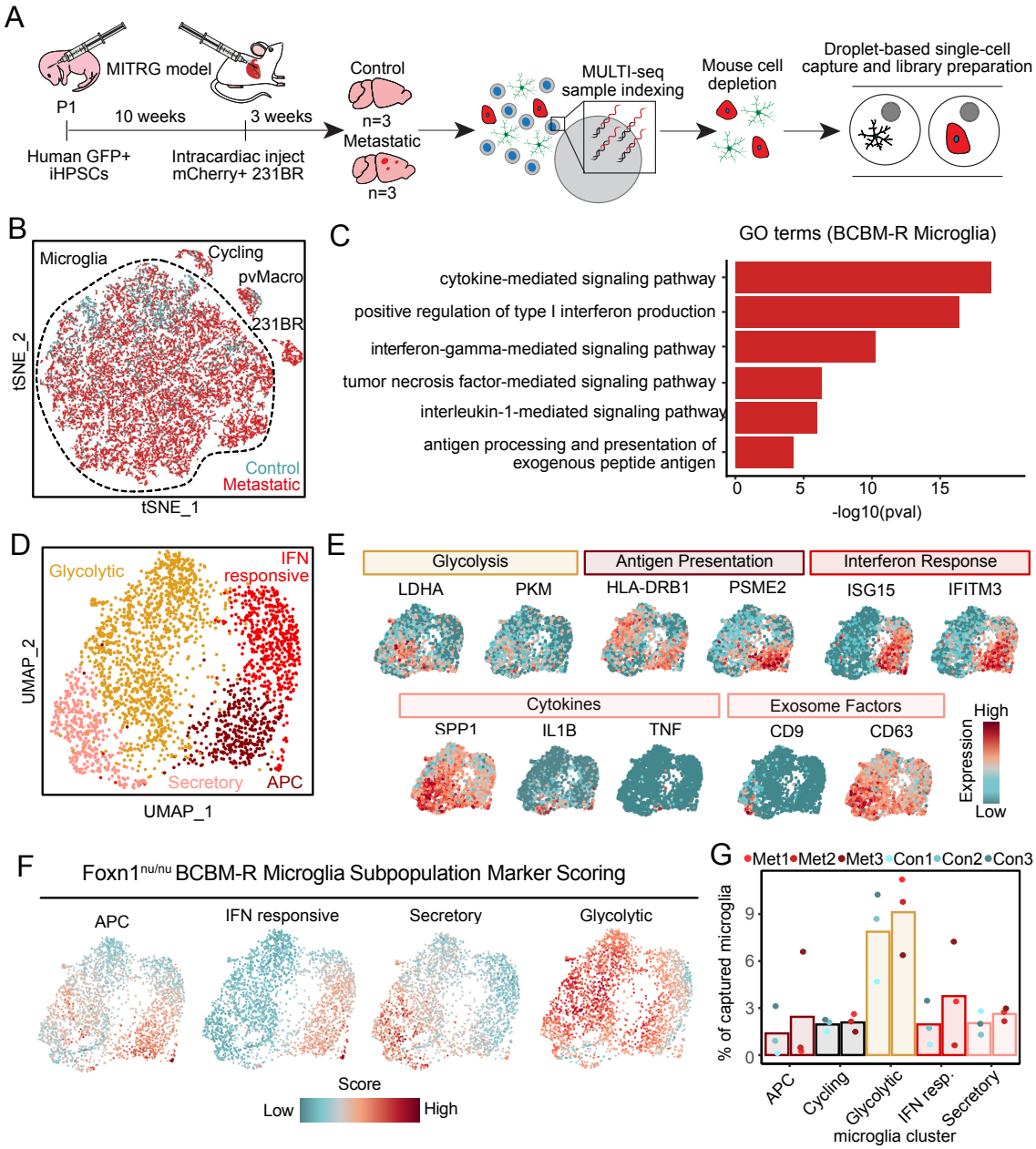
A
MITRG model
P1
10 weeks
3 weeks
Human GFP+ iHPSCs
Intracardiac inject mCherry+ 231BR
Control
n=3
Metastatic
n=3
MULTI-seq sample indexing
Mouse cell depletion
Droplet-based single-cell capture and library preparation
B
Microglia
Cycling
pvMacro
231BR
Control
Metastatic
tSNE_2
tSNE_1
C
GO terms (BCBM-R Microglia)
cytokine-mediated signaling pathway
positive regulation of type I interferon production
interferon-gamma-mediated signaling pathway
tumor necrosis factor-mediated signaling pathway
interleukin-1-mediated signaling pathway
antigen processing and presentation of exogenous peptide antigen
0
5
10
15
-log10(pval)
D
Glycolytic
IFN responsive
Secretory
APC
UMAP_2
UMAP_1
E
Glycolysis
Antigen Presentation
Interferon Response
LDHA
PKM
HLA-DRB1
PSME2
ISG15
IFITM3
Cytokines
Exosome Factors
SPP1
IL1B
TNF
CD9
CD63
High
Expression
Low
F
Foxn1nu/nu BCBM-R Microglia Subpopulation Marker Scoring
APC
IFN responsive
Secretory
Glycolytic
Score
Low
High
G
Met1 Met2 Met3 Con1 Con2 Con3
% of captured microglia
0
3
6
9
APC
Cycling
Glycolytic
IFN resp.
Secretory
microglia cluster
H
DAPI
GFP-hMG
mCherry-231BR
HLA-DR
Merge

**Figure 5: The pro-inflammatory response to BCBM is conserved in human microglia.** (A) Schematic shows experimental design for scRNA-seq of human microglia from humanized MITRG mice transplanted with 231BR cells. MITRG mouse pups were injected with GFP-labeled iHPSCs, aged to 10 weeks and injected i.c. with mCherry-labeled 231BR cells. Brains from control (n=3) and metastatic (n=3) mice were digested to make single cell suspensions three weeks later. Dissociated cells from each sample were indexed using the MULTI-seq method. Mouse cells were removed using anti-mouse MHC-I magnetic beads, and recovered cells were collected and pooled into two samples for scRNA-seq, metastatic and control. (B) tSNE plot shows cells (n=21,353) colored by condition and labeled by cell type. pvMacro=perivascular macrophages. (C) Bar plot shows selected top GO terms identified for microglia from metastatic (n=4,146 genes, adj. $p<0.05$) brains. GO terms were determined using MouseMine and select terms with Holm-Bonferonni adjusted *P* values <0.05 were retained. (D) UMAP of BCBM-R microglia, colored by cluster label. BCBM-R microglia were identified for subclustering analysis using the iterative approach described in **Fig 4.4A**. (E) Feature plots show relative expression in each cell for key marker genes associated with each BCBM-R microglia cluster. (F) UMAP plots show similarity of human and mouse microglia substates by gene scoring analysis. Each human cell from (D) was scored for gene signatures for the mouse microglia substates identified in **Fig 4.4**. Scores were calculated using the AddModuleScore function in Seurat. Gene signatures were translated from mouse to human using the biomaRt package in R. See **Appendix B**. (G) Barplots show the average percentage of microglia in each labeled cluster that came from control and metastatic animals. Points represent individual mice (H) Representative images showing IF analysis of HLA-DR (white) in human microglia (green) near 231BR metastatic cells (mCherry) in transplanted MITRG mice from (A). Scale = 1000μm. hMG=human microglia.

**Microglia demonstrate a potent tumor suppressive effect on BCBM initiation**

Prior work using pharmacologic and genetic depletion strategies has established a clear pro-tumorigenic role for TAMs in BCBM and CNS cancers(Guldner et al. 2020; Qiao et al. 2019; Quail et al. 2016; Yan et al. 2017). These studies primarily utilized CSF1R inhibitors and CX3CR1-targeted genetic ablation strategies that can target microglia as well as other TAM populations, leaving the specific role of microglia unclear(Elmore et al. 2018; Guldner et al. 2020; Spangenberg et al. 2019; Yan et al. 2017). A new genetic model was recently developed that completely lacks microglia due to deletion of the highly conserved super-enhancer in the *Csf1r* locus called the fms-intronic regulatory element (FIRE) (**Fig 6A**)(Rojo et al. 2019). The *Csf1r*$^{\Delta FIRE/\Delta FIRE}$ (FIRE-KO) model lacks microglia while retaining most BAMs and BMDMs, making it an important new tool to specifically explore microglia function in disease(Munro et al. 2020; Rojo et al. 2019).

We investigated the role of microglia in BCBM using FIRE mice and the EO771 model, since both were generated on the C57BL/6 background. We first compared the immune composition of FIRE-KO and FIRE-WT mice. IF and flow cytometry analysis confirmed a complete absence of microglia and retention of BAMs in non tumor-bearing FIRE-KO animals (**Fig 6B,C**). We observed the same phenomenon in tumor-bearing animals by scRNA-seq. CD45$^{+}$ cells from EO771-injected FIRE-WT (n=4) and FIRE-KO (n=4) brains were isolated by flow cytometry, pooled and captured for sequencing using droplet-based technology. Clustering and marker gene analysis of the 10,827 cells that passed quality control filtering identified 11 immune cell types, including one cluster of microglia (**Fig S6A, Table S6**). As expected, microglia were only observed in FIRE-WT mice (**Fig S6A,C)**. The proportions of other immune cell types were also not skewed between FIRE-WT and FIRE-KO mice, excluding this as a confounding variable in future experiments (**Fig S6D)**. Importantly, this contrasts with the Cx3cr1$^{CreERT/+}$:ROSA26i$^{DTR/+}$ model used in previous studies (Guldner et al, 2020). Reanalysis of scRNA-seq data from these mice showed retention and potentially even enrichment of microglia in depleted vs. control animals (**Fig S6B,E**). Depleted animals also

demonstrated a decrease in the proportion of macrophages and Ly6c$^{hi}$ monocytes (**Fig S6E**). Reports of a tumor-promoting role for microglia and brain resident myeloid cells using these mice are therefore confounded since depletion is ineffective. This emphasizes the need for more precise analysis of microglia function in metastasis using the FIRE-KO model.

We next compared BCBM progression in FIRE-KO and FIRE-WT mice. FIRE-WT (n=19) and FIRE-KO (n=14) mice were injected with GFP and luciferase-labeled EO771 cells and monitored by *in vivo* bioluminescence (IVIS) every three days until endpoint at day 14 (**Fig 6D**). Surprisingly, many FIRE-KO mice quickly developed overt clinical symptoms of advanced disease (**Fig 6E,F**). Five of 14 FIRE-KO mice died before endpoint (36% mortality), while all 19 FIRE-WT survived (0% mortality) (p=0.0034) (**Fig 6E**). Surviving FIRE-KO mice displayed >20% decrease in body mass compared to FIRE-WT (p=0.0002), also indicating increased morbidity in mice lacking microglia (**Fig 6F**). Analysis of tumor growth over time by IVIS revealed interesting differences in the kinetics of tumor progression between FIRE-WT and FIRE-KO animals (**Fig 6G-I**). After initial engraftment, we observed a decrease in luciferase signal in eight of 19 FIRE-WT mice over time (42% mice decrease), while signal continued to increase in all 14 FIRE-KO animals (0% mice decrease) (p=0.01036) (**Fig 6G-I**). This indicates that tumors regress in FIRE-WT but not FIRE-KO animals, suggesting microglia suppress BCBM specifically through tumor rejection. Consistent with this hypothesis, *ex vivo* analysis of tumors at endpoint confirmed the presence of tumors in 9/9 of the surviving FIRE-KO animals (eight parenchymal and one meningeal) and 14/19 FIRE-WT mice (**Fig S6F**). But no difference in tumor size was observed between the groups (p=0.77), showing that the absence of microglia attenuates the animal's capacity for tumor rejection rather than for slowing tumor growth (**Fig S6G**). Taken together with previous work, these findings suggest that microglia are innately pro-inflammatory and tumor suppressive, while other TAM populations are anti-inflammatory and tumor promoting. This raises new opportunities to harness the tumor suppressive capacity of

microglia, and highlights the importance of developing therapeutic approaches that target specific TAM populations in order to effectively treat BCBM and other CNS cancers.

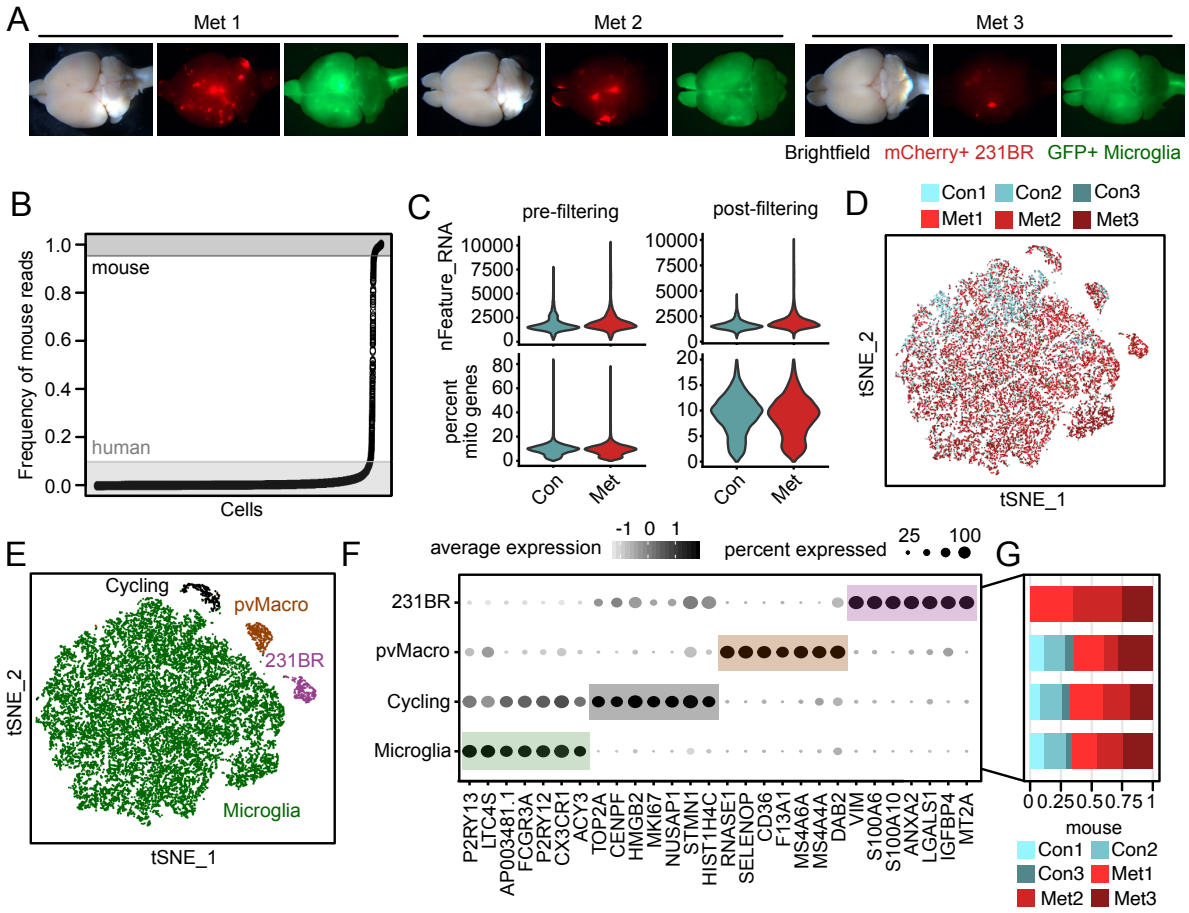


**Figure S5: Experimental design, quality control and cell type identification for scRNA-seq cell libraries from transplanted MITRG mice.** (A) Whole mount brightfield and fluorescence microscopy images show brains from MITRG mice transplanted with GFP-labeled iHPSC cells and mCherry-labeled 231BR cells. See **Fig 4.5.1A**. (B) Identification of mouse and human cells by the frequency of reads that align to the mm10 mouse genome. Cutoffs used to identify mouse cells (>0.95 aligned, n=641 cells), human cells (<0.1 aligned, n=25,287 cells) and doublets (0.1-0.95 aligned, n=387 cells) are shown. (C) Violin plots show cell distributions for key quality control metrics pre- and post- filtering and removal of poor quality cells. Cells were removed that displayed >20% of genes mapped to the mitochondrial genome (percent mito genes). (D) tSNE plot shows clustering of human cells (n=21,353) from MITRG brains colored by mouse ID. Mouse ID was assigned to each cell based on MULTI-seq barcode analysis. (E) tSNE plot shows human cells, colored by cluster and labeled by cell type. pvMacro=perivascular macrophages, Cycling = cycling myeloid cells. (F) Dot plot shows top marker genes for each cell type determined by the Wilcoxon rank sum test and ranked by average natural logFC. Dot size represents the percentage of cells that express the gene, and dot greyscale represents the average expression level. pvMacro=perivascular macrophages. (G) Bar chart shows the frequency of cells contributed by each mouse to the cell types shown in (F).

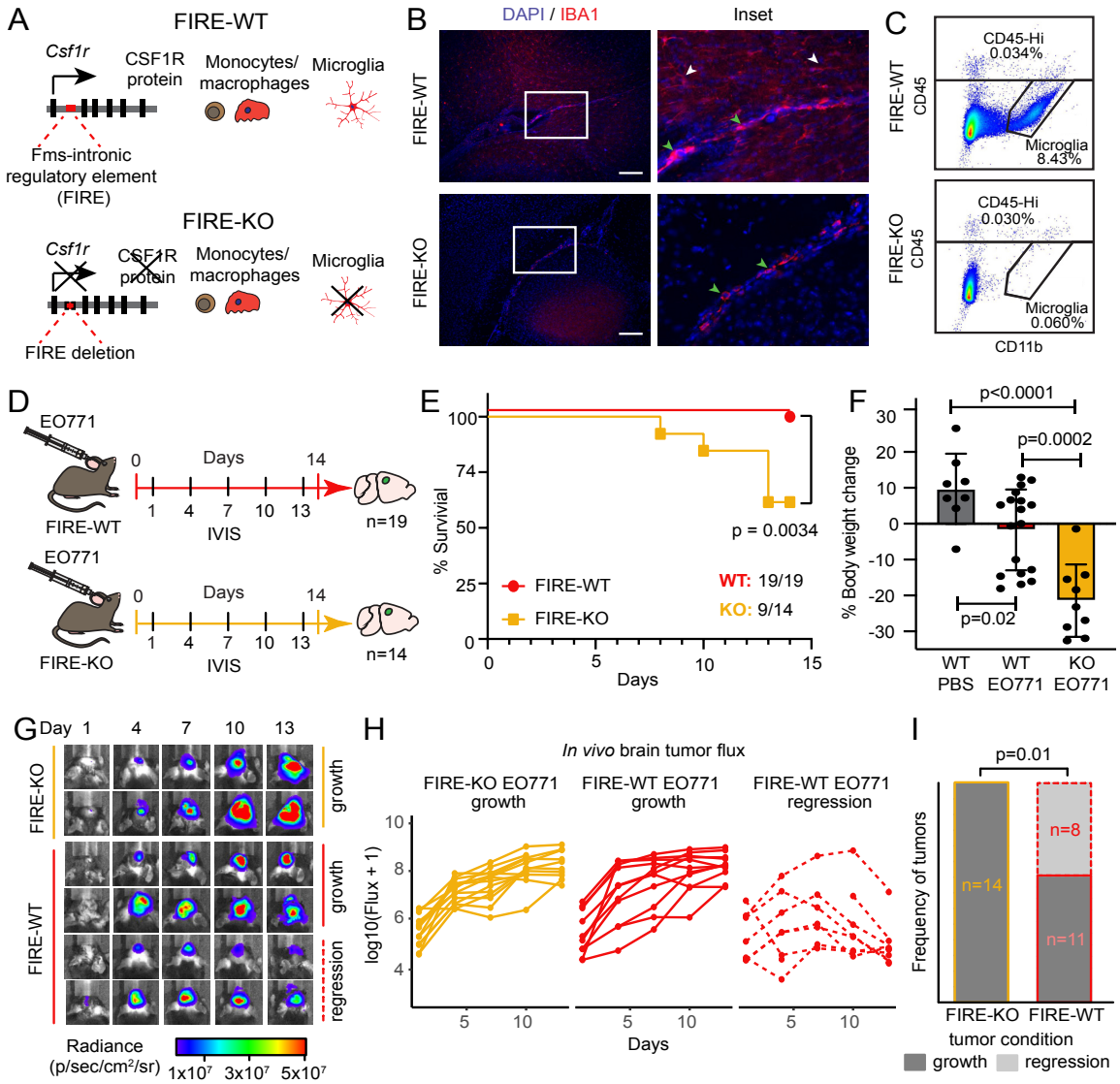
A
FIRE-WT
Csf1r
CSF1R protein
Monocytes/ macrophages
Microglia
Fms-intronic regulatory element (FIRE)
FIRE-KO
FIRE deletion
B
DAPI / IBA1
Inset
FIRE-WT
FIRE-KO
C
CD45-Hi 0.034%
Microglia 8.43%
CD45-Hi 0.030%
Microglia 0.060%
CD45
CD11b
D
EO771
FIRE-WT
FIRE-KO
Days
IVIS
n=19
n=14
E
% Survivial
FIRE-WT
FIRE-KO
p = 0.0034
WT: 19/19
KO: 9/14
Days
F
% Body weight change
p<0.0001
p=0.0002
p=0.02
WT PBS
WT EO771
KO EO771
G
Day 1 4 7 10 13
FIRE-KO
FIRE-WT
growth
regression
Radiance (p/sec/cm²/sr)
1x10⁷ 3x10⁷ 5x10⁷
H
In vivo brain tumor flux
FIRE-KO EO771 growth
FIRE-WT EO771 growth
FIRE-WT EO771 regression
log10(Flux + 1)
Days
I
p=0.01
n=14
n=8
n=11
Frequency of tumors
FIRE-KO FIRE-WT
tumor condition
growth regression

**Figure 6: Microglia demonstrate a potent tumor suppressive effect on BCBM initiation**. (A) Schematic depiction of *Csf1r*$^{\Delta FIRE/\Delta FIRE}$ mouse model. Deletion of FIRE super-enhancer in FIRE-KO mice leads to loss of CSF1R protein expression and lack microglia development. (B) IF staining shows IBA1$^{+}$ cells in FIRE-WT and FIRE-KO mouse brains. Green arrows show choroid plexus macrophages in FIRE-KO and FIRE-WT, and white arrows show microglia only in FIRE-WT. Scale bar = 50μm. (C) Representative flow cytometry plots show the percentage of CD45$^{lo}$CD11b$^{+}$ microglia and CD45$^{hi}$ immune cells gated from live (sytox negative), single cells in FIRE-WT (n=2) and FIRE-KO (n=2) mouse brains. (D) Schematic of experimental design to compare disease progression in FIRE-WT and FIRE-KO mice. FIRE-WT (red, n=19) and FIRE-KO (yellow, n=14) mice were injected intracranially with 100,000 GFP and luciferase labeled EO771 cells. Control FIRE-WT mice (n=8) were also injected with PBS. Animals were imaged for luminescence (IVIS) every three days before dissection at endpoint on day 14. (E) Kaplan-Meier plot shows survival in FIRE-WT (19/19, 100%) and FIRE-KO (9/14, 64%) mice from (D). *P* value determined by log-rank (Mantel-Cox) test. (F) Bar graph shows percentage body weight change for each PBS injected (n= 8), FIRE-WT (n=19), and FIRE-KO (n=9) animal from (D) at day 14 relative to day 0. *P* values determined by unpaired two-sided Student's *t*-test and error bars represent standard deviation. (G) IVIS images show luminescence signal change over time in FIRE-WT and FIRE-KO animals from (D). Representative animals that displayed continuous signal increase (tumor growth, solid line) vs. signal decrease (tumor regression, dashed line) are shown. Pseudocoloring of luminescence shows quantification of radiance (p/sec/cm$^2$/sr). (H) Line graphs show quantification of luminescence signal change over time in all FIRE-WT and FIRE-KO animals from (D). Solid lines indicate animals that demonstrated tumor growth and dashed lines indicate those that showed tumor regression. Growth was defined by signal increase over time, and regression was defined as either baseline signal ($<10^6$) or >5-fold decrease in signal relative to maximum. (I) Bar graph summarizes the frequency of animals that displayed tumor growth and tumor regression in FIRE-WT and FIRE-KO backgrounds. *P* value was determined by Fisher's exact test.

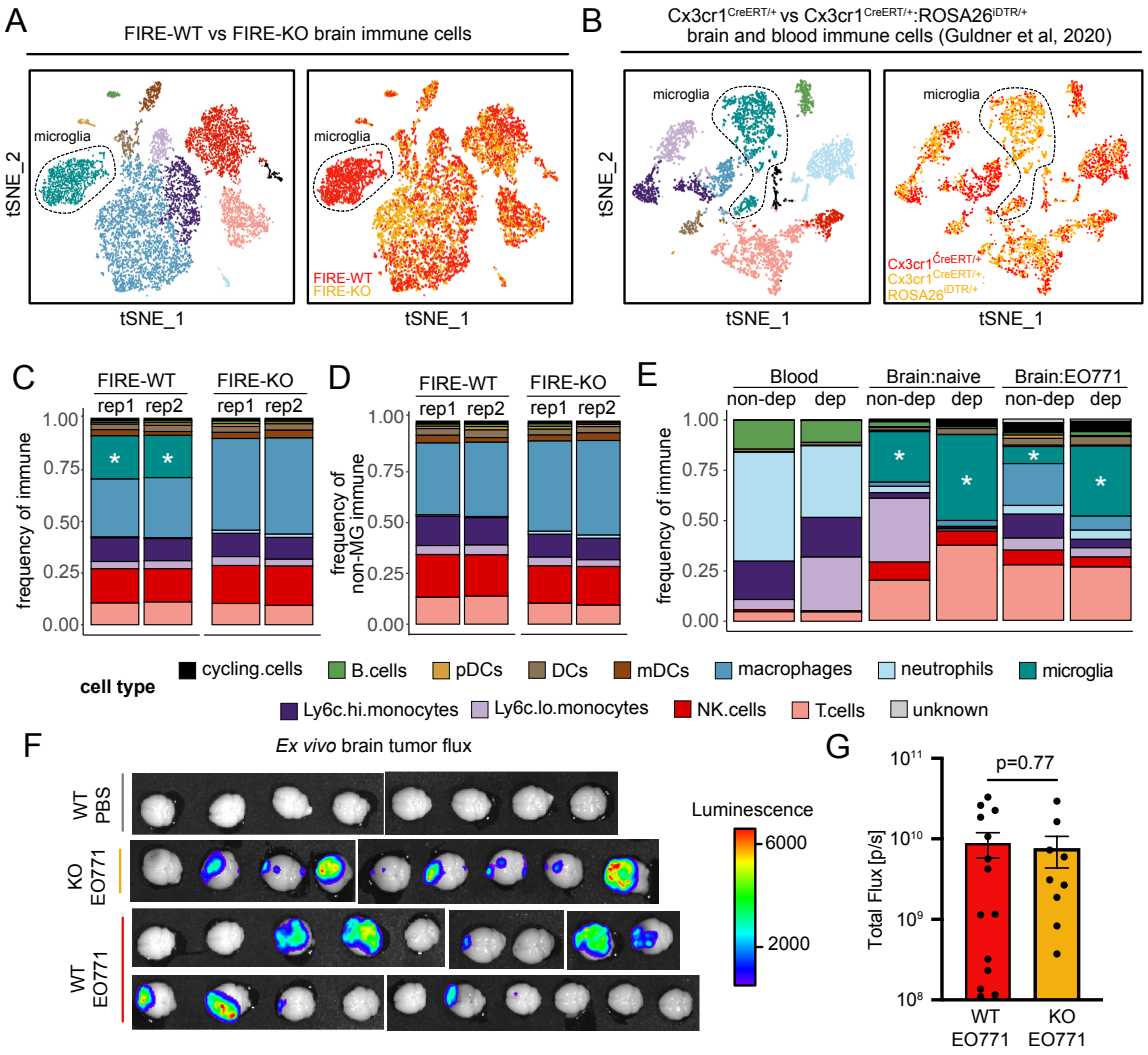
A
FIRE-WT vs FIRE-KO brain immune cells
microglia
tSNE_2
tSNE_1
FIRE-WT
FIRE-KO
B
Cx3cr1CreERT/+ vs Cx3cr1CreERT/+:ROSA26iDTR/+
brain and blood immune cells (Guldner et al, 2020)
Cx3cr1CreERT/+
Cx3cr1CreERT/+:
ROSA26iDTR/+
C
FIRE-WT
FIRE-KO
rep1 rep2
frequency of immune
D
frequency of non-MG immune
E
Blood
Brain:naive
Brain:EO771
non-dep dep
cell type
cycling.cells
B.cells
pDCs
DCs
mDCs
macrophages
neutrophils
microglia
Ly6c.hi.monocytes
Ly6c.lo.monocytes
NK.cells
T.cells
unknown
F
Ex vivo brain tumor flux
WT PBS
KO EO771
WT EO771
Luminescence
6000
2000
G
p=0.77
Total Flux [p/s]
WT EO771
KO EO771

**Figure S6: Analysis of immune cell composition and tumor burden in FIRE-WT and FIRE-KO animals.** (A) ScRNA-seq analysis of immune cell composition in FIRE-WT and FIRE-KO mice. FIRE-WT (n=4) and FIRE-KO (n=4) mice were injected intracranially with 100,000 EO771 cells and harvested 14 days later. Immune cells ($CD45^+$) were isolated by flow cytometry and pooled for droplet-based capture and sequencing. The genotype of each cell was determined using Souporcell. tSNE plots (n=10,827 cells) show cells labeled by cell type (left) and condition (right). (B) tSNE plots show reanalysis of single cell CITE-seq data collected from $Cx3cr1^{CreERT/+}$:$ROSA26i^{DTR/+}$ (CNS-myeloid depleted) and $Cx3cr1^{CreERT/+}$ (control non-depleted) mice as described in Guldner et al, (2020) (GSE139971). Left plot shows cells colored by cell type, which was assigned by label transfer from the FIRE dataset in (A). Right plot shows cells colored by genotype using Souporcell, which were cross-referenced with HTO-barcodes from the CITE-seq dataset. (C) Barplot shows the frequency of each immune cell type captured from FIRE-WT and FIRE-KO mice in the scRNA-seq experiment from (A). Stars indicate microglia. Replicates 1 and 2 indicate two separate pooled samples generated for droplet capture (rep1, n=5,466; rep2, n=5,361). (D) Barplot shows the frequency of each immune cell type as in (C) but excluding microglia (MG). (E) Barplots show the frequency of each immune cell type out of total immune cells captured from the blood and brain of $Cx3cr1^{CreERT/+}$:$ROSA26^{iDTR/+}$ (CNS-myeloid depleted, dep) and $Cx3cr1^{CreERT/+}$ (non-depleted, non-dep) mice from Guldner et al. (2020) (GSE139971) as shown in (B). Cells were assigned to mouse stains and tissue type based on HTO-barcodes from CITE-seq dataset. (F) Ex vivo whole brain luminescence of FIRE-KO (n=9) and FIRE-WT (n=19) mice that survived to endpoint (day 14) relative to PBS injected controls. Pseudocoloring of luminescence is shown in counts(p/s). (G) Barplots show the quantification of total flux for brains shown in (F). *P* value was determined by unpaired two-sided t-test.

## Discussion

We utilized a diverse array of approaches to investigate the role of microglia in the development of BCBM. ScRNA-seq analysis of whole transcriptome profiles allowed us to discriminate brain resident microglia from other types of TAMs, a longstanding challenge in CNS diseases. This enabled us to discover that microglia upregulate a pro-inflammatory (M1) response to BCBM, in contrast to prior dogma that they and other TAMs favor an alternatively activated (M2) response. We further describe heterogeneity within pro-inflammatory microglia, where we find that distinct subpopulations of microglia upregulate programs for proliferation, IFN response, cytokine and exosome secretion, glycolysis, and antigen presentation. We validated the pro-inflammatory response at the protein level in three distinct models of BCBM, as well as in human microglia, showing the response is highly conserved and highlighting its relevance in human BCBM. Most importantly, we utilized the newly developed, genetically engineered FIRE-KO mouse model that completely lack microglia to investigate their impact on metastasis. We find that animals lacking microglia develop more metastasis and less tumor regression than controls. Together with scRNA-seq data, these results show that microglia are pro-inflammatory and anti-tumorigenic, and suggest that microglia suppress metastasis through facilitating tumor rejection. This contrasts with the anti-inflammatory, pro-tumorigenic role previously ascribed to microglia and other TAMs, and raises the prospect of augmenting their tumor suppressive function to treat BCBM.

An interesting phenomenon emerging from our study is a clear conservation of microglia response phenotypes to different diseases of the CNS. Several of the microglia substates we observed in BCBM have been recently reported in single cell studies of microglia in other CNS diseases. In a study comparing microglia diversity during development, aging, and demyelinating injury, Hammond et al. (2019) identified subpopulations of cells that resemble our Glycolytic (*Mif*, *Pkm*), Secretory (*Lpl*, *Ccl4*), IFN responsive (*Ifitm3*, *Isg15*), and Cycling (*Pcna*, *Mki67*) microglia (Hammond

et al. 2019). Interestingly, specific subpopulations of microglia were preferentially found in different contexts; Glycolytic and Secretory were predominantly found in the developing brain, while IFN response and Cycling microglia were enriched in aging and injury. Similar response phenotypes have also been observed in neurodegenerative diseases. Keren-Shaul et al (2017) found that disease-associated microglia (DAMs) in Alzheimer's Disease (AD) and amyotrophic lateral sclerosis (ALS) upregulate the phagocytosis and lipid metabolism associated genes *Apoe*, *Cst7*, *Cd9*, and *Lpl,* which are markers of Secretory microglia in our dataset(Keren-Shaul et al. 2017). They show that DAMs phagocytose plaques and are protective against AD development, suggesting Secretory microglia may perform similar functions in BCBM. Another study of AD found that microglia display distinct phenotypes at progressive stages of disease development, where early response (ER) microglia upregulate markers of proliferation while late response (LR) microglia upregulate IFN response and antigen presentation genes(Mathys et al. 2017). ER and LR microglia share many markers in common with Cycling, IFN responsive, and APC microglia in our study. The overlap of markers between ER and LR microglia led the authors to suggest that they represent progressive stages of microglia activation in response to disease development, raising the question of whether the microglia substates identified in our study also represent different stages of temporal activation. An alternative hypothesis could be that the substates represent microglia responding to different local stimuli that elicit distinct responses. An important question for future studies will be to determine whether the microglia subpopulations carry out distinct functions, and what their independent effects on metastasis are.

Another fascinating phenomenon revealed by our study is the opposing outcomes achieved using different TAM depletion strategies. While we find increased tumor progression in FIRE-KO mice lacking microglia, previous work clearly showed decreased tumor progression following TAM depletion using CSF1R inhibitors and CX3CR1-targeted genetic ablation models(Guldner et al. 2020b; Yan et al. 2017) .There are several possible explanations for these discrepant findings. It is clear that

microglia depletion in the FIRE-KO model is more complete and restricted to microglia than other approaches (Guldner et al., 2020; Yan et al., 2017). Furthermore, microglia cannot rebound and repopulate the brain in FIRE-KO mice as has been observed in other depletion models. The massive cell death produced in the $Cx3cr1^{CreERT/+}$:$ROSA26i^{DTR/+}$ depletion model has also been shown to induce cytokine storm and astrogliosis, which may have confounding effects on tumor growth and the immune response(Bruttger et al. 2015; Han, Harris, and Zhang 2017). Another important distinction in our study is that the FIRE-KO mice lack microglia from birth, while most prior studies targeted TAMs postnatally and after tumor initiation. It is therefore plausible that the timing of depletion impacts the outcome, as microglia and TAMs may become tumor promoting as disease progresses. Regardless, further investigation is critical given that several CSF1R inhibitors targeting TAMs are currently in clinical trials (e.g., NCT02829723, NCT01596751, NCT02401815, NCT02584647) for the treatment of CNS and peripheral cancers. An unintended side effect may be the depletion of protective microglia in the CNS and the creation of a permissive microenvironment for the development of CNS metastasis.

Finally, it will be important in future work to investigate the mechanism by which microglia suppress BCBM outgrowth. Since the absence of microglia in FIRE-KO mice specifically compromises their capacity for tumor rejection, it is compelling to consider that their effect is mediated through promotion of an anti-tumor T cell response. BCBM-R microglia secrete several chemokines that may promote T cell trafficking, as well as pro-inflammatory cytokines that may sustain T cell function once in the brain. BCBM-R microglia also upregulate MHC-I and MHC-II and other machinery for antigen presentation, which could enable them to present tumor neoantigens to CD4 or CD8 T cells in the brain. Previous work has shown that local APCs are critical to skew T cell differentiation and sustain their activation after arrival to the inflamed tissue, so it is reasonable that microglia function as the predominant purveyors of this function in the CNS(Ley 2014). Microglia function could therefore be critical for the efficacy of checkpoint inhibitors in CNS cancers, and boosting their

function with macrophage targeting agents such as CD40 agonists could provide further therapeutic benefit.

# CHAPTER 3: Materials and Methods

## Normal human brain and human BCBM samples

FFPE sections of deidentified normal human brain and resected breast cancer brain metastasis were acquired from University of California Irvine department of Pathology and Laboratory Medicine, experimental tissue shared resource facility and the University of California Davis Pathology Biorepository.

## Cell lines

MDA-MB-231-Br2(Bos et al. 2009) cells stably transduced with membrane targeted AcGFP (rLV.EF1.AcGFP1-Mem-9, ClonTech/Takara Bio, USA, Cat#0019VCT), mCherry (rLV.EF1.mCherry-9, ClonTech/Takara, Cat#0037VCT), and luciferase lentivirus were a generous gift from Ian Smith (Parker, 2017, Bos, 2009). 4T1 cells were purchased from ATCC (ATCC Cat# CRL-2539, RRID:CVCL_0125), stably infected with GFP lentivirus (Santa Cruz Biotechnology, copGFP Control Lentiviral Particles, Cat#sc-108084) at a MOI or 10, and sorted for GFP expression after two weeks growth in culture. EO771 cells were purchased from CH3 Biosystems (Cat. No. 94A001, RRID:CVCL_GR23) and stably infected with pCDH-EF1a-eFFly-eGFP) lentivirus particles. pCDH-EF1a-eFFly-eGFP was a gift from Irmela Jeremias (Addgene plasmid #104834; http://n2t.net/addgene:104834; RRID:Addgene_104834). To produce lentiviral particles, HEK293T cells were transfected with pCDH-EF1a-eFFly-eGFP together with pMD2G and psPAX2 packaging plasmids using Lipofectamine 2000 (Invitrogen, Cat# 11668027). Supernatants containing lentiviral particles were used to infect EO771 cells overnight in the presence of 8 μg/ml polybrene (Sigma-Aldrich, Cat# TR-1003-G). Transduced EO771 cells were sorted on the basis of GFP expression on a BD FACSAria Fusion cell sorter. MDA213-BRm and 4T1 cell lines were cultured in DMEM, 5% FBS, 10U/ml penicillin, 0.1mg/mL streptomycin (GE Healthcare Cat#SV30010), at 37 °C, 5% $CO_2$, 95%

relative humidity. EO771 cells were cultured in RPMI 1640, 5% FBS, 10U/ml penicillin, 0.1mg/mL streptomycin, 10mmol/L HEPES at 37 °C, 5% $CO_2$, 95% relative humidity. Cells were passaged for one-two weeks prior to intracardiac or intracranial injections. All cell lines were authenticated by STR analysis by ATCC prior to injection.

**Mouse strains**

Female Foxn1$^{nu/nu}$ mice (IMSR Cat# JAX:007850, RRID: IMSR_JAX:007850), C57BL/6J (IMSR Cat# JAX:000664, RRID: IMSR_JAX:000664, and BALB/cJ (IMSR Cat# JAX:000651, RRID:IMSR_JAX:000651) were purchased from The Jackson Laboratories. Female MITRG mice (IMSR Cat# JAX:017711, RRID: CVCL_JM19) which are C:129S2- Rag2$^{tm1.1Flv}$ Csf1$^{tm1(CSF1)Flv}$ CSF2/IL3$^{tm1.1(CSF2,IL3)Flv}$ Thpo$^{tm1.1(TPO)Flv}$ Il2rg$^{tm1.1Flv}$/J were bred, housed and maintained by the laboratory of Mathew Blurton-Jones (IACUC protocol #AUP-17-162). *Csf1r*$^{\Delta FIRE/\Delta FIRE}$ (FIRE-KO) and *Csf1r*$^{FIRE/FIRE}$ (FIRE-WT) mice were a gift from Claire Pridans and Mathew Blurton-Jones laboratories and were housed and maintained by the Lawson laboratory. All animals were aged between 5-15 weeks old. When possible, animals were randomized between cages and ages prior to injection of cells or PBS. Only female animals were included in these studies because breast cancer predominantly afflicts women. All animal studies were performed in accordance with an IACUC approved protocol #AUP-19-051 at the University of California Irvine.

**Immunofluorescence analysis of human BCBM samples**

4-µm sections were heated at 65 °C for 30 min, then deparaffinized by two sequential five-min incubations in Histo-Clear (National Diagnostics, #HS-200, Atlanta, Georgia, USA). Tissues were rehydrated with graded solutions of ethanol (100%-50%) and washed in double-distilled $H_2O$ and 1XPBS. Antigen retrieval was performed using a microwave pressure cooker with 10 mM citric acid buffer (0.05% Tween-20, ThermoFisher Scientific Cat#BP337500, pH 6.0). Tissues were blocked in blocking solution (0.1% Tween-20 and 10% Goat Serum in PBS) for 30 min at room

temperature, incubated with primary antibodies diluted in blocking solution at 4 °C overnight, washed in PBS, incubated with secondary antibodies diluted in blocking solution for one hour at room temperature, and washed in PBS. Slides were mounted with VECTASHIELD Antifade Mounting Medium with DAPI (Vector Laboratories, #H-1200, Burlingame, California, USA) and micrographs were taken with the BZ-X700 Keyence fluorescence microscope.

**Generation of BCBM in mice**

For intracardiac injection to establish brain metastasis, as previously described by(Campbell et al. 2012), cells were injected into the left cardiac ventricle of anesthetized mice (300mg/kg Avertin). For 231BR brain metastasis 500,000 cells in 100μL of DPBS were injected into nine week old Foxn1$^{nu/nu}$ or 10 week old MITRG mice. For 4T1 brain metastasis, 100,000 cells were injected into nine week old BALB/cJ mice in 100μL of DPBS. For the intracranial injection of C57BL/6J, 100,000 EO771 cells in a volume of 10μL PBS were injected to a depth of 3mm into the right coronal suture of five week old mice(Pyonteck et al. 2013; Yan et al. 2017). Control mice were injected with 10μL PBS. Injections were replicated in 2-3 cohorts of mice 4-6 mice and in different mouse strains to ensure reproducibility of results.

**Dissection and visualization of mouse BCBM by whole mount fluorescence microscopy**

At endpoint, mice were euthanized and perfused with 50mL of sterile ice cold 1X PBS, 1mg/mL EDTA. The brain was dissected from the cranium and meninges, and then washed in ice cold sterile 1X PBS. To visualize metastasis prior to RNAseq, flow cytometry analysis, or fixation, the whole brain was placed on the dissection microscope (Leica Biosystems, DMC 2900) and imaged for GFP fluorescence and brightfield. Researchers were not blinded to the treatment condition of the mice during dissection, tissue processing or analysis.

**Mouse brain fixation and sectioning**

Dissected brains were drop fixed into 4% PFA, 1X PBS, pH 7.4 overnight at 4°C. Fixed brains were transferred into 30% Sucrose 1X PBS for 24 hours prior to cryosectioning on sliding microtome (Leica Biosystems, SM2010R). Brains were frozen onto the stage for sagittal or coronal sectioning at 40µm thickness using dry ice powder. Serial slices were collected into 1X PBS, 0.05% sodium azide and stored at 4°C for floating section immunostaining.

**Immunofluorescence staining of floating sections**

Brain slices were transferred into a well of a 24 well plate containing 300µL of blocking solution (1X PBS, 5% serum, 0.3% tritonX-100) and placed on an orbital shaker for one hour. Blocking solution was removed and replaced with 500µL of primary antibody diluted in blocking solution and incubated overnight on an orbital shaker at 4°C. The next day, primary antibody was removed, and brain slices were washed with three sequential 500µL washes of blocking solution and incubated with secondary antibody for one hour at room temperature. Brain slices were transferred to a glass slide and mounted with VECTASHIELD Antifade Mounting Medium with DAPI (Vector Laboratories, # H-1200, Burlingame, California, USA). Micrographs were taken with the BZ-X700 Keyence fluorescence microscope and acquisition software. Primary antibodies: Rabbit polyclonal anti-IBA1 diluted 1:500 (RRID: AB_A39504 Wako Cat#019-19741); rat anti-CD74 clone ln1/Cd74 diluted 1:100 (RRID: AB_2632609, BioLegend Cat. No. 151004); rabbit monoclonal anti-TMEM119 clone 28-3 diluted 1:500 (RRID: AB_2800343 (Abcam Cat#Ab209064); anti -Human HLA-DRB clone LN3 diluted 1:200 (Invitrogen, Cat#14-9956-82; RRID: AB_468639). Secondary antibodies diluted 1:400: Goat anti-rabbit IgG conjugated with Alexa Fluor 568 and 488 (ThermoFisher Scientific, RRID: AB_2535730 Cat#A21069 and RRID: AB_2576217 Cat#A11034); Goat anti-rat IgG conjugated with Alexa Fluor 568 and 647 (RRID: AB_2534074 Cat#A11006and RRID: AB_141778 Cat#A21247); Goat anti- hamster conjugated with Alexa Flour 647 (RRID: AB_2535868 Cat#A21451) (Thermo Fisher Scientific Inc., Carlsbad, California, USA).

**Quantification of IBA1 immunofluorescence in Foxn1$^{nu/nu}$ brains**

Four brain tissue sections from control (n=4) and 28-day metastatic (n=4) Foxn1$^{nu/nu}$ mouse brains were stained for IBA1. Micrographs were acquired on the BZ-X700 Keyence fluorescence microscope. Baseline exposure level for IBA1 was established using control brain tissues under 20X magnification. For controls, 8 x 16 µM Z-stack fields of brain parenchyma per mouse were taken. For 231-BR metastatic brains, AcGFP$^{+}$ lesions were located at low magnification (2X), then images at 20X using the same exposure setting as control. Z-stack micrographs were compressed into maximum intensity projection and opened in FIJI (Fiji, RRID:SCR_002285). Regions of interest were quantified for IBA1 fluorescence intensity as the mean fluorescence intensity per pixel for control (n=115), peritumoral (n=127) and distal (n=96). Data was tabulated and analyzed in GraphPad Prism 8 (https://www.graphpad.com/scientific-software/prism/, GraphPad Prism, RRID:SCR_002798).

**Isolation of cells for scRNA-seq**

Single cell suspensions from mouse brains were prepared using the Adult Brain Dissociation Kit, Mouse and Rat (Miltenyi Biotec) with some modifications. Whole dissected brains were chopped into 8 pieces of equal size and placed into C tube (Miltenyi Biotec, Cat#130-093-237) containing enzyme P and A. Brain tissue was digested using gentleMACS Octo Dissociator with heaters operating the Adult brain dissociation protocol. After digestion, the cell suspension was strained over a sterile 70µm strainer (Fisher Scientific, Cat#22363548) and washed with 5mL FACS buffer containing ice cold DMEM/F12, 50mM HEPES, and 2% BSA. After removal of myelin by density centrifugation, the cell pellet was washed and remaining red blood cells were lysed with red blood cell lysis buffer. Cells were then re-suspended in FACS buffer and blocked with anti-CD16/32 for 15 minutes on ice. Next, cells were stained with fluorescent antibodies on ice for 15 minutes shielded from light. The labeled cells were washed with 500µL of FACS buffer and resuspended in 500µL of FACS buffer, strained through 40µm strainer prior to sorting on BD FACSAria Fusion sorter. For sorting of microglia,

astrocytes, and cancer cells, cells were gated for size based on forward and side scatter, single cells, and Sytox Blue viability (Thermofisher, Cat#S34857. All myeloid cells ($CD45^+$ $CD11b^+$) and astrocytes ($CD45^-$, $ACSA2^+$) were sorted from control and metastatic mouse brains into 500µL of chilled FACS buffer. $GFP^+$ 231BR cells were sorted from metastatic brains into 500µL of FACS buffer.

**scRNA-seq of $Foxn1^{nu/nu}$ cells**

FACS isolated mouse microglia cells were centrifuged for 10 minutes at 300g and washed with 0.04% BSA in PBS. A power analysis was performed to estimate the number of cells needed for capture for barcoding for scRNA-seq and identified 5,000- 10,000 cells per mouse. Cells were resuspended to achieve approximately 1,000 cells/µL. Final cell suspensions were counted on the Countess II automated cell counter to determine actual concentration for droplet generation. Cells were loaded onto the 10x Genomics Chromium Single Cell Gene Expression 3' v2 Chemistry kits for GEMs generation. Following the Chromium Single Cell 3' Reagents Kits version 2 user guide (CG00052 Rev B), cells were loaded to achieve approximately 10,000 cells for capture. Libraries were sequenced on the Illumina HiSeq 4000 platform to achieve an average of read depth of 50,000 mean reads per cell. Sequencing reads were aligned utilizing 10x Genomics Cell Ranger Count 3.0.2 to a dual indexed GRCh38 and mm10 reference genome.

**Flow cytometry analysis of microglia from BCBM**

For flow cytometry analysis of metastatic mouse brains, tissue was prepared as for FACS sorting, with the exception that 1mg/mL Collagenase D (Milipore Sigma Cat#11213857001) was used for digestion instead of enzyme P provided in the Adult Brain Dissociation kit. After a single cell suspension was obtained, cells were stained with ZombieNIR viability dye (1:500, BioLegend Cat. No. 423106) in 50µL of ice cold PBS for 15 minutes. Cells were washed with FACS buffer and blocked with anti-CD16/32 antibody diluted in FACS buffer for 15 minutes on ice. Next, cells were stained with fluorescent antibodies for 15 minutes on ice, protected from light. Cells were washed with

500µL FACS buffer and resuspended in 400µL FACS buffer, strained through a 40µm cell strainer and analyzed using BD Fortessa X20.

### *In vitro* differentiation and early postnatal transplantation of iHPCs

Differentiation of Hematopoietic Progenitor Cells from iPSCs (iHPCs) performed according to McQuade et al. (2018). Briefly, iPSCs were first passaged in mTeSR-E8 and on day 0, cells were transferred to Medium A from the STEMdiff Hematopoietic Kit (Stem Cell Technologies, Cat#05310). On day three, flattened endothelial cell colonies were transferred to Medium B for seven additional days while iHPCs began to lift off the colonies. On day 10, non-adherent $CD43^+$ iHPCs were collected by removing medium and cells and at this point, d10-d11 iHPCs can be frozen in Bambanker (Fisher Scientific, Cat#NC9582225) for later transplantation. Cells used for early-postnatal iHPC transplantation were thawed in iPS-Microglia medium (DMEM/F12, 2X insulin-transferrin-selenite, 2X B27, 0.5X N2, 1X glutamax, 1X non-essential amino acids, 400 mM monothioglycerol, and 5 mg/mL human insulin freshly supplemented with 100ng/mL IL-34, 50ng/mL TGFb1, and 25 ng/mL M-CSF (Peprotech, Cat#100-21 ) according to(McQuade et al. 2018) and allowed to recover for 24 h. Early Postnatal Intracerebroventricular Transplantation of iHPCs was performed as described in(Hasselmann et al. 2019). Briefly P1 to P2 MITRG mice placed on ice for two-three min to induce hypothermic anesthesia. Free-hand transplantation was performed using a 30-gauge needle affixed to a 10µL Hamilton syringe, mice received 1µL of iHPCs suspended in sterile 1X DPBS at 31.25-62.5K cells/µL at each injection site (8 sites) totaling 250-500K cells/pup. Bilateral injections were performed at 2/5th of the distance from the lambda suture to each eye, injecting into the lateral ventricles at 3mm and into the overlying anterior cortex at 1mm, and into the posterior cortex in line with the forebrain injection sites, and perpendicular to lambda at a 45° angle. Transplanted pups were then returned to their home cages and weaned at P21.

### Isolation of human xenotransplanted microglia

At 10 weeks old, MITRG mice were injected intracardially with 500,000 mCherry labeled 231BR cells as previously described. 25 days after intracardiac injection and following perfusion with ice cold PBS containing 5μg/ml actinomycin D (act D, Cat#A1410), whole metastatic brains were briefly imaged on a dissection microscope (Leica Biosystems, DMC 2900) for mCherry and GFP intensity. Half brains were then dissected, fixing the left hemisphere in 4% PFA for histology and the right hemisphere was prepped for dissociation as described in(Hasselmann et al. 2019) with modifications. The cerebellum was removed and the whole right hemisphere was stored briefly in RPMI 1640 containing 5μg/mL act D, 10μM triptolide (Sigma-Aldrich, Cat#T3652), and 27.1ug/mL anisomycin (Sigma-Aldrich, Cat#A9789). Tissue dissociation was then performed using the Tumor Dissociation kit, human (Miltenyi Biotec) and the gentleMACS OctoDissociator with heaters (Miltenyi Biotec) according to manufacturer guidelines with modifications. Briefly, tissue was cut into ~1mm pieces and placed into the C-tubes with the kit's enzymes, 5μg/mL act D, 10μM triptolide, and 27.1ug/mL anisomycin and samples were dissociated using the preprogrammed soft tumor protocol. Following enzymatic digestion, samples were strained through a 70μm filter and pelleted by centrifugation. Myelin and debris were removed by resuspending the pellet in 8mL 23% Percoll (GE Healthcare, Cat#45-001-748), overlaid with 2mL of 1X DPBS, spinning at 400xg for 25 minutes at 4°C, with acceleration and brake set to 0, and discarding the myelin band and supernatant.

**MULTI-seq labeling and scRNA-seq of human microglia**

For barcoding of cells from each individual mouse the MULTI-seq lipid- tagged indices for sample multiplexing for scRNAseq protocol was followed(McGinnis et al. 2019). Lipid anchor and co-anchor reagents were a generous gift from Zev Gartner, and barcode index oligos were purchased from Integrated DNA Technologies, Inc. Cells were resuspended and washed with 15 mL cold DPBS and pelleted by centrifugation (10 minutes, 400xg). The supernatant was discarded, and cells were resuspended in 180μL of DPBS. 20μL of 20μM Anchor:Barcode solution was added to a final concentration of 2μM, and incubated on ice for five minutes. Next 20μL of 20μM Co-Anchor solution

was added, gently mixed and incubated for five minutes. After incubation 1mL 1% BSA in DPBS was added and cells were pelleted by centrifugation (five minutes, 400xg). Finally, the supernatant was removed and washed a second time with 1mL 1% BSA in PBS and pelleted by centrifugation (5 minutes, 400xg). Next, mouse cell removal was performed by resuspending cell pellets in 160μL FACS buffer (0.5% BSA in 1X DPBS) + 40μL Mouse cell removal beads (Miltenyi Biotec) and incubated at 4°C for 15 minutes. Mouse and human cells were then separated using LS columns and the MidiMACs separator (Miltenyi Biotec) and the human cells were collected in the flow through. Human cells were pelleted via centrifugation (10 minutes, 400xg) and control samples and metastatic samples were then pooled separately. Cells were resuspended to ~1,000 cells per microliter in FACS buffer, according to counts performed on a hemocytometer.

**ScRNA-seq of MITRG human microglia**

Final cell suspensions were counted on the Countess II automated cell counter to determine actual concentration for droplet generation. Cells were loaded onto the 10x Genomics Chromium Single Cell Gene Expression 3' v3 Chemistry kits for GEMs generation. Following the Chromium Single Cell 3' Reagents Kits version 3 user guide (CG000183 Rev C), cells were loaded to achieve approximately 10,000 cells for capture. MULTI-seq barcode libraries were prepared according to the MULTI-seq protocol(McGinnis et al. 2019). Libraries were sequenced on the Illumina NovaSeq 6000 platform to achieve an average read depth of 50,000 mean reads per cell for 3' gene expression libraries. MULTI-seq barcode libraries were sequenced to achieve at least 5,000 reads per cell. Sequencing reads were aligned utilizing 10x Genomics Cell Ranger Count 3.1.0 to a dual indexed GRCh38 and mm10 reference genome. All libraries were aggregated using 10x Genomics Cell Ranger Aggr 3.1.0, to normalize the number of mean reads per cells. MULTI-seq reads were processed according to the MULTI-seq protocol (https://github.com/chris-mcginnis-ucsf/MULTI-seq).

**Analysis of BCBM in FIRE mice**

Four-six week old *Csf1r*$^{\Delta FIRE/\Delta FIRE}$ (FIRE-KO) and *Csf1r*$^{FIRE/FIRE}$ (FIRE-WT) mice were injected intracranially in the right coronal suture with 100,000 enhanced GFP and luciferase labeled EO771 cells as previously described. To monitor brain tumor growth *in vivo*, mice were imaged for luciferase luminescence one day after injection, and every three days thereafter until endpoint. Imaged mice were anesthetized via isoflurane inhalant and administered 300µg D-Luciferin (Goldbio), intraperitoneally, in sterile DPBS. Following a 10-minute incubation, mice were imaged for bioluminescence for six minutes utilizing an IVIS Lumina III In Vivo Imaging System (Xenogen). Regions of interest were selected around each brain and average photon flux (total photons/s-cm$^2$) was recorded using Living Image analysis software (**RRID:SCR_014247,** http://www.perkinelmer.com/catalog/category/id/living%20image%20software) and average background flux subtracted. On day 14, mice were weighed, euthanized and dissected and the whole brains were removed and placed in a 24 well tissue culture plate submerged in ice cold PBS with D-Luciferin (1.5 mg/mL, Goldbio, Cat# LUCK-1G). After 10 minutes incubation, whole brains were removed from the solution and placed on a black plastic card and imaged for luminescence for 1 second. A region of interest was drawn around each brain and the total flux (ptotal photons/s-cm$^2$) was recorded for analysis.

**Immune cell isolation and scRNA-seq of FIRE mice**

FIRE-WT and FIRE-KO mice were injected intracranially with 100,000 EO771 cells and dissected after two weeks. For scRNAseq, four FIRE-KO bearing visible brian tumors, two FIRE-WT bearing visible brain tumors and two FIRE-WT without visible brain tumors were euthanized as previously described and brains were digested using our standard GentleMACS protocol for FACS isolation. After removal of myelin using debris removal solution (Miltenyi Biotec) cells from all 8 mice were pooled and stained for CD45 and viability. Single, live CD45$^+$ cells, including CD45 low microglia, were sorted into FACS buffer and subjected to 10X barcoding as previously described. Sequencing reads were then aligned utilizing 10x Genomics Cell Ranger Count 3.1.0 to a mm10 reference genome.

## Quantification and Statistical Analysis

### GSE139971 CITE-seq realignment

FASTQ files associated with GSE139971 HTO barcodes and mRNA samples were downloaded using 'fastq-dump --split-files --origfmt --gzip' and realigned using CITE-seq-Count 1.4.3 and Cell Ranger 3.0.2 respectively. HTO barcodes were assigned to cells using the procedure in Seurat v3 based on the umi count matrix output from CITE-seq-Count.

### Souporcell genotyping

Genotyping was performed using Souporcell (Heaton et al, 2020) for GSE139971 and FIRE samples. For GSE139971, three genotype clusters were assigned and HTO barcodes were used to assign the genotypes to EO771, Cx3cr1$^{CreERT/+}$, or Cx3cr1$^{CreERT/+}$:ROSA26i$^{DTR/+}$. For FIRE samples, 2 genotype clusters were assigned and microglia presence, as determined by gene expression, was used to assign clusters to FIRE-WT (+microglia) and FIRE-KO (-microglia). Notably, using genotyping to label Cx3cr1$^{CreERT/+}$ and Cx3cr1$^{CreERT/+}$:ROSA26i$^{DTR/+}$ mice in this dataset had a high concordance with the expected antibody sample barcodes (matching in 96.7% of cells), which supports our use of this method to label FIRE-WT and FIRE-KO cells.

### Human/mouse cell assignment

Cells were aligned to a merged GRCh38/mm10 genome using Cell Ranger v3. Cells were then determined to be from mouse or human based on the frequency of reads aligning to the mouse genome with very low quality cells with <200 genes (nFeature_RNA) filtered before estimating. Cells were called as mouse for all cells above the top elbow in the mouse read mapping frequency plot (>0.875 for Foxn1$^{nu/nu}$ data; >0.95 for MITRG data), human for all cells below the bottom elbow (<0.05 for Foxn1$^{nu/nu}$ data; <0.1 for MITRG data), and any other cells were discarded as doublets or poor

quality. Any counts for GRCh38 genes in the cells called as mouse were removed from the expression matrix and vice versa for mm10 genes in human cells.

**Quality control metrics**

Cells for the Foxn1$^{nu/nu}$ cell type identification analysis were filtered to have between 500 and 2000 genes (nFeature_RNA) and <10% mitochondrial genome reads (percent.mito) in any retained cell. Putative microglia/astrocyte doublet clusters with marker gene co-expression were removed from the Foxn1$^{nu/nu}$ microenvironment. This cell set was then used for subset myeloid and astrocyte analyses based on the cell type labels. Cells were further filtered for the myeloid analysis to have <5% percent.mito and low ribosomal expression (<10% of their transcriptome representing Rps and Rpl genes). An additional small cluster of putative microglia/astrocyte doublets was removed from the final astrocyte analysis. Cells for the 231BR analysis in Foxn1$^{nu/nu}$ were filtered to have >2500 genes (nFeature_RNA), <60000 reads (nCount_RNA), and <10% percent.mito. Cells for the MITRG analysis were filtered to have <20% percent.mtio. Doublets and empty gems (Negative) were also removed from the MITRG analysis based on MULTI-Seq barcoding label assignment from the R package deMULTIplex. Cell cycle signatures (S.Score and G2M.Score, determined by CellCycleScoring in Seurat) were regressed from the data for the 231BR analysis as well as the MITRG analysis before clustering and dimensionality reduction. FIRE immune cells were first filtered to have >200 and <3500 genes (nFeature_RNA) and <7.5% percent.mito, low quality clusters were removed separately to conserve cell types with low gene expression (e.g. neutrophils), and doublets were removed based on Sourporcell labels(Heaton et al. 2020). GSE139971 samples were filtered to be singlets by both HTO-barcode and Souporcell assignment and only clusters that expressed CD45 (*Ptprc)* and were not assigned to the EO771 cluster by Souporcell genotype were kept for downstream analysis.

**Clustering and differential expression**

Main clustering and dimensionality reductions were performed in Seurat using the default Louvain and tSNE methods respectively. UMAP was used for dimensionality reductions in microglia subclustering analyses to better visualize global relationships. Some datasets were integrated using the mutual kNN algorithm adaptation in Seurat before these steps. Specifically, integration was performed on the Foxn1$^{nu/nu}$ full microenvironment and astrocyte analyses by sequencing batch (Con1:Met1, Con2:Con3, Met2:Met3) and the subclustering analyses for metastatic and control Foxn1$^{nu/nu}$ myeloid cells were also batch integrated. Integrated analyses used the "vst" selection method with nfeatures=2000 for FindVariableFeatures and dims=1:30 for FindIntegrationAnchors and IntegrateData. Differential expression analyses were run on the RNA assay in Seurat with FindAllMarkers/FindMarkers using the Wilcoxon rank sum test and adjusted *P* values represent the Bonferroni corrected values for all single-cell analyses. For all samples except GSE139971, cell types and states were assigned to clusters manually based on gene expression profiles. GSE139971 cell type labels were determined by label transfer for FIRE immune cells using the standard pipeline in Seurat v3.

**GO term analysis and gene scoring**

GO term analyses were performed using the MouseMine(Motenko et al. 2015) web portal with list input for M. musculus with the default background population for mouse analyses and using the Enrichr portal (E. Y. Chen et al. 2013; Kuleshov et al. 2016) with a gene list input. Gene inputs for each condition included only genes considered differentially expressed with a Bonferroni adjusted *P* value < 0.05 from the Wilcoxon rank sum test. Specific GO terms were then selected from the Gene Ontology Enrichment section for biological_process with Holm-Bonferroni adjusted *P* value < 0.05 in MouseMine or the GO Biological Process 2018 list in Enrichr with unadjusted *P* value < 0.05. All gene scoring on single-cell data was performed in Seurat using the AddModuleScore function with default parameters. MG-score gene list was taken directly as the Core MG list from Table S4 in(Bowman et al. 2016). M1 and M2 gene signatures were translated to mouse from Table S4 of(Azizi et al. 2018)

using the biomaRt package in R. Microglia subcluster profiles from Foxn1$^{nu/nu}$ mice were taken as top marker genes (logFC > 0.5) for each cluster compared to all other myeloid cells from mice with BCBM, and translated to human using the biomaRt package.

# Chapter 4: Conclusions and Future Directions

This work began with a simple observation that IBA1+ cells accumulate within BCBM. At the time little was known about their origins and function in the broader immune response to BCBM. In the intervening years, advances in technology enabled new discoveries in our lab and other that made this study and our original findings possible. In particular, the application of single cell RNA sequencing technologies made it possible to observe changes in rare populations of microglia in the tumor microenvironment, revealing their pro-inflammatory response to BCBM. Applying new mouse models in this study, including iPS derived humanized microglia and FIRE-KO allowed us to more authentically study the response of human microglia to BCBM, and the consequences of complete microglia loss on BCBM. Taken together our data shows the importance of the microglia response to BCBM initiation. As in all research, answers lead to more questions. For example, we do not know if microglia control metastatic growth directly or indirectly, we do not know the functional consequences of their heterogeneous response that our scRNA-seq and flow cytometry uncovered or how to therapeutically target this response to enhance their anti-tumor function. These are important questions to pursue in future work.

### Mechanism of microglia regulation of BCBM outgrowth

Do microglia suppress BCBM outgrowth directly through tumoricidal activities such as iNOS production and phagocytosis, or indirectly through recruitment of cytotoxic T and NK cells to the tumor environment, T cell priming, or supporting these effectors through pro-inflammatory cytokine production and antigen presentation. I have begun to address these questions about the mechanism of microglia suppression of BCBM using *in vivo* mouse studies, and *ex vivo* analysis of cytokine production by microglia. Based on the observations that microglia deficient FIRE-KO mice all succumb to lethal metastasis by day 14, while almost half the FIRE-WT mice have some levels of tumor regression beginning day 7 after tumor injection, I hypothesized that microglia are important

for T and NK response during BCBM initiation. I do not strongly support they hypothesis that microglia directly suppress metastatic outgrowth through tumoricidal activities because even in microglia replete animals, tumor outgrowth occurs. To test the hypothesis that microglia support T/NK cell responses to BCBM, FIRE-KO and FIRE-WT mice were injected intracranially with EO771-GFP and luciferase labeled cells and monitored for tumor growth by IVIS (**Fig 7A**)**.** Tumors were detectable in all injected mice above background and un-injected control, and progressively grew in all but one FIRE-WT subject (**Fig 7B**). Mice were dissected on day 7 to assess the immune response to metastasis initiation in FIRE-WT vs FIRE-KO. Brains were analyzed for tumor burden by IVIS and then dissociated into single cell suspension for flow cytometry analysis of T and NK cell infiltration (**Fig 7C-D**). *Ex vivo* IVIS analysis of tumor burden revealed that FIRE-KO brains had slightly larger tumors, although this was not a significant difference (**Fig 7C**). Consistent with my hypothesis, flow cytometry analysis revealed significantly fewer CD3+, NK1.1, and CD3+NK1.1+ T, NK and NKT cells in FIRE-KO mice compared to WT (**Fig 7D**). This resulted in fewer total numbers of CD4+ and CD8+ T cells (**Fig 7E**). To assess function, cell surface expression of CD107a, a marker of cytotoxic NK and CD8+ T cell degranulation, was assessed by flow cytometry analysis (Betts et al. 2003). Consistent with reduced numbers of T and NK cells the total number of CD107a+ NK1.1+ and CD8+ T cells was significantly lower in microglia deficient FIRE-KO mice compared to WT (**Fig 7F**). Interestingly, there was no significant difference in numbers of Ly6C+ CD11b+ monocytes or Foxp3+ T regulatory cells in FIRE-WT vs FIRE-KO (data not shown), indicating that microglia may be critically important for the early recruitment of conventional CD4+ and CD8+ T cells and NK cells during BCBM initiation. This data helps explain why FIRE-KO mice succumb to lethal metastasis earlier than WT mice. Due to a lack of microglia, there is a delay in the early response of cytotoxic immune effectors, namely CD8+ and NK lymphocytes. As a result, tumors in FIRE-KO mice grow rapidly in the initial stages and the immune system is not able to catch up to control the outgrowth. In follow up experiments, I plan to perform multiplex cytokine screening, ELISpot and ELISA assays of microglia from metastatic

mouse and control brains to determine if microglia secrete proinflammatory cytokines to support T/NK cell recruitment and function. In additional *in vivo* studies I will determine if T and NK cells are the primary mediators of BCBM rejection. In these experiments I will use RAG1-KO mice deficient in adaptive immunity, wild type mice treated with S1P inhibitor to block T and NK cell extravasation from the blood vessels into the tissue, and IL2-complex treatment to stimulate cytotoxic CD8+ T and NK cell function in FIRE-KO mice to attempt to rescue their deficiency in responding to BCBM (Klevorn et al. 2016; Weiler et al. 2014). Together, these studies will address the mechanism through which microglia, T cells and NK cells control BCBM.

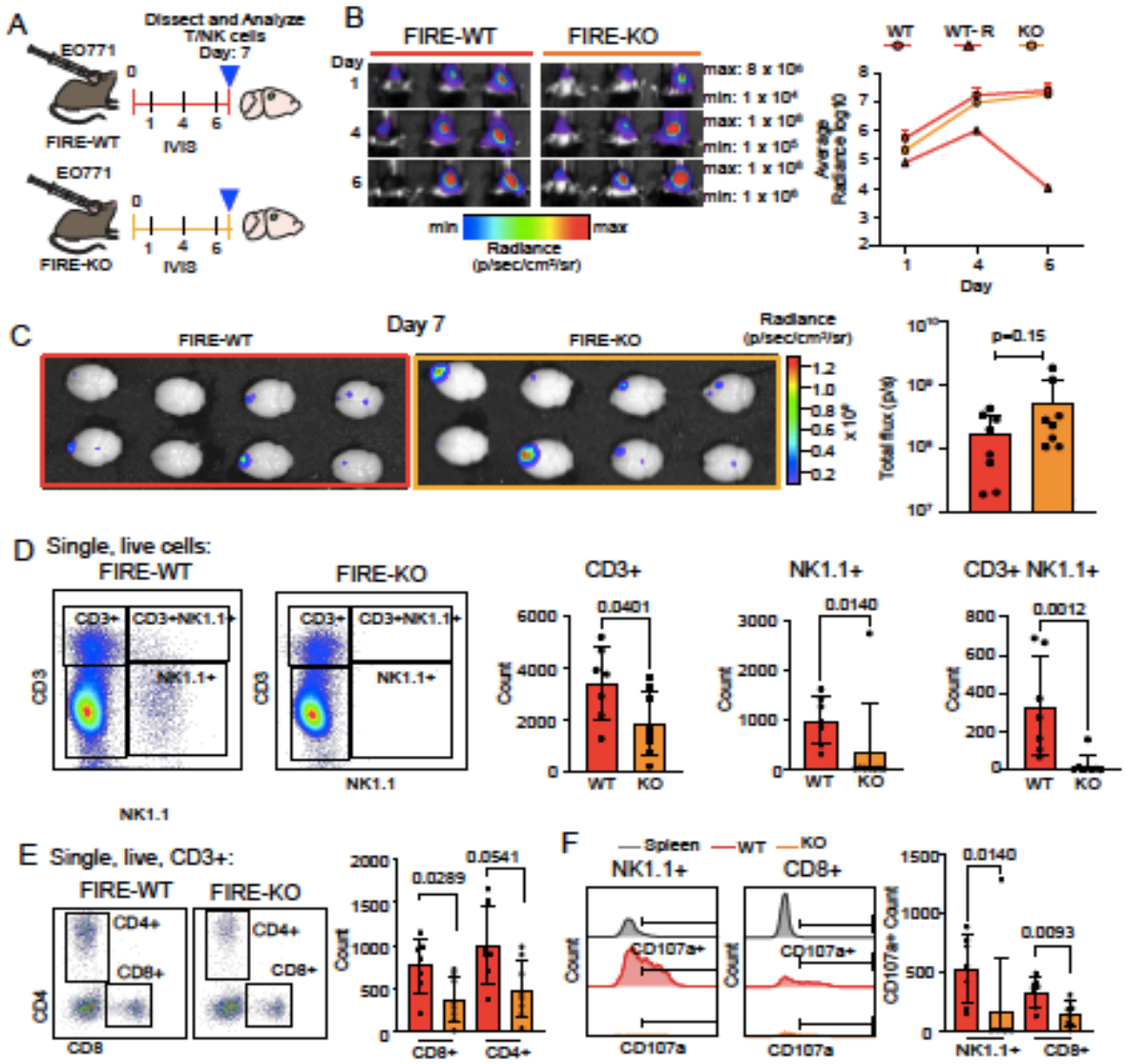

**Figure 7. Microglia deficient FIRE-KO mice have impaired T and NK cell response during BCBM metastasis initiation.** (A) Schematic of experimental design. FIRE-WT (n = 8) and FIRE-KO (n=8) were injected with 100,000 EO771 GFP and luciferase expressing cells in the right hemisphere on day zero and were monitored for tumor growth by IVIS on day 1, 4 and 6 post injection. Mice were euthanized and dissected on day 7 and brains were imaged by whole mount for luminescence and then dissociated to analyze T, NK and monocyte cell infiltration. (B) Example FIRE-WT and FIRE-KO cranial luminescence shows that detectable luminescent signal above background and had increasing luminescent signal on day 4 and 6. Note one FIRE-WT in this cohort regressed from day 4-6. Luminescence wad quantified by drawing a region of interest around the head and subtracting background luminescence. Each time point pseudocoloring minimum (min) and maximum (max) is set to illustrate the minimum and maximum Radiance (p/sec/cm$^2$/sr), indicated to the right of the images. The average radiance for the 7/8 Fire-WT (WT, red lines and circles) with tumor growth, 1/8 FIRE-WT with tumor regression (WT-R, red lines and triangles) and 8/8 FIRE-KO with tumor growth (KO, yellow lines and circles). (C) Ex vivo IVIS analysis of FIRE-WT and FIRE-KO at day 7 showing luminescence in radiance (p/sec/cm$^2$/sr), and quantification of total flux per brain quantified by drawing a circle around each sample of the same size. P value shown is the result of an un-paired two tailed students t test. (D) Flow cytometry analysis of single, live CD3+ T, CD3+ NK1.1+ NKT, and NK1.1+ NK cells isolated from FIRE-WT (n=7, one brain was not analyzed due to failed perfusion) and FIRE-KO (n=8) mouse brains at day 7. Quantification of cell counts per 100,000 live cells are shown to the right. P values are the result of an unpaired Mann-Whitney t test. (E)Flow cytometry analysis of single, live, CD3+ CD4+ T helper and CD8+ cytotoxic T cells from FIRE-WT (n=7) and FIRE-KO (n=8) mouse brains at day 7. Quantification of cell counts per 100,000 live cells are shown to the right. P values are the result of an unpaired Mann-Whitney t test. (F) Flow cytometry analysis of NK and CD8 T cell CD107a surface expression (indicating degranulation). Histograms show the number of CD107a+ degranulating NK and CD8+ cells is decreased in FIRE-KO mice compared to FIRE-WT. Quantification of cell counts per 100,000 live cells are shown to the right. P values are the result of an unpaired Mann-Whitney t test.

We do not know why some wild type mice, or BCBM patients, are able to control tumor outgrowth. In our EO771-C57BL/6 mouse model nearly half of mice regress or reject tumors. This phenomenon likely involves the interplay between tumor cells, microglia, and infiltrating immune cells such as conventional CD4+ T, CD8+ T, NK cells, dendritic cells and monocyte derived macrophages. One potential approach to investigating this phenomenon would be to track intracranial tumor growth by IVIS and perform scRNAseq analysis of immune cells isolated from mice with tumor progression vs mice with tumor regression. This data may help generate new hypothesis regarding the dynamics of immune control of tumor growth in the CNS.

**BCBM-R microglia localization over space and time**

Other important remaining questions are 1) where do BCBM-R microglia localize in situ, 2) at what point do they begin responding, and 3) what cells do they associate with? To address these questions, I have begun multiplex immunofluorescence analysis of BCBM from FIRE-WT mice using the CO-DEtection by indEXing (CODEX) (**Fig. 9A**) (Goltsev et al. 2018). This technology has advantages over traditional immunofluorescence in that is limited to 4-6 fluorescence channels for visualizing proteins in situ. Rather, CODEX uses primary antibodies conjugated to unique DNA oligo barcodes, and iteratively images 3 probes + DAPI at a time using complementary 'reporter' oligoes conjugated to fluorescent dyes. Tissues can be stained with up to 40 antibodies and imaged over multiple sequential cycles to reveal each protein using an automated fluidics and microscope platform. Applying CODEX spatial analysis to our BCBM mouse model may help identify the location and cellular interactions between BCBM-R microglia, tumor cells and other immune cells. Analysis of different times and stages of BCBM will reveal microglia activation and immune response dynamics. Our scRNAseq data indicates a few key genes/ proteins can be used to identify BCBM-R microglia from homeostatic microglia. Additionally, our scRNA-seq data and flow cytometry analysis show that immune cells from the periphery infiltrate into the CNS during BCBM. Our new data generated in the FIRE-KO model indicates there is a critical axis between microglia and T/NK cells during BCBM initiation to suppress tumor outgrowth. Using the BCBM-R microglia signature I designed an 18-antibody panel to detect BCBM-R microglia and other immune cells in BCBM mouse tissue (**Table 2**). I have generated preliminary data which identifies BCBM-R microglia located in tumor proximal regions (**Fig. S9A-B and 9B**). Microglia proximal to BCBM and in tumor distal regions are positive for TMEM119, IBA1, and CD64, while microglia proximal to BCBM are also positive for BCBM-R signature proteins CD74, MHCII and ISG15. CD64 also brightly marks a population of TMEM119-negative macrophages on the boarder of the brain tissue. While these preliminary results are interesting, they are unfortunately mainly descriptive at this stage. Further refinement of this

extremely challenging technique and analysis pipeline are needed to complete this analysis. After troubleshooting tissue staining and post imaging analysis issues I will apply this CODEX panel to FIRE-WT and FIRE-KO BCBM and perform spatial analysis between BCBM-R microglia and infiltrating immune cells to uncover cellular interactions that may indicate why the T and NK cells fail to robustly respond in microglia deficient mice. Additional areas to investigate BCBM-R microglia using this CODEX panel include early and late stages of BCBM and growing vs regressing tumors.

**Table 2. CODEX panel for special analysis of BCBM-R microglia and other immune cells in mouse models of BCBM.** Antibody marker supplier clone or catalogue number and barcode indicated. Orange = dilution titration optimization needed. Green= works under current conditions. Blue = need to move to another channel. Red = custom conjugation reaction failed, need to re-do. *= custom antibody conjugation, #= purchased from Akoya.

| | CH1: DAPI | CH2: Alexa488 250ms | CH3: CY3/Atto550 400ms | CH4: CY5 500ms |
|---|---|---|---|---|
| Cycle 1 | DAPI | Blank/GFP | Bank | Blank |
| Cycle 2 | DAPI | *GFP(Abcam ab220802)BX040 | #CD31 (MEC13.3) BX002 | #CD11C (N418) BX030 |
| Cycle 3 | DAPI | *IL-1B(R&DAF-401) BX034 | #MHCII (M5/114.15.2) BX014 | #TCRB (H57-597) BX003 |
| Cycle 4 | DAPI | #CD11B(M1/70)-BX025 | #CD4 (RM4-5) BX026 | *ISG15 (1H9L21) BX045 |
| Cycle 5 | DAPI | #CD45(30-F11) BX007 | #CD8a (53-6.7) BX029 | *CD74 (ln1/CD74) BX036 |
| Cycle 6 | DAPI | | #Ki67 (B56) BX047 | *IBA1 (polyclonal Wako 019-19741) BX042 |
| Cycle 7 | DAPI | | *TMEM119 (195H4 synaptic systems 400 011) BX035 | *LY6C (HK1.4) BX006 |
| Cycle 8 | DAPI | | *F4/80 (BM8) BX032 | *CD49D (polyclonal Novus biologicals NBP2-68992)* |
| Cycle 9 | DAPI | | *CD64 (MA5-29706) BX005 | |
| Cycle 10 | DAPI | Blank/GFP | Bank | Blank |

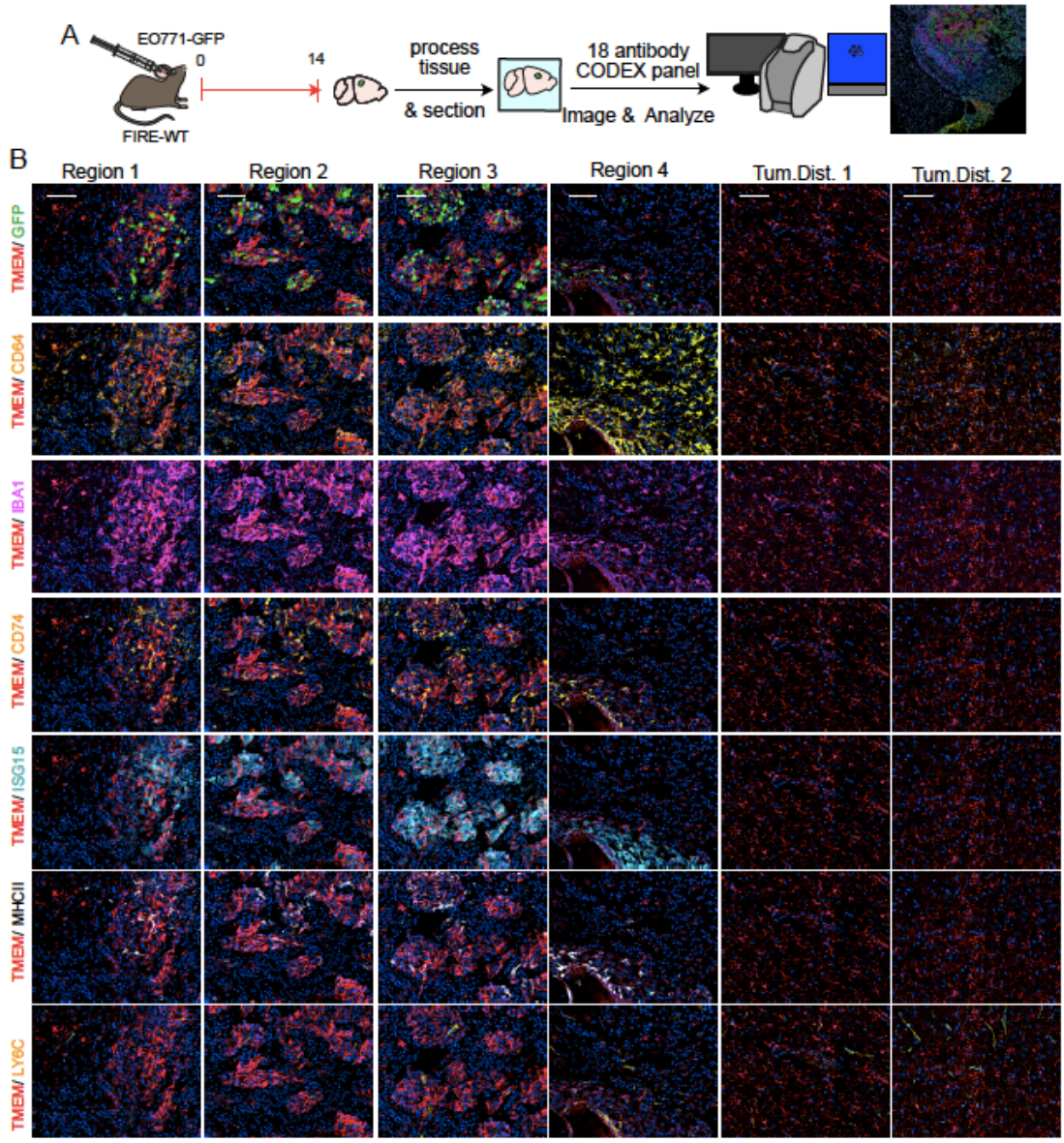


**Figure 8. Spatial analysis of BCBM-R Microglia using CODEX.** (A) Mouse brain tissue was fixed in 4% PFA overnight, cryoprotected in 30% sucrose 1X PBS until tissue equilibrated, then embedded in OCT and frozen for sectioning to 10 micron thickness and mounted on glass coverslips. Tissues were stained with 18 antibodies simultaneously following CODEX manual rev. C, and imaged using 20X PlanApo 0.75 NA lens using the CODEX automated imaging system with the Keyence 700 microscope and BZX software. A 7X7 tile scan with 6x Z planes 1.5u steps was taken, and processed using the CODEX processor to perform deconvolution, background subtraction, stitching, compression into one plane, and segmentation. Images were analyzed using CODEX MAV plugin on ImageJ and iindividual channels were adjusted for contrast and pseudocolored to enhance viewing. (B) Example tumor proximal and distal regions from EO771-GFP tumor bearing FIRE-WT mouse brain. Indicated markers GFP (green), TMEM119 (red), CD64 (yellow), IBA1 (magenta), CD74 (yellow), ISG15 (cyan), MHCII (white), and LY6C (yellow), are shown with DAPI (blue). Tumor proximal microglia are identified as TMEM119+ (red) and up-regulate ISG15 (cyan), MHC-II (white), and CD74 (yellow). Tumor proximal microglia are also positive for IBA1(magenta), and CD64 (yellow). Tumor distal microglia express TMEM119, CD64, and IBA1. A few tumor-distal microglia are also positive for CD74 (arrow). Little expression of MHC-II or ISG15 is observed in tumor distal microglia. LY6C+ cells (yellow) are shown as staining negative for TMEM119. Scale = 100 microns.

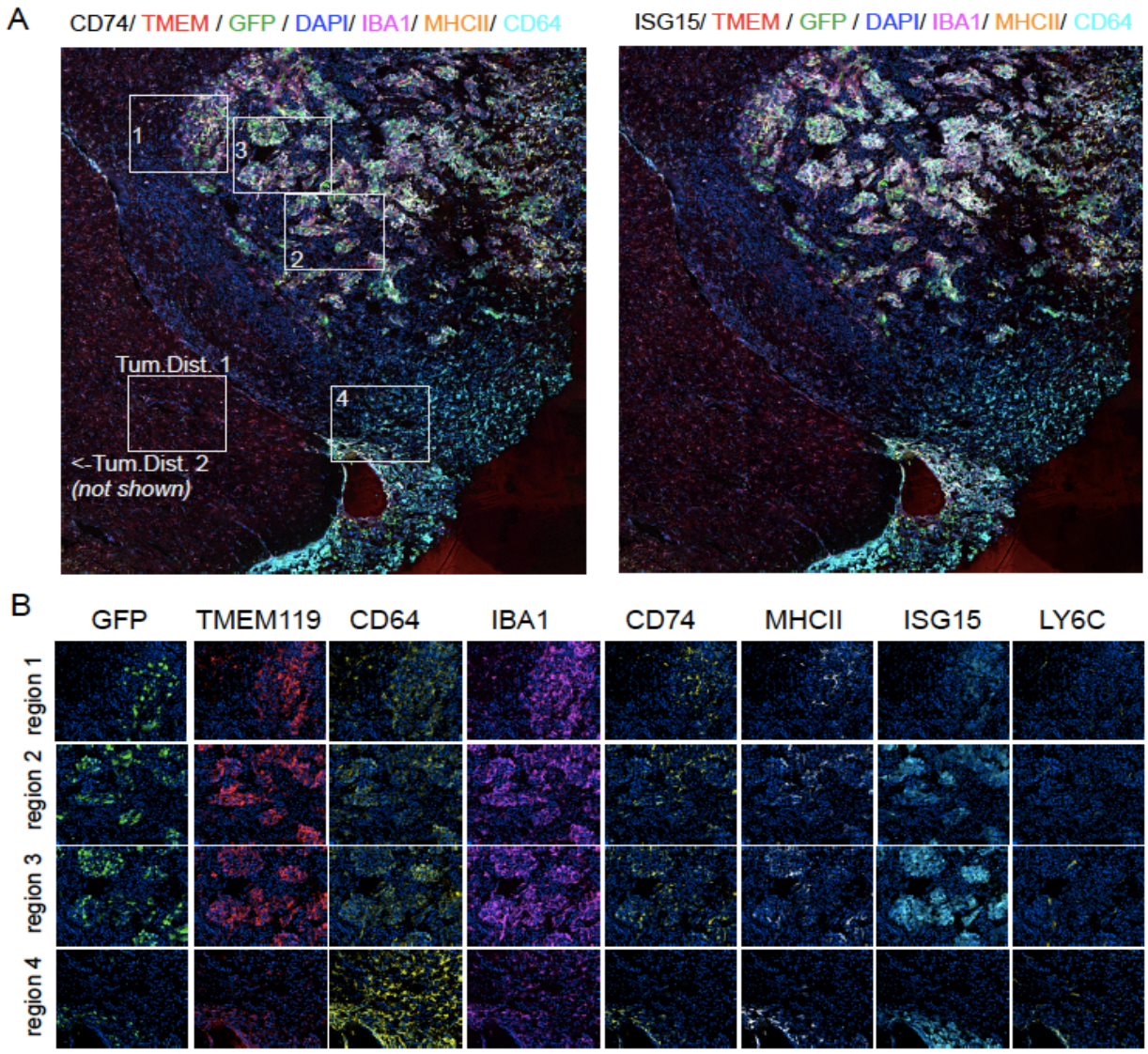


**Figure S8. Spatial analysis of BCBM-R Microglia related to Figure 8.** (A) Processed and stitched image of EO771-GFP tumor bearing FIRE-WT mouse stained with 18 antibodies simultaneously, the indicated markers are pseudo-colored as indicated above: CD74 (left) or ISG15 (right), (white); TMEM119 (red), GFP (green), DAPI (blue), IBA1 (magenta), MHCII (yellow), CD64 (cyan). Regions within the tumor and tumor distal are shown in white boxes. (B) Tumor proximal regions 1-4 shown with pseudo-coloring for each indicated marker.

# References


Azizi, Elham et al. 2018. "Single-Cell Map of Diverse Immune Phenotypes in the Breast Tumor Microenvironment." *Cell* 174(5): 1293-1308.e36.

Bennett, Mariko L et al. 2016. "New Tools for Studying Microglia in the Mouse and Human CNS." *Proceedings of the National Academy of Sciences of the United States of America*.

Betts, Michael R. et al. 2003. "Sensitive and Viable Identification of Antigen-Specific CD8+ T Cells by a Flow Cytometric Assay for Degranulation." *Journal of Immunological Methods*.

Blasius, Amanda L. et al. 2006. "Bone Marrow Stromal Cell Antigen 2 Is a Specific Marker of Type I IFN-Producing Cells in the Naive Mouse, but a Promiscuous Cell Surface Antigen Following IFN Stimulation." *The Journal of Immunology*.

Boche, D., V. H. Perry, and J. A R Nicoll. 2013. "Review: Activation Patterns of Microglia and Their Identification in the Human Brain." *Neuropathology and Applied Neurobiology* 39(1): 3–18.

Bos, Paula D et al. 2009. "Genes That Mediate Breast Cancer Metastasis to the Brain." *Nature*.

Bowman, Robert L. et al. 2016. "Macrophage Ontogeny Underlies Differences in Tumor-Specific Education in Brain Malignancies." *Cell Reports* 17(9).

Brufsky, Adam M. et al. 2011. "Central Nervous System Metastases in Patients with HER2-Positive Metastatic Breast Cancer: Incidence, Treatment, and Survival in Patients from RegistHER." *Clinical Cancer Research* 17(14): 4834–43.

Bruttger, Julia et al. 2015. "Genetic Cell Ablation Reveals Clusters of Local Self-Renewing Microglia in the Mammalian Central Nervous System." *Immunity* 43(1): 92–106.

Butler, Andrew et al. 2018. "Integrating Single-Cell Transcriptomic Data across Different Conditions, Technologies, and Species." *Nature biotechnology* 36(5): 411–20.

Butovsky, Oleg et al. 2014. "Identification of a Unique TGF-β-Dependent Molecular and Functional Signature in Microglia." *Nature Neuroscience*.

Campbell, J. Preston et al. 2012. "Models of Bone Metastasis." *Journal of Visualized Experiments*.

Chen, Edward Y et al. 2013. "Enrichr: Interactive and Collaborative HTML5 Gene List Enrichment Analysis Tool." *BMC bioinformatics* 14: 128.

Chen, Qing et al. 2016. "Carcinoma-Astrocyte Gap Junctions Promote Brain Metastasis by CGAMP Transfer." *Nature* 533(7604): 493–98.

Coniglio, Salvatore J et al. 2012. "Microglial Stimulation of Glioblastoma Invasion Involves Epidermal Growth Factor Receptor (EGFR) and Colony Stimulating Factor 1 Receptor (CSF-1R) Signaling." *Molecular Medicine*.

Contreras-Zárate, Maria J. et al. 2019. "Estradiol Induces BDNF/TrkB Signaling in Triple-Negative Breast Cancer to Promote Brain Metastases." *Oncogene* 38(24).

Davalos, Dimitrios et al. 2005. "ATP Mediates Rapid Microglial Response to Local Brain Injury in Vivo." *Nature Neuroscience*.

Deeken, John F., and Wolfgang Löscher. 2007. "The Blood-Brain Barrier and Cancer: Transporters, Treatment, and Trojan Horses." *Clinical Cancer Research* 13(6): 1663–74.

Duchnowska, Renata et al. 2016. "Immune Response in Breast Cancer Brain Metastases and Their Microenvironment: The Role of the PD-1/PD-L Axis." *Breast Cancer Research* 18(1).

Elmore, Monica R.P. et al. 2014. "Colony-Stimulating Factor 1 Receptor Signaling Is Necessary for Microglia Viability, Unmasking a Microglia Progenitor Cell in the Adult Brain." *Neuron*.

Elmore, Monica R.P. et al. 2018. "Replacement of Microglia in the Aged Brain Reverses Cognitive, Synaptic, and Neuronal Deficits in Mice." *Aging Cell*.

Fitzgerald, Daniel P. et al. 2008. "Reactive Glia Are Recruited by Highly Proliferative Brain Metastases of Breast Cancer and Promote Tumor Cell Colonization." *Clinical and Experimental Metastasis* 25(7): 799–810.

Ginhoux, Florent, and Marco Prinz. 2015. "Origin of Microglia: Current Concepts and Past Controversies." *Cold Spring Harbor Perspectives in Biology*.

Goldmann, Tobias et al. 2016. "Origin, Fate and Dynamics of Macrophages at Central Nervous System Interfaces." *Nature Immunology*.

Goltsev, Yury et al. 2018. "Deep Profiling of Mouse Splenic Architecture with CODEX Multiplexed Imaging." *Cell* 174(4).

Gonzalez, Hugo, Catharina Hagerling, and Zena Werb. 2018. "Roles of the Immune System in Cancer: From Tumor Initiation to Metastatic Progression." *Genes and Development* 32(19–20).

Gosselin, David et al. 2017. "An Environment-Dependent Transcriptional Network Specifies Human Microglia Identity." *Science*.

Griffith, Jason W., Caroline L. Sokol, and Andrew D. Luster. 2014. "Chemokines and Chemokine Receptors: Positioning Cells for Host Defense and Immunity." *Annual Review of Immunology* 32(1): 659–702.

Guldner, Ian H. et al. 2020a. "CNS-Native Myeloid Cells Drive Immune Suppression in the Brain Metastatic Niche through Cxcl10." *Cell* 183(5): 1234-1248.e25.

Guldner, Ian H et al. 2020b. "CNS-Native Myeloid Cells Drive Immune Suppression in the Brain Metastatic Niche through Cxcl10." *Cell*: 1–15.

Hammond, Timothy R. et al. 2019. "Single-Cell RNA Sequencing of Microglia throughout the Mouse Lifespan and in the Injured Brain Reveals Complex Cell-State Changes." *Immunity* 50(1): 253-271.e6.

Hammond, Timothy R, Daisy Robinton, and Beth Stevens. 2018. "Microglia and the Brain: Complementary Partners in Development and Disease." *Annual Review of Cell and Developmental Biology* 34(1): 523–44. https://doi.org/10.1146/annurev-cellbio-100616-060509.

Han, Jinming, Robert A. Harris, and Xing Mei Zhang. 2017. "An Updated Assessment of Microglia Depletion: Current Concepts and Future Directions." *Molecular Brain* 10(1): 1–8.

Hanisch, Uwe Karsten, and Helmut Kettenmann. 2007. "Microglia: Active Sensor and Versatile Effector Cells in the Normal and Pathologic Brain." *Nature Neuroscience*.

Hasselmann, Jonathan et al. 2019. “Development of a Chimeric Model to Study and Manipulate Human Microglia In Vivo.” *Neuron*.

Haynes, Sharon E. et al. 2006. “The P2Y12 Receptor Regulates Microglial Activation by Extracellular Nucleotides.” *Nature Neuroscience*.

Heaton, Haynes et al. 2020. “Souporcell: Robust Clustering of Single-Cell RNA-Seq Data by Genotype without Reference Genotypes.” *Nature Methods* 17(6): 615–20.

Herz, Jasmin et al. 2017. “Myeloid Cells in the Central Nervous System.” *Immunity*.

Hickman, Heather D. et al. 2015. “CXCR3 Chemokine Receptor Enables Local CD8+T Cell Migration for the Destruction of Virus-Infected Cells.” *Immunity*.

Hughes, Paula Marie et al. 2002. “Expression of Fractalkine (CX3CL1) and Its Receptor, CX3CR1, during Acute and Chronic Inflammation in the Rodent CNS.” *GLIA* 37(4).

Ito, Daisuke et al. 1998. “Microglia-Specific Localisation of a Novel Calcium Binding Protein, Iba1.” *Molecular Brain Research* 57(1).

Jordão, Marta Joana Costa, Roman Sankowski, Stefanie M. Brendecke, Sagar, et al. 2019. “Neuroimmunology: Single-Cell Profiling Identifies Myeloid Cell Subsets with Distinct Fates during Neuroinflammation.” *Science*.

Jordão, Marta Joana Costa, Roman Sankowski, Stefanie M. Brendecke, Sagar Giuseppe Locatelli, et al. 2019. “Single-Cell Profiling Identifies Myeloid Cell Subsets with Distinct Fates during Neuroinflammation.” *Science*.

Keren-Shaul, Hadas et al. 2017. “A Unique Microglia Type Associated with Restricting Development of Alzheimer’s Disease.” *Cell* 169(7): 1276-1290.e17. http://dx.doi.org/10.1016/j.cell.2017.05.018.

Kettenmann, Helmut, Uwe-Karsten Hanisch, Mami Noda, and Alexei Verkhratsky. 2011. “Physiology of Microglia.” *Physiological Reviews*.

Kienast, Yvonne et al. 2010. “Real-Time Imaging Reveals the Single Steps of Brain Metastasis Formation.” *Nature Medicine* 16(1): 116–22.

Klevorn, Lauryn E. et al. 2016. “Rescue of Tolerant CD8+ T Cells during Cancer Immunotherapy with IL2: Antibody Complexes.” *Cancer Immunology Research* 4(12).

Kuleshov, Maxim V et al. 2016. “Enrichr: A Comprehensive Gene Set Enrichment Analysis Web Server 2016 Update.” *Nucleic acids research* 44(W1): W90-7.

Lauro, Clotilde, and Cristina Limatola. 2020. “Metabolic Reprograming of Microglia in the Regulation of the Innate Inflammatory Response.” *Frontiers in Immunology* 11(March): 1–8.

Ley, Klaus. 2014. “The Second Touch Hypothesis: T Cell Activation, Homing and Polarization.” *F1000Research* 3(May): 1–15.

Li, Qingyun et al. 2018. “Developmental Heterogeneity of Microglia and Brain Myeloid Cells Revealed by Deep Single-Cell RNA Sequencing.” *bioRxiv*: 406363. https://www.biorxiv.org/content/early/2018/09/01/406363.full.pdf+html.

Li, Qingyun, and Ben A Barres. 2018. “Microglia and Macrophages in Brain Homeostasis and Disease.” *Nature reviews. Immunology* 18(4): 225–42.

http://www.ncbi.nlm.nih.gov/pubmed/29151590.

Lombardi, Giuseppe et al. 2014. “Systemic Treatments for Brain Metastases from Breast Cancer, Non-Small Cell Lung Cancer, Melanoma and Renal Cell Carcinoma: An Overview of the Literature.” *Cancer Treatment Reviews* 40(8): 951–59. https://linkinghub.elsevier.com/retrieve/pii/S0305737214000929 (February 11, 2019).

Lorger, Mihaela, Tereza Andreou, Christopher Fife, and Fiona James. 2019. “Immune Checkpoint Blockade - How Does It Work in Brain Metastases?” *Frontiers in molecular neuroscience* 12: 282. https://pubmed.ncbi.nlm.nih.gov/31824260.

Lorger, Mihaela, and Brunhilde Felding-Habermann. 2010. “Capturing Changes in the Brain Microenvironment during Initial Steps of Breast Cancer Brain Metastasis.” *American Journal of Pathology* 176(6): 2958–71.

Lou, Nanhong et al. 2016. “Purinergic Receptor P2RY12-Dependent Microglial Closure of the Injured Blood-Brain Barrier.” *Proceedings of the National Academy of Sciences of the United States of America* 113(4).

Mantovani, Alberto et al. 2017. “Tumour-Associated Macrophages as Treatment Targets in Oncology.” *Nature Reviews Clinical Oncology* 14(7): 399–416. https://doi.org/10.1038/nrclinonc.2016.217.

Martin, Allison M et al. 2018. “Immunotherapy and Symptomatic Radiation Necrosis in Patients With Brain Metastases Treated With Stereotactic Radiation.” *JAMA Oncology* 4(8): 1123–24.

Mathys, Hansruedi et al. 2017. “Temporal Tracking of Microglia Activation in Neurodegeneration at Single-Cell Resolution.” *Cell Reports* 21(2): 366–80. https://doi.org/10.1016/j.celrep.2017.09.039.

McGinnis, Christopher S. et al. 2019. “MULTI-Seq: Sample Multiplexing for Single-Cell RNA Sequencing Using Lipid-Tagged Indices.” *Nature Methods*.

McQuade, Amanda et al. 2018. “Development and Validation of a Simplified Method to Generate Human Microglia from Pluripotent Stem Cells.” *Molecular Neurodegeneration*.

Mildner, Alexander et al. 2017. “P2Y12 Receptor Is Expressed on Human Microglia under Physiological Conditions throughout Development and Is Sensitive to Neuroinflammatory Diseases.” *GLIA*.

Mills, Evanna L. et al. 2016. “Succinate Dehydrogenase Supports Metabolic Repurposing of Mitochondria to Drive Inflammatory Macrophages.” *Cell* 167(2): 457-470.e13.

Motenko, H., S. B. Neuhauser, M. O’Keefe, and J. E. Richardson. 2015. “MouseMine: A New Data Warehouse for MGI.” *Mammalian Genome* 26(7–8): 325–30.

Mrdjen, Dunja et al. 2018. “High-Dimensional Single-Cell Mapping of Central Nervous System Immune Cells Reveals Distinct Myeloid Subsets in Health, Aging, and Disease.” *Immunity* 48(2): 380-395.e6. http://dx.doi.org/10.1016/j.immuni.2018.01.011.

Munro, David A D et al. 2020. “CNS Macrophages Differentially Rely on an Intronic Csf1r Enhancer for Their Development.” *Development (Cambridge, England)* 147(23): dev194449. https://pubmed.ncbi.nlm.nih.gov/33323375.

Neil, Stuart J.D., Trinity Zang, and Paul D. Bieniasz. 2008. “Tetherin Inhibits Retrovirus Release and

Is Antagonized by HIV-1 Vpu." *Nature*.

Niikura, Naoki et al. 2014. "Treatment Outcomes and Prognostic Factors for Patients with Brain Metastases from Breast Cancer of Each Subtype: A Multicenter Retrospective Analysis." *Breast Cancer Research and Treatment* 147(1): 103–12. http://link.springer.com/10.1007/s10549-014-3090-8 (February 11, 2019).

O'Flanagan, Ciara H. et al. 2019. "Dissociation of Solid Tumor Tissues with Cold Active Protease for Single-Cell RNA-Seq Minimizes Conserved Collagenase-Associated Stress Responses." *Genome Biology* 20(1): 1–13.

Ostrom, Quinn T., Christina Huang Wright, and Jill S. Barnholtz-Sloan. 2018. 149 Handbook of Clinical Neurology *Brain Metastases: Epidemiology*. 1st ed. Elsevier B.V.

Priego, Neibla et al. 2018. "STAT3 Labels a Subpopulation of Reactive Astrocytes Required for Brain Metastasis." *Nature Medicine* 24(9): 1481. http://dx.doi.org/10.1038/s41591-018-0044-4.

Prinz, Marco, Daniel Erny, and Nora Hagemeyer. 2017. "Ontogeny and Homeostasis of CNS Myeloid Cells." *Nature Immunology* 18(4): 385–92. https://doi.org/10.1038/ni.3703.

Pukrop, Tobias et al. 2010. "Microglia Promote Colonization of Brain Tissue by Breast Cancer Cells in a Wnt-Dependent Way." *GLIA*.

Pyonteck, Stephanie M. et al. 2013. "CSF-1R Inhibition Alters Macrophage Polarization and Blocks Glioma Progression." *Nature Medicine* 19(10): 1264–72.

Qiao, Sha et al. 2019. "Long-Term Characterization of Activated Microglia/Macrophages Facilitating the Development of Experimental Brain Metastasis through Intravital Microscopic Imaging." *Journal of Neuroinflammation*.

Quail, Daniela F. et al. 2016. "The Tumor Microenvironment Underlies Acquired Resistance to CSF-1R Inhibition in Gliomas." *Science*.

Quail, Daniela F., and Johanna A. Joyce. 2017a. "The Microenvironmental Landscape of Brain Tumors." *Cancer Cell* 31(3).

Quail & Joyce. 2017b. "The Microenvironmental Landscape of Brain Tumors." *Cancer Cell* 31(3): 326–41.

Ries, Carola H et al. 2014. "Targeting Tumor-Associated Macrophages with Anti-CSF-1R Antibody Reveals a Strategy for Cancer Therapy." *Cancer cell* 25(6): 846–59.

Rojo, Rocío et al. 2019. "Deletion of a Csf1r Enhancer Selectively Impacts CSF1R Expression and Development of Tissue Macrophage Populations." *Nature Communications* 10(1).

Rongvaux, Anthony et al. 2014. "Development and Function of Human Innate Immune Cells in a Humanized Mouse Model." *Nature Biotechnology*.

Rostami, Rezvan et al. 2016. "Brain Metastasis in Breast Cancer: A Comprehensive Literature Review." *Journal of Neuro-Oncology*.

Russo, Matthew V., and Dorian B. McGavern. 2015. "Immune Surveillance of the CNS Following Infection and Injury." *Trends in Immunology*.

Schröder, Bernd. 2016. "The Multifaceted Roles of the Invariant Chain CD74 - More than Just a Chaperone." *Biochimica et Biophysica Acta - Molecular Cell Research*.

Sevenich, Lisa et al. 2014. “Analysis of Tumour- and Stroma-Supplied Proteolytic Networks Reveals a Brain-Metastasis-Promoting Role for Cathepsin S.” *Nature Cell Biology*.

Spangenberg, Elizabeth et al. 2019. “Sustained Microglial Depletion with CSF1R Inhibitor Impairs Parenchymal Plaque Development in an Alzheimer’s Disease Model.” *Nature Communications*.

Steeg, Patricia S. 2016. “Targeting Metastasis.” *Nature Reviews Cancer*.

Stuart, Tim et al. 2019. “Comprehensive Integration of Single-Cell Data.” *Cell* 177(7): 1888-1902.e21.

Taggart, David et al. 2018. “Anti–PD-1/Anti–CTLA-4 Efficacy in Melanoma Brain Metastases Depends on Extracranial Disease and Augmentation of CD8 T Cell Trafficking.” *Proceedings of the National Academy of Sciences*.

Ting, Jenny Pan Yun, and John Trowsdale. 2002. “Genetic Control of MHC Class II Expression.” *Cell*.

Tosoni, Alicia, Mario Ermani, and Alba A Brandes. 2004. “The Pathogenesis and Treatment of Brain Metastases: A Comprehensive Review.” *Critical Reviews in Oncology/Hematology* 52(3): 199–215. http://www.sciencedirect.com/science/article/pii/S1040842804001520.

Valiente, Manuel et al. 2014. “Serpins Promote Cancer Cell Survival and Vascular Co-Option in Brain Metastasis.” *Cell*.

Watanabe, Hiroyuki et al. 2004. “Innate Immune Response in Th1- and Th2-Dominant Mouse Strains.” *Shock*.

Wei, Spencer C., Colm R. Duffy, and James P. Allison. 2018. “Fundamental Mechanisms of Immune Checkpoint Blockade Therapy.” *Cancer Discovery* 8(9): 1069–86.

Weiler, Sven et al. 2014. “Orally Active 7-Substituted (4-Benzylphthalazin-1-Yl)-2-Methylpiperazin-1- Yl]Nicotinonitriles as Active-Site Inhibitors of Sphingosine 1-Phosphate Lyase for the Treatment of Multiple Sclerosis.” *Journal of Medicinal Chemistry* 57(12).

Witzel, Isabell et al. 2016. “Breast Cancer Brain Metastases: Biology and New Clinical Perspectives.” *Breast cancer research : BCR* 18(1): 8. http://www.ncbi.nlm.nih.gov/pubmed/26781299 (February 11, 2019).

Wolf, Susanne A, H.W.G.M. Boddeke, and Helmut Kettenmann. 2017a. “Microglia in Physiology and Disease.” *Annual Review of Physiology* 79(1): 619–43. https://doi.org/10.1146/annurev-physiol-022516-034406.

Yan, D et al. 2017. “Inhibition of Colony Stimulating Factor-1 Receptor Abrogates Microenvironment-Mediated Therapeutic Resistance in Gliomas.” *Oncogene*.

Zeiner, P. S. et al. 2018. “CD74 Regulates Complexity of Tumor Cell HLA Class II Peptidome in Brain Metastasis and Is a Positive Prognostic Marker for Patient Survival.” *Acta neuropathologica communications*.

Zeiner, Pia S. et al. 2015. “MIF Receptor CD74 Is Restricted to Microglia/Macrophages, Associated with a M1-Polarized Immune Milieu and Prolonged Patient Survival in Gliomas.” *Brain Pathology* 25(4): 491–504.

Zeisel, Amit et al. 2018. “Molecular Architecture of the Mouse Nervous System.” *Cell* 174(4): 999-1014.e22.

Zlotnik, Albert, and Osamu Yoshie. 2000. “Chemokines: A New Classification System and Their Role in Immunity.” *Immunity*.

# APPENDIX A: Gene signatures for BCBM-R microglia subpopulations

Table provides marker genes for BCBM-R microglia subpopulations (excluding Cycling) from Foxn1$^{nu/nu}$ data compared to all other myeloid cells from mice with BCBM, translated to their human equivalents using biomaRt in R. Related to **Fig 4.5.1**.

| APC | | IFN Responsive | Secretory | Glycolytic | | |
|---|---|---|---|---|---|---|
| ISG15 | ID2 | ISG15 | CD52 | MT-ATP6 | CXCL16 | TMSB4Y |
| MT-CO1 | BST2 | IFI44L | RHOC | ISG15 | RPL26 | RPS18 |
| CD52 | P2RY14 | TOR3A | PRDX1 | MT-ND1 | RPL35A | AIF1 |
| VCAM1 | CD300LF | GBP2 | CSF1 | ENO1 | UQCR11 | COX7A2 |
| GBP2 | CCL2 | IFI44 | RGS1 | RPL22 | SNRPG | RPS4X |
| FCGR3A | ITGB2 | FCGR1B | CH25H | RPL11 | RPL23 | EIF3E |
| FCGR3B | SLFN12 | FCGR1A | ATF3 | CD52 | CST7 | PABPC1 |
| GBP6 | SLFN12L | MNDA | SLC15A3 | UQCRHL | RPS15 | RPL8 |
| MNDA | CD86 | IFIT2 | RNF121 | RPS8 | CCL5 | RPS14 |
| IFI44L | ICAM1 | IFIT3 | RAB7B | GNG5 | CCL7 | CXCL13 |
| IFI44 | CCL4 | IFITM2 | CTSD | GBP2 | HMOX1 | ATP5MF |
| TOR3A | CCL4L2 | IFITM1 | LDHA | AKR1A1 | TSPO | |
| SLAMF8 | CD33 | IFITM3 | HCAR2 | PRDX1 | RPS19 | |
| PRDX1 | SIGLEC6 | TRIM5 | HCAR3 | UQCRH | SPP1 | |
| MS4A6A | ZBP1 | IRF7 | TNFRSF12A | RPS13 | EEF2 | |
| MS4A6E | CXCL10 | UBE2L6 | CADM1 | EEF1G | RPL32 | |
| SRGN | C19orf38 | IFIT1B | ALDOA | FAU | SELENOW | |
| IFIT1B | APOE | HCAR2 | LGALS3 | EIF5AL1 | RPL38 | |
| IL18BP | LGALS3BP | HCAR3 | CD63 | PGAM1 | TMSB10 | |
| IFIT2 | CXCL9 | PHF11 | PKM | EIF3F | RPS3A | |
| PRDX5 | STAT1 | STAT2 | CD9 | RPS3 | RPL22L1 | |
| CH25H | CD40 | MX1 | RPS2 | RPLP2 | RPL24 | |
| PSAP | SLFN5 | LGALS3BP | C3AR1 | ATP5F1C | RPL19 | |
| LDHA | TLR2 | CXCL10 | CST7 | COX8A | RTCB | |

| | | | | | |
|---|---|---|---|---|---|
| IRF7 | ARL5C | PARP14 | MT1G | PRDX5 | CXCL9 |
| IFITM2 | RPL19 | SP140 | PLEK | LDHA | COX7C |
| IFITM1 | RSAD2 | CCL4 | CCRL2 | IRF7 | RPL36 |
| IFITM3 | NAAA | CCL4L2 | CCL15-CCL14 | IFITM2 | COTL1 |
| IFIT3 | SAMHD1 | ZBP1 | CCL15 | IFITM1 | RPL18A |
| CD69 | CCL18 | IFI35 | CCL23 | IFITM3 | RPS21 |
| CD63 | CCL3 | XAF1 | CSTB | SERF2 | COX6B1 |
| RPS2 | CCL3L1 | CCL18 | ANKH | NACA | COPS9 |
| B2M | CCL3L3 | CCL3 | CD14 | ATP5F1B | RPL34 |
| COX6A2 | USP18 | CCL3L1 | FTL | RPL21 | RPL28 |
| ALDOA | USP41 | CCL3L3 | CAPG | COX6A2 | HINT1 |
| PSME1 | CCRL2 | SLFN5 | APOE | SLC25A3 | RPL31 |
| ITGAX | IL1B | USP18 | CCL18 | RPS2 | RPS28 |
| SERPINA3 | NFE2L2 | USP41 | CCL3 | CD63 | GPI |
| PKM | TAP2 | CCL2 | CCL3L1 | RPL4 | ZBP1 |
| LAG3 | IL2RG | EIF2AK2 | CCL3L3 | PFDN5 | EIF5A |
| CTSC | TAP1 | TSPO | NCEH1 | PSME2 | APOE |
| NPC2 | HLA-DQB1 | CMTM8 | OSM | ELOB | COX7A2L |
| LGALS3 | HLA-DQB2 | RTP4 | IL1B | NPC2 | COX4I1 |
| STAT2 | LPL | SLFN12 | TLR2 | RPL6 | RPL29 |
| PSME2 | HLA-DMB | SLFN12L | HMOX1 | PSME1 | RPL37 |
| HCAR2 | TAPBP | STAT1 | C5AR1 | TPT1 | LGALS3BP |
| HCAR3 | CRLF2 | CCL8 | CCL4 | ALDOA | UQCRQ |
| BCL2A1 | C4A | BST2 | CCL4L2 | B2M | RPL3 |
| PHF11 | C4B | DHX58 | EIF4A1 | RPS17 | RPS27A |
| CSTB | CD36 | HERC6 | MFSD12 | RPS25 | ATP5F1E |
| CCL8 | CSF2RA | IRGM | SPP1 | ATP5MG | C19orf38 |
| MIF | HLA-DOA | LY6E | GNAS | GATM | COX7B |
| CXCL16 | FGL2 | FGL2 | RPL32 | LGALS3 | RPL12 |
| SLC11A1 | CD83 | | CXCL16 | PKM | EIF3H |
| CXCL13 | CD72 | | LGALS1 | RPL18 | CD72 |

| | | | | | |
|---|---|---|---|---|---|
| SELENOW | CD274 | | PLAUR | TBCA | RPS6 |
| GRN | CD74 | | PLD3 | FTL | PSMB1 |
| RPS19 | ASS1 | | ID2 | BST2 | ASS1 |
| TSPO | CYBB | | MIF | RPL14 | CD74 |
| SPP1 | TNF | | GADD45B | RPS5 | RPL7 |
| HMOX1 | PIM1 | | CTSZ | AXL | ATOX1 |
| PARP14 | CTSB | | PMP22 | RPS16 | COX6C |
| CCL7 | IRGM | | RPL12 | EIF3K | PSMB8 |
| CCL5 | CDKN1A | | RPL35 | EEF1B2 | RPL35 |
| CST7 | PSMB8 | | TNF | UBA52 | RPL30 |
| RPL32 | HLA-DMA | | LPL | RPL13 | RACK1 |
| RPS5 | PGK1 | | CD83 | RPS9 | RPL36A |
| CTSZ | FTL | | CTSB | ATP5MGL | PGK1 |
| C3 | | | IER3 | CCL8 | TXN |
| AXL | | | SERPINE1 | MIF | HLA-DQB1 |
| IL1RN | | | FAM20C | CSTB | HLA-DQB2 |

# APPENDIX B: Flow cytometry panel for BCBM-R microglia and T cells

This is the standard flow cytometry panel used for analysis of BCBM-R microglia. Commercially available monoclonal antibodies were used with the indicated fluorophore and at the indicated dilution. Samples were dissected and dissociated as described in Chapter 3, Materials and Methods, and analyzed using the BD FortessaX20 in Gross Hall stem cell core facility at UCI Irvine. EO771, MDA231-BrM2 and 4T1 cell lines were transduced with GFP reporter.

| Marker | Color | Dilution |
|---|---|---|
| CD16/32 [93] | Na | 1:100 |
| CD45 [30-F11] | BV510 | 1:100 |
| CD11b [M1/70] | BV605 | 1:250 |
| CD90.2[30-H12], CD3[500A2] or TCRb[H57-597] | PercpCy5.5 | 1:100 |
| CD49b [HMa2] or NK1.1 [PK136] | PE594 | 1:100 |
| CD74 [ln1/CD74] | Alexa647 | 1:100 |
| CD317 (BST2/PDCA-1) [129c1] | PE | 1:100 |
| CD40 [3/23] | PE/Cy7 | 1:100 |
| I-A/I-E (MHCII) [M5/114.15.2] | Pacific Blue | 1:500 |
| Ly6C [HK1.4] | BV785 | 1:250 |
| Dead cells | ZombieNIR(APC/Cy7) | 1:500 |

## APPENDIX C: Flow cytometry panel for T and NK cell infiltration and activation in the mouse brain

This is the standard flow cytometry panel used for analysis of T and NK cell infiltration and activation in the mouse brain. Commercially available monoclonal antibodies were used with the indicated fluorophore and at the indicated dilution. Samples were dissected and dissociated as described in Chapter 3, Materials and Methods, and analyzed using the BD FortessaX20 in Gross Hall stem cell core facility at UCI Irvine. EO771, MDA231-BrM2 and 4T1 cell lines were transduced with GFP reporter.

| Marker | Color | Dilution |
|---|---|---|
| CD16/32 [93] | Na | 1:100 |
| CD107a [1D4B] | FITC | 1:100 |
| CD4 [H129.19] | BV605 | 1:500 |
| CD3[500A2] | PercpCy5.5 | 1:100 *intracellular* |
| NK1.1 [PK136] | PE594 | 1:100 |
| CD8a [53-6.7] | Alexa647 | 1:500 |
| Foxp3 [FJK-16s] | PE | 1:100 *intracellular* |
| CD11b [M1/70] | PECy5.5 | 1:100 |
| CD44 [IM7] | PE-Cy7 | 1:300 |
| Ly6C [HK1.4] | APC-FIRE | 1:200 |
| CD62L [MEL-14] | BV785 | 1:200 |
| CD152 (CTLA-4) [UC10-4F10-11] | APC | 1:100 *intracellular* |
| Dead cells | Amcyan Invitrogen live/dead fixable stain kit Aqua | 1:500 |